Design and Analysis of High-Performance Surface Plasmon Resonance based Optical Sensor for Biomedical Applications

Submitted in partial fulfilment of the requirements
for the award of the degree of

Doctor of Philosophy

by

V. YESUDASU
(Roll No. 719075)

Supervisor

Dr. Himansu Shekhar Pradhan
Assistant Professor, Dept. of ECE

Department of Electronics & Communication Engineering
NATIONAL INSTITUTE OF TECHNOLOGY WARANGAL – 506004, T.S, INDIA
March-2022

APPROVAL SHEET

This thesis entitled "**Design and Analysis of High-Performance Surface Plasmon Resonance based Optical Sensor for Biomedical Applications**" by Mr. **V. Yesudasu** is approved for the degree of **Doctor of Philosophy**.

Examiners

_____

_____

Supervisor

_____

Dr. Himansu Shekhar Pradhan

Assistant Professor, Electronics and Communication Engineering Department,

NIT WARANGAL

Chairman

_____

Dr. Patri Sreehari Rao

Head, Electronics and Communication Engineering Department,

NIT WARANGAL

Date:

Place: Warangal

DECLARATION

This is to certify that the work presented in the thesis entitled "**Design and Analysis of High-Performance Surface Plasmon Resonance based Optical Sensor for Biomedical Applications**" is a bonafide work done by me under the supervision of **Dr. Himansu Shekhar Pradhan**, Department of Electronics and Communication Engineering, National Institute of Technology Warangal, and was not submitted elsewhere for the award of any degree.

I declare that this written submission represents my ideas in my own words and where others' ideas or words have been included, I have adequately cited and referenced the original sources. I also declare that I have adhered to all principles of academic honesty and integrity and have not misrepresented or fabricated or falsified any idea/date/fact/source in my submission. I understand that any violation of the above will be cause for disciplinary action by the institute and can also evoke penal action from the sources which have thus not been properly cited or from whom proper permission has not been taken when needed.

V. Yesudasu

Roll No: 719075

Date:

Place: Warangal

Department of Electronics and Communication Engineering
National Institute of Technology
Warangal – 506 004, Telangana, India

CERTIFICATE

This is to certify that the dissertation work entitled **"Design and Analysis of High-Performance Surface Plasmon Resonance based Optical Sensor for Biomedical Applications"**, which is being submitted by Mr. V. Yesudasu (Roll No.719075), is a bonafide work submitted to National Institute of Technology Warangal in partial fulfilment of the requirement for the award of the degree of **Doctor of Philosophy in Electronics and Communication Engineering**.

To the best of our knowledge, the work incorporated in this thesis has not been submitted elsewhere for the award of any degree.

Dr. Himansu Shekhar Pradhan
Supervisor
Department of ECE
National Institute of Technology
Warangal – 506004

Dedicated to My

Family, Gurus, & Friends

I. CONTENT

II. ACKNOWLEDGEMENT

I am grateful to many people who made this work possible and helped me during my Ph.D. studies. I am greatly indebted to my research supervisor Dr. Himansu Shekhar Pradhan for giving me excellent support during my research activity at NIT Warangal. He encouraged me in choosing my research topic, his vision in my research area leads to successful investigations. I am very much thankful for giving research freedom and guidance, support in non-academic matters and for the humanity shown to me. With his inimitable qualities as a good teacher, he chiseled my path towards perfection. Ever since I met him, he has been an eternal source of motivation, inspiration, encouragement and enlightenment. He is responsible for making the period of my research work as an educative and enjoyable learning experience. The thesis would not have seen the light of the day without his insistent support and cooperation.

I am also grateful to Prof. P. Sreehari Rao, Head of the Department, Dept. of Electronics and Communication Engineering, for his valuable suggestions and support that he shared during my research tenure.

I take this privilege to thank all my Doctoral Scrutiny Committee members, Dr. P. Suresh, Department of Mechanical Engineering, Dr. V. V. Mani, Associate Professor, Department of Electronics and Communication Engineering, Dr. Mahammad Farukh Hashmi, Assistant Professor, Department of Electronics and Communication Engineering for their detailed review, constructive suggestions and excellent advice during the progress of this research work.

I am grateful to the former Heads of the ECE department Prof. N. Bheema Rao and Prof. L. Anjaneyulu for their continuous support and encouragement. I would also appreciate the encouragement from teaching, non-teaching members and fraternity of Dept. of E.C.E. of N.I.T. Warangal. They have always been encouraging and supportive.

I take this opportunity to convey my regards to my closest friends for being always next to me. Thanks to J. Ashish, S. Karthik Sai Ram, Dr. K. Krishna Reddy and P. Ravindra Department of Electronics and Communication Engineering for their motivation and support throughout my work.

I acknowledge my gratitude to all my teachers and colleagues at various places for supporting and cooperating me to complete this work.

I would like to thank my family members (V. Yesaiah, V. Ramadevi and V. Nageswararao) for giving me mental support and inspiration. They have motivated and helped me to complete my thesis work successfully.

Finally, I thank God, for filling me every day with new hopes, strength, purpose and faith.

V. Yesudasu

III. ABSTRACT

The surface plasmon resonance (SPR) based sensor is a promising device due to its label-free technique, quick response, high accuracy and high sensitivity. Since the last several decades, these sensors have capacity to detect interactions between biomolecules and chemical molecules based on minor changes in refractive index at the sensing interface. Therefore, SPR sensors have become increasingly popular among researchers in biomedical and health care applications to monitor biomolecular interactions like urea, bacterial and other specific biological samples. Although many other researchers have explored several SPR structures in the literature, society demands effective devices and techniques to save humans from deadly diseases. Moreover, the existing techniques are limited to measure or detect only few parameters at a particular wavelength using the angular interrogation method. Therefore, it's a challenge to improve the sensor performance for different applications at different wavelength regions. This thesis aims to overcome those problems and establish a new platform for SPR sensors in the biomedical field.

The thesis initially focuses on the prism-based SPR sensor design because of its simple structure and good light-coupling efficiency as compared to other SPR sensors. The performance enhancement of a prism-SPR sensor is presented in the thesis, where silver (Ag), black phosphorus (BP) and silicon are employed for DNA hybridization. The combination of Ag and BP provides high sensitivity with acceptable detection accuracy and quality factor. To improve the degraded parameters such as detection accuracy and quality factor, silicon has been incorporated between the silver and BP. Additionally, this work has investigated the performance of the SPR sensor in terms of figure of merit for the first time. However, the sensitivity is reduced slightly after adding silicon to the proposed structure. To overcome this problem, an SPR sensor based on the silicon and barium titanate structure is used to detect pseudomonas bacteria. In this work, three bacterial attachments are operated as a protective layer in the sensor structure for the detection process. The performance analysis reveals that good sensitivity is obtained with the proposed sensor (with silicon) compared to without silicon. When compared to the existing sensors, it is observed that the proposed models of earlier works show better performance employing the angular interrogation method. Moreover, the performance of the SPR sensor is validated using the wavelength region method as well as the Finite-Difference Time-Domain (FDTD) solutions. On the other hand, diffuse reflection in the visible-near-infrared range is used for the majority of analytical work. Therefore, the SPR

performance enhancement is executed at the visible-near-infrared region. Three different SPR structures have been proposed in this work using the combinations of dielectric and two-dimensional (2D) materials for urea detection. Though the proposed prism-based SPR sensors provide better performance compared to the existing sensors, they are not attractive for the remote sensing applications in hazardous areas. Therefore, fiber optic-based SPR sensors are highly preferred because they are robust, cost-effective, compact and quick in response. Moreover, the resonance feature can be easily tuned using a dielectric over-layer at the desired wavelength range. The modeling of a high-performance fiber optic-based SPR sensor for DNA hybridization using a hybrid structure of black phosphorus and tungsten disulfide is proposed in this thesis. The DNA hybridization sensing and the single nucleotide polymorphisms identifying procedure are shown by observing the resonance shift and transmitter power performances for probe DNA, mismatched DNA and complementary DNA stands. Moreover, the performance parameters, such as sensitivity, dip-of-figure-of-merit, quality-factor and detection-accuracy, are observed. The impact of the combination of dielectric and 2D materials towards the improvement of sensitivity, dip-of-figure-of-merit, quality-factor and detection-accuracy for an SPR based sensing system is evaluated using a numerical process and reported in this thesis.

IV. LIST OF FIGURES

V. LIST OF TABLES

VI. NOMENCLATURE

2D	Two-dimensional
A-M	Air and Metal
AS	Amplitude Sensitivity
Ag	Silver
AlAs	Aluminum Arsenide
ATR	Attenuated Total Reflection
Au	Gold
BaTiO3	Barium Titanate
BeFiO3	Bismuth Ferrite
BeO	Beryllium Oxide
BK	Borosilicate Glass
BP	Black Phosphorus
C	Velocity of Light
CSF	Combined Sensitive Factor
Cu	Copper
DA	Detection Accuracy
DFOM	Dip of Figure of Merit
DNA	Deoxyribonucleic acid
EM	Electromagnetic
EMW	Electromagnetic Wave
EW	Evanescent Wave
FDTD	Finite-Difference Time-Domain
FET	Field Effect Transistor
FOM	Figure of Merit
FWHM	Full Width Half Maximum
GaP	Gallium Phosphide
ISFET	Ion-Sensitive Feld Effect Transistor
IMOB	Immunochemical Optical Biosensor
I-SPR	Imaging Surface Plasmon Resonance
M-A	Metal and Air

M-D	Metal and Dielectric
MoS2	Molybdenum Disulfide
nm	Nano-meter
NNDS	Novel Nano-drug Delivery Systems
P-A	Prism and Air
P-M	Prism and Metal
PC	Propagation Constant
PD	Penetration Depth
PL	Penetration Length
RI	Refractive Index
RIU	Refractive Index Unit
r_p	Reflection Co-efficient
R_p	Reflectance Intensity
S	Sensitivity
Si	Silicon
SP	Surface Plasmon
SPW	Surface Plasmon Wave
SPP	Surface Plasmon Polariton
SPR	Surface Plasmon Resonance
SW	Surface Wave
TIBr	Thallium Bromide
TIR	Total Internal Reflection
TMM	Transfer Matrix Method
TP	Transmittance Power
QF	Quality Factor
WS	Wavelength Sensitivity
WS_2	Tungsten Disulfide

Chapter-1

Introduction

In recent years, surface plasmon resonance (SPR)-based biosensors have gained a lot of attention from researchers due to their extremely flexible features, label-free, noninvasive nature and wide use in various domains related to human life. It has multiple applications, including food safety, drug discovery, environment protection and medical diagnostics, organic chemical sensing, gas detection, bio-imaging, bio-sensing, glucose monitoring, disease detection, real-time monitoring and etc. The researchers have been developing the SPR sensors, optical sensors, and terahertz sensors for many effective applications because of the improvement of current technology. SPR based sensor has several advantages over other approaches, including a need of lower sample size, reusable sensor chips, the utilization of complicated samples and shorter experimental runs.

In 1902, the SPR technique was devised, and it was later utilized as a sensor [1]. Moreover, R. W. Wood worked on P-polarized light incident on the surface of the diffraction grating and observed the pattern of irregular light and dark lines that occur in reflected light [2]. In 1907, J. Zenneck et al. found the solution to the surface wave (SW) in form of Maxwell's equations. Electromagnetic waves (EMW) are excited at the periphery of two mediums, such as the lossy and loss-free mediums, due to the plasmons oscillation. Moreover, the lossy (imaginary) dielectric function is incumbent for binding the EMW and interface [3]. Further, A. Sommerfeld et al. noticed that J. Zenneck's hypothesized magnitude fields of SWs are inversely proportional to the square root of the distance from the dipole source. It is also a high-speed wave, and the intensity of the wave is exponentially decomposed with respect to the height above the boundary [4]. When R. H. Ritchie theoretically verified the occurrence of metal surface plasma excitations (SPE) in 1957, he made a substantial contribution to the SPR hypothesis [5]. C. H. Powell et al. determined that those surface plasmons (SPs) were excited by employing electrons at metal interfaces [6]. Later, E. A. Stern et al. observed that EM waves on a metal surface are contained EM radiation combined with plasmons. They also extracted the dispersion relationships on metal surfaces for SPWs [7].

Furthermore, a single crystal surface was analyzed by employing the conventional Otto configuration, which shows some gap between the prism and metal surface, and the results show that the prism is having no effect on the metal surface [8]. Similarly, the Kretschmann configuration is generally coated by the metal film thickness of 10-100nm that is deposited on

the prism surface for demonstrating the presence of SPs on that surface [9]. X.D. Hoa et al. and J. Homola et al. presented a substantial review of the SPR sensor technology, where it highlighted the key areas of applications, diverse methodologies (e.g., interferometry and luminescence) and that are used to examine the performance of chemical and biological sensors [10, 11]. Similarly, R. Ince et al. demonstrated that the characteristics of physical and chemical/morphological are essential for optical sensors, and these are incorporated into the sensor's operating theory [12]. In another investigation, O. S. Wolfbeis et al. described the condition of various chemical sensors and biosensors for fiber optics in 2006 [13]. Recently, many researchers have been focused on the performance enhancement of SPR-based sensor in terms of sensitivity, quality factor and detection accuracy employing different combinations of dielectric and two-dimensional (2D) materials for biological samples detection [14]. This sensor can be established a new platform for the SPR sensor in biomedical field to save human lives in rescue events. Therefore, being inspired by the exceptional background of the SPR sensor, the thesis is focused on enhancing the SPR sensor performance for different biomedical applications. The motivation for this topic and the overall organization of the thesis are described in the following sections.

1.1 Motivation

In 2019, 55% of the 55.4 million deaths occurred globally by the cause of non-communicable diseases, such as ischaemic heart disease, strokes, kidney diseases, lung cancer and diabetes mellitus. Ischaemic heart disease, stroke and chronic obstructive pulmonary disease are secured at first, second and third ranks in terms of leading causes of death, accounting for approximately 16%, 11% and 6% of all deaths, respectively. Moreover, kidneys play a key role in the human body, and it takes out waste and excess water from the bloodstream to form urine that passes out from the kidneys to the bladder via ureter. In this event, if the kidneys fail to eliminate the waste, then it can accumulate in the blood and damage the human body. The presence of higher urea levels in the human body indicates that the kidneys are not functioning properly. Highly sensitive devices are required to detect adequate waste disposal, such as urea. Furthermore, major biosensor devices are required in the medical industry to save human lives in rescue events. Therefore, SPR-based sensors are highly beneficial in addressing the aforementioned issues due to the high-quality data, high throughput and absorbing relatively small sample quantities. They can also measure real-time quantitative binding affinities, kinetics and thermodynamic parameters of interacting molecules. In addition, it has

several applications, such as bio-sensing and biomedical, which include novel nano-drug delivery systems (NNDS) and nano-cancer imaging (NCI) [15].

1.2 Problem Statement

The major intention for SPR design is that it is an emerging optical device to monitor minor changes in a structure's refractive index. However, several drawbacks are found in the literature.

- The existing studies have investigated mostly at the visible range wavelength.
- The investigated parameters are limited and have not met the required standards.
- The literature computed limited performance parameters, whereas other parameters like dip of figure of merit and combined sensitive factor represent the overall performance of the structure.
- Existing studies have focused on the performance enhancement of SPR sensors for a few applications, while deadly diseases are increasing day by day.
- The high-performance parameter of SPR sensor is needed be validate.

This thesis aims to address these above-mentioned problems and establish a new platform for the SPR sensor in the biomedical field.

1.3 Research Objectives

In order to mitigate the above-mentioned problems, and design and analysis of high-performance SPR based sensors in the biomedical field, the thesis has several objectives, which are mentioned below:

- Study the theoretical analysis of surface plasmon resonance (SPR)-based sensors, such as prism-based and fiber optic-based sensor.
- Performance enhancement of SPR sensor for DNA hybridization using different combinations of metal, dielectric and 2D materials.
- Sensitivity enhancement of SPR sensor for Pseudomonas bacterial detection employing a hybrid structure of dielectric materials.
- Design and analyze the high-performance SPR biosensor based on different hybrid structures.
- Validation of High-Performance Novel SPR Biosensor using the wavelength region method as well as FDTD solution tool.
- Performance enhancement of SPR sensor based on different emerging dielectric materials for urea detection at different wavelength regions.

- Design and analyse the high-performance fiber-optic-based SPR sensor for DNA hybridization employing TDMC material-based hybrid structure.
- Design and analyze the high-performance SPR based sensors.

1.4 Organization of the thesis

The thesis presents the numerical modeling of high-performance SPR based optical sensors for different biomedical applications at different wavelength regions. The contributions of the thesis have been mentioned from chapter-3 to 7. The thesis is divided into eight chapters, and the summary of each chapter is presented below.

Chapter-1: Introduction

It presents an introduction to the work, motivation, problem statement, objectives and contributions.

Chapter-2: Literature Review

The definition of SPR, its history, different types of SPR sensors and their configurations, literature review of the current state-of-the-art of SPR based sensors, such as prism-based and fiber optic-based sensors, as well as various methodologies and applications, have all been covered in this chapter.

Chapter-3: SPR performance enhancement for DNA hybridization employing black phosphorus, silver and silicon

In this chapter, the performance enhancement of the SPR sensor is presented for deoxyribonucleic acid (DNA) hybridization employing black phosphorus, silver and silicon configurations. Thicknesses of structure layers are obtained by the iteration process. The SPR performances are analyzed in terms of sensitivity, detection accuracy, quality factor, and figure of merit. The combination of silver and black phosphorus provides better sensitivity with degraded detection accuracy, quality factor, and figure of merit performances. To enhance the degraded parameters, a silicon layer is placed between the silver and black phosphorus. Finally, the comparative study has been carried out and observed that the proposed sensor provides better performance compared to existing sensors. However, the sensitivity of the proposed structure is reduced after adding the silicon to the structure. Therefore, to overcome this problem, a novel SPR sensor is designed with a silicon alloy structure in the next chapter.

Chapter-4: Sensitivity enhancement of the SPR biosensor for Pseudomonas bacterial detection employing a silicon-barium titanate structure

In this chapter, a novel SPR sensor is designed for Pseudomonas bacterial detection employing a silicon-barium titanate structure. In this work, three bacterial attachments are

operated as a protective layer for the detection process. Initially, thicknesses of structure layers are obtained by plotting reflectance curves with respect to an angle. To show the impact of silicon in the proposed structure, this study is considered three different structures with comprised layers. The SPR performances are analyzed in terms of sensitivity, quality factor and figure of merit. Results demonstrate that the proposed sensor improved the sensitivity performance after adding silicon to the structure. In addition, the proposed sensor is accomplished a magnified quality factor and figure of merit performances. Finally, the comparative study is demonstrated that this work is heightened performances of sensitivity and FOM. These earlier chapters provide better SPR performance compared to the existing works employing the angular interrogation method. However, validation for the SPR high-performance parameter is missing. Therefore, the high-performance of SPR sensor is designed and analysed in the next chapter by exploiting the wavelength region method as well as the FDTD solution tool.

Chapter-5: Design and analysis of high-performance SPR Biosensor based on different novel hybrid structures

In this chapter, the high-performance of SPR biosensor is designed and analyzed by employing different novel hybrid structures. This work is investigated in two parts. In the first part, the numerical analysis of SPR biosensor based on Bismuth Ferrite-Bromide materials-BP/Graphene hybrid structure using the transfer matrix method. In this study, the impact of 2D and bromide materials in the proposed structure is observed initially using the iteration method. Results show that the BP-based structure (Bismuth Ferrite-bromide materials-BP) provides better SPR performance than the graphene-based structure (Bismuth Ferrite-bromide materials-graphene). The maximum values of performance parameters are achieved for the Bismuth Ferrite-thallium bromide-black phosphorus structure. Therefore, being inspired by the properties of thallium bromide and black phosphorus, another SPR biosensor is designed employing aluminum arsenide, thallium bromide and black phosphorus in the second part. In this study, numerical analysis of another proposed structure is performed by appliying the transfer matrix method. The proposed SPR sensor achieves abnormal sensitivity performance with acceptable quality factor and figure of merit performances. In addition, this study introduces the performance parameter as combined sensitivity factor for the first time. Moreover, the high sensitivity performance of the proposed sensor is validated with the wavelength variation method by plotting reflectance curves at different wavelengths as well as by electric field intensity curves using the FDTD solution tool. The earlier studies have been carried out using the incident light wavelength of 633nm. On the other hand, diffuse reflection

in the different wavelength ranges is used for the majority of analytical work. Therefore, the SPR performance is investigated at different wavelength regions in the next chapter.

Chapter-6: High-performance SPR sensor for urea detection at different wavelength regions

In this chapter, a high-performance SPR sensor is presented for urea detection employing three different dielectric and 2D materials-based structures at the different wavelength regions. Firstly, performance enhancement of SPR sensor is shown employing molybdenum disulfide (MoS_2)-Dielectric materials- MoS_2 structure. Secondly, the SPR sensor based on the gold (Au)-beryllium oxide (BeO)-gallium phosphide (GaP) structure is presented. Thirdly, the SPR sensor employing an Au-dielectric material-based structure is presented. In each work, the metal film thickness is optimized by plotting the reflectance curves. Then, the impact of the proposed structure on the SPR sensor is shown by analysing the performance parameters. The performances of the proposed sensors are analyzed in terms of sensitivity and quality factor. Finally, the comparative study is demonstrated that the proposed sensors are accomplished better SPR performance compared to the existing sensors.

The earlier works have designed and analyzed the high-performance prism-based SPR sensors for different applications like DNA hybridization, bacteria detection and urea detection. The sensors have shown exceptional performance compared to existing works. However, prism-based SPR sensors are not attractive to remote sensing applications in hazardous areas. Therefore, fiber optic-based SPR sensors are highly preferred due to their properties like being robust, cost-effective, compact and fast in response. Also, it has several advantages over prism-based SPR including simple and flexible optical design, in-situ monitoring, and continuous analysis. Moreover, it is useful because the resonance feature can be easily tuned using a dielectric over-layer in the desired wavelength range. Therefore, the modeling of a high-performance fiber optic-based SPR sensor is presented in the next chapter.

Chapter-7: High-performance fiber-optic-based SPR sensor for DNA hybridization using black phosphorus-tungsten disulfide hybrid structure

In this chapter, a high-performance fiber optic-based SPR sensor is presented using a hybrid structure of black phosphorus and tungsten disulfide. This study shows the DNA hybridization sensing and the single nucleotide polymorphisms identifying procedure by observing the resonance shift and transmitter power performances for probe DNA, mismatched DNA and complementary DNA stands. Moreover, the performance parameters are investigated in terms of sensitivity, depth-of-figure-of-merit, quality factor and detection accuracy. Finally,

this work shows better SPR performance compared to the state-of-the-art works and includes an additional DFOM parameter, which shows the resonance depth effect.

Chapter-8: Conclusions and Future scope

It provides a summary of the thesis by highlighting the major contributions of this work along with a few suggestions for carrying out for future works.

Chapter-2

Literature Survey

2.1 Introduction

This chapter presents a literature survey on the performance analysis of SPR-based sensors, such as prism-based and fiber optic-based. Moreover, it describes the principles of SPR, the history of SPR and different configurations of SPR. For decades, many researchers have proposed several SPR structures for different applications. The major aspect of this chapter, research gap and outline areas for future study figure in the conclusion.

2.2 Plasmon oscillation

Chemistry demonstrates that delocalized electrons dissociate to a covalent bond and observed that they are in incoherence. Metal is an excellent conducting material with a regular array of atoms. An atom preserves at least one electron that is free to roam and disperse across all other particles in the material. These free electrons can generate an infinitely large mass, and are distinct from positive ions. Consequently, the Jellium model has been demonstrated that a constant positive charge background could replace these ions. However, the whole charge density settles at zero within the conductor. A peripheral field is applied to the conductor, and it controls free electron oscillation that degraded the free electrons' mass. In that case, the negative free electrons are no longer veiled by the background, and they begin to get attracted by the positive ion. The covalent bonding of these electrons and positive ions has happened in the background, and it unfolds at a higher density than is required to achieve charge neutrality. At the Coulomb repulsion, a restoring force generates and executes longitudinal oscillations among free electrons, known as plasma oscillations. The Quantum of the plasma oscillation is a plasmon, and the subsistence of plasma oscillations has been described in an electron energy loss experiment [15, 16].

2.3 Surface plasmon oscillation

The description of the classic drude conductive model has been revealed some metal characteristics, but not all of them are successful. The discovery of Bose-Einstein statistics and the development of quantum mechanics have explained the rest of the part. Light is an EM wave that strikes the metal as described in Fig. (2.1a), then the electric field of light interacts with conducting electrons in the metal, while atoms represent the quantum members apprehended as fermions. The oscillation of these electrons can lead to a wave pattern that is a

spatial distribution of particles, termed surface plasmon wave (SPW) or surface plasmon polaritons (SPPs). After generating the SPW, it opposes the light energy bearing in plasmons shown in Fig. (2.1b). The light absorbs its energy and converts it into a reflected light, and this phenomenon is a working principle for SPR sensors.

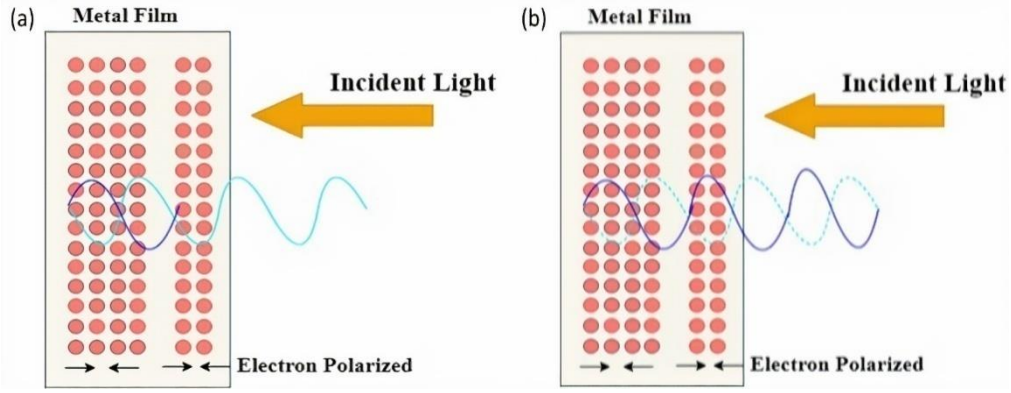

Fig.2.1 (a) Phenomenon of metals (b) Reminiscent of Lenz's law.

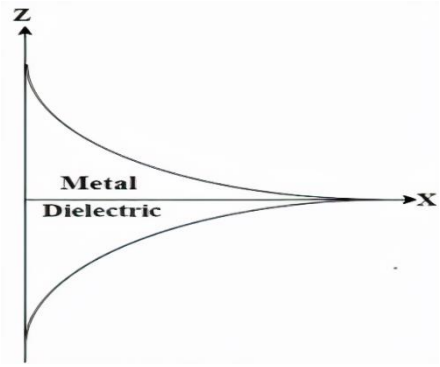

Fig. 2.2 Exponential intensity field for surface plasmon in M-D layers.

Moreover, the oscillation of the plasmon occurs at the metal and dielectric (M-D) interface. The charge density of the oscillations is well-known as surface plasmon oscillation, and the quantum of these oscillations is known as surface plasmon. These SPs are escorted by a longitudinal P-polarized electric field, decaying exponentially in metal and dielectric, as shown in Fig. (2.2); the consequence is that the field produces maximum intensity at the metal-dielectric (M-D) interface. These asserts achieve by unlocking Maxwell's numerical equation for the M-D category of refractive index (RI) allocation. The SPW propagation constant (PC) (K_{sp}) is incessant within the M-D interface, and is mathematically evaluated by applying Eq. (2.1).

$$K_{sp} = \frac{\omega}{c}\sqrt{\frac{\varepsilon_d \varepsilon_m}{\varepsilon_d + \varepsilon_m}} \tag{2.1}$$

Where, ω is the incident frequency, c is the velocity of light, ε_d and ε_m are the dielectric constants of the dielectric medium and the metal film, respectively. Moreover, $\varepsilon_m < 0$ and $\varepsilon_d > 0$ represent the metaland dielectric mediums respectively at a given wavelength. Eq. (2.2) shows the significant PC of the light wave at the propagation frequency via the dielectric medium. Fig. (2.3) represents the distribution curves K_{sp}, and the direct light incident through the dielectric medium(K_s). The SPs' PC is higher than the light wave in the dielectric medium, resulting in non-radiative SPs excited at the M-D interface, which means direct light cannot excite the SPs. Therefore, the wave vector of exciting light in the dielectric medium must increase for SPs excitation [17].

$$K_s = \frac{\omega}{c}\sqrt{\varepsilon_d} \tag{2.2}$$

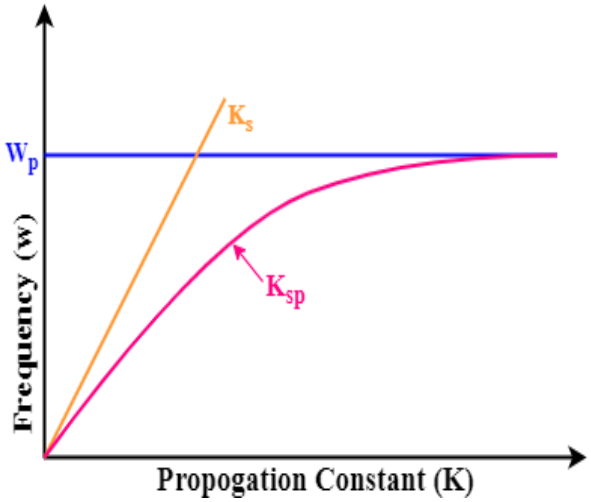

Fig. 2.3 Distribution curves for SPW and direct light incident via dielectric medium.

Furthermore, as SPP propagates along the M-D interface, it loses energy to the metal due to absorption. It can also lose energy due to scattering into free-space or into other directions. The electric field falls off evanescently perpendicular to the metal surface. At low frequencies, the SPP penetration depth into the metal is commonly approximated using the skin depth formula. In the dielectric, the field will fall off far more slowly. SPPs are very sensitive to slight perturbations within the skin depth and because of this, SPPs are often used to probe in homogeneities of a surface. Now the prism is coated with a thin film of a noble metal on the reflection site. In most cases, gold is used because it gives an SPR signal at convenient combinations of reflectance angle and wavelength. In addition, gold is chemically inert to solutions and solutes typically used in biochemical contexts [13]. When the electrical field energy of the photon is just right, it can interact with free electron constellations on the gold surface. These are the outer shell and conduction-band electrons. The incident light photons

are absorbed and the energy is transferred to the electrons, which convert into surface Plasmon's. Photon and electron behavior can only be described when they have both wave and particle properties. In accordance with quantum theory, plasmon is the particle name of the electron density wave. Therefore, when in a TIR situation, the quantum energy of the photons is right, the photons convert to Plasmon's leaving a 'gap' in the reflected light intensity.

The field decay in the direction perpendicular to the direction of propagation may be characterized by means of the penetration depth (L_p). Penetration depth is defined as the distance from the interface at which the amplitude of the field has fallen to $\frac{1}{e}$ of its value at the surface and is related to field parameters for the dielectric and metal, α_D and α_M, as mentioned in Eq. (2.3) [18].

$$L_{pD} = \frac{1}{Re\{\alpha_D\}} \quad \text{and} \quad L_{pM} = \frac{1}{Re\{\alpha_M\}} \tag{2.3}$$

Similarly, the attenuation of an SPW in the direction of propagation can be characterized by means of the propagation length (L), which is defined as the distance in the direction propagation at which the energy of the wave decreases by a factor of $\frac{1}{e}$, as shown in Eq. (2.4) [19].

$$L = \frac{1}{2Im\{\alpha_D\}} \tag{2.4}$$

Table 2.1 Major Characteristics of Surface Plasmon Polaritons

Metal	Silver		Gold	
Wavelength(nm)	630	850	630	850
Penetration depth into metal (nm)	24	23	29	25
Penetration depth into Dielectric (nm)	219	443	162	400
Propagation length (μm)	19	57	2	24

Characteristics of SPWs supported by the surface of gold and silver are given in Table 2.1. As follows, SPWs propagating along the surface of silver are less attenuated than those propagating along the surface of gold. Surface plasma waves propagate with high attenuation and the attenuation increases with decreasing wavelength.

2.4 Surface Plasmon Resonance

SPR is an analytical technique for studying molecular interactions. SPR is an optical effect that can be utilized to measure the binding of molecules in real-time without the use of labels. SPR instruments are primarily used to measure the binding kinetics and affinity of

molecular interactions. SPR can be used, for example, to measure the binding between two proteins, a protein and an antibody, DNA and a protein, and many more. SPR is unique because it is one of the few techniques that allow the determination of binding kinetics and not just binding affinity, as one would get from traditional techniques like ELISA. The binding kinetics or ON and OFF rates can only be determined with a bio-sensing technique that gives the real-time binding data of both the association and dissociation phases of the interaction. This data gives detailed insights into the binding strength and stability of the interaction, which is critical for many industries and research areas. It helps researchers determine which molecules interact, why they interact, and how strongly they interact.

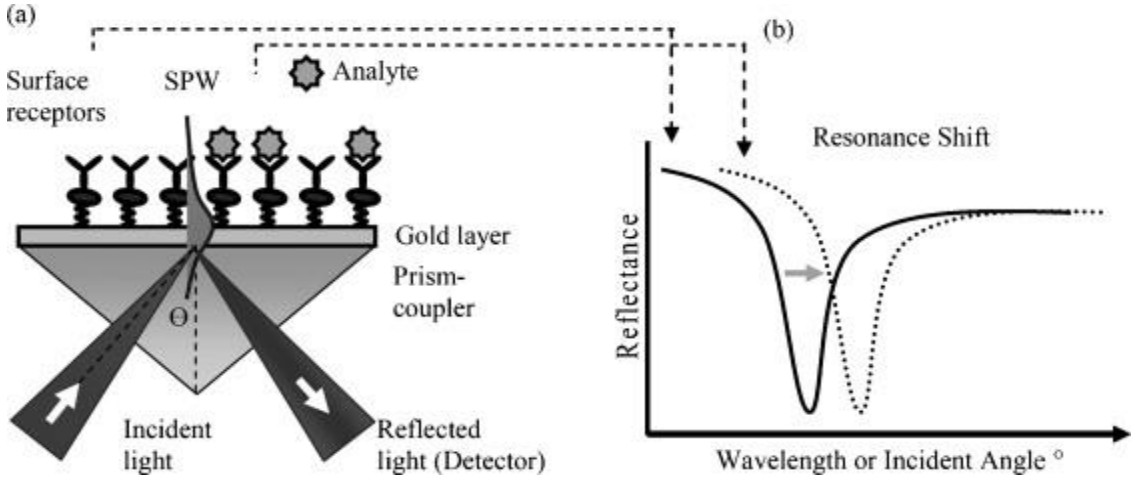

Fig. 2.4 (a) prism-coupled configuration (b) resonance shift in the reflected spectrum [19].

The sensitivity of SPR lies in the strong electromagnetic enhancement of SPW. Commercial SPR biosensors are generally capable of detecting absorbed analytes of 1pg/mm^2. This sensitivity is strongly dependent on many parameters, but is particularly dependent on surface functionalization. In comparing sensitivity between reported SPR biosensors, one must be cautious as the sensitivity values are often described independently of the surface functionalization chemistry or for a specific application. For a more relevant assessment, the sensitivity, where it is available, will be expressed in terms of detectable refractive index unit (RIU) change.

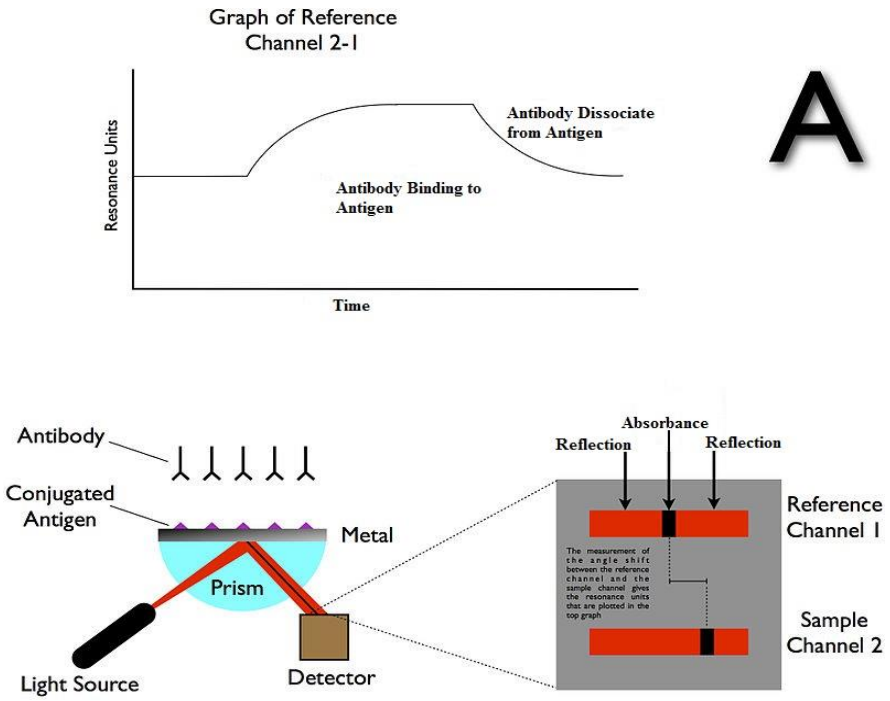

Fig. 2.5 SPR response [13].

Surface plasmons are used to enhance the surface sensitivity of several spectroscopic measurements including fluorescence, Raman scattering and second harmonic generation. However, in their simplest form, SPR reflectivity measurements can be used to detect molecular adsorption, such as polymers, DNA or proteins, etc. Technically, it is common to measure the angle of minimum reflection (angle of maximum absorption). This angle changes in the order of 0.1° during thin (about nm thickness) film adsorption. In other cases, the changes in the absorption wavelength is followed. The mechanism of detection is based on that the adsorbing molecules cause changes in the local index of refraction, changing the resonance conditions of the surface Plasmon waves. The same principle is exploited in the recently developed competitive platform based on loss-less dielectric multilayers, supporting surface electromagnetic waves with sharper resonances (Bloch surface waves).

The data from SPR is critical in a number of industries, and has been in use for over 25 years by companies like Pfizer, Roche, and GSK and by many universities throughout the world. Some examples of its applications include:

- Screening and developing new pharmaceuticals products and new bio-therapeutics
- Quality control in bioprocess monitoring
- Developing new diagnostic assays
- Basic research such as discovering and characterizing protein function, disease mechanisms, etc.

SPR has a number of advantages over other common assay techniques:

- Label-free (less expensive and easier to perform)
- Small sample volumes (100-200μL)
- High sensitivity (can be used on small molecules to large proteins)
- Real-time (giving deeper insight into the binding kinetics compared to yes/no binding or affinity techniques)
- Quantitative

2.5 Why Surface Plasmon Resonance

SPR sensor has been become the golden standard for providing optimal quality kinetics, real time interaction data, and label-free analysis for a wide variety of applications. For more than two decades, it has been becoming increasingly more affordable and accessible to researchers than ever before. One of the notable benefits of SPR is the value that SPR data can add to one's research. In fact, there are strong indications that SPR will become a standard technique available in every single biochemistry lab because it uncovers the true nature of binding interactions.

2.6 Types of SPR configurations

The reflected photons in total internal reflectance (TIR) are a procreation of an electrical field on the interface's opposite site. The plasmons develop a comparable area on either side of the metal film that spread out into the dielectric medium. This wave is called as evanescent wave (EW) because the wave magnitude decreases exponentially with sprouting distance from the surface of the interface, decaying over a range of one light wavelength. Fig. (2.6) shows the Otto configuration that operates with an ATR principle, which occurs at the prism-base coupling. An incident light passes at an angle higher than the critical angle via the prism-air (P-A) interface for the coupling of SPW with EW [17]. EW decays exponentially in the dielectric medium adjacent to the metal layer since both waves own the PC along with the interface. Therefore, a strong possibility of interface develops amid these waves. Eq. (2.5) denotes the x-component of the PC of the EW (K_{ev}) at the P-A boundary.

$$K_{ev} = \frac{\omega}{c}\sqrt{\varepsilon_p}\sin\theta \tag{2.5}$$

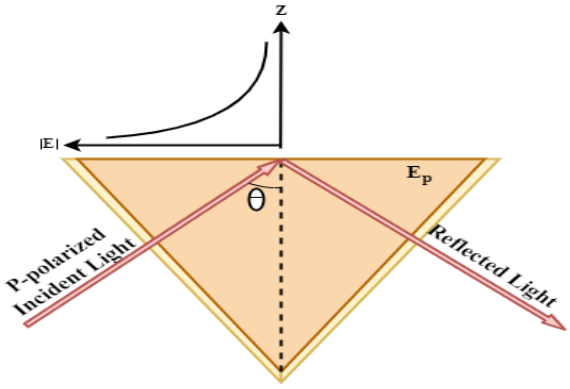

Fig. 2.6 Excitation of evanescent wave on the M-D interface.

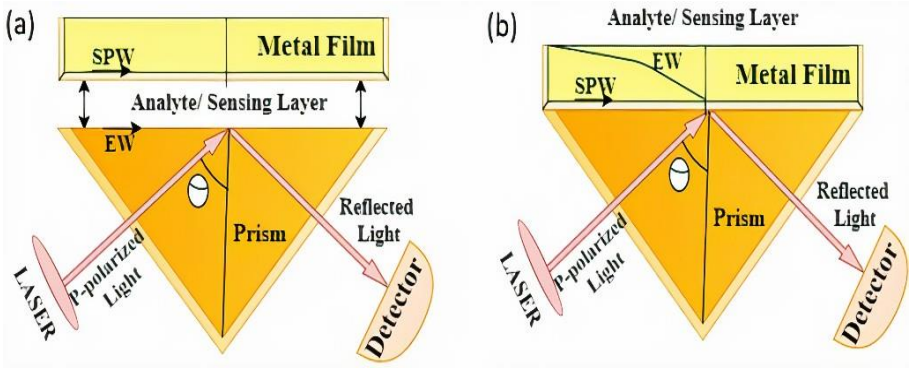

Fig. 2.7 (a) Otto configuration (b) Kretschmann configuration.

Furthermore, Fig. (2.7a) represents the Otto configuration that exposed a gap flanked by the prism and metal film. Exponential decay of the evanescent field occurs at the P-A interface, and this field can excite the SPs at the air-metal (A-M) boundary. Moreover, the configuration is inflexible for practical realization, but it's beneficial in analyzing the single-crystal metal surfaces and adsorption. Fig. (2.7b) represents the Kretschmann configuration, where a metal film is coated on the prism instead of air. An evanescent field is spawned at the prism-metal (P-M) interface, diminishing the attenuation due to environmental effects. This field can excite the SPs at the metal-air (M-A) interface.

Besides, Fig. (2.8) concludes that the PC of the EW could match with that of the SPW at the M-D interface relying on the frequency and incidence angle. Moreover, no excitation of SPs at the M-P interface, because of the PC of SPW lies to the maximum of EW's PC. Eq. (2.6) denotes the resonance condition, where minimum reflectance (R_{min}) is required for the SPR response [18]. Where, $\varepsilon_p$is the dielectric constant of the prism, θ_{res} is the resonance angle.

$$\frac{\omega}{c}\sqrt{\varepsilon_p}\sin\theta = \frac{\omega}{c}\sqrt{\frac{\varepsilon_d \varepsilon_m}{\varepsilon_d + \varepsilon_m}} \tag{2.6}$$

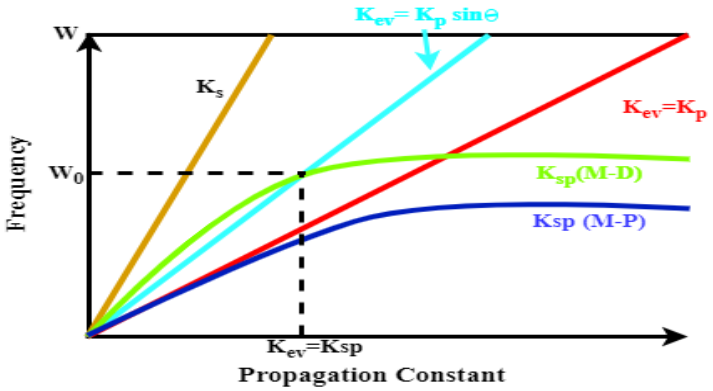

Fig. 2.8 Dispersal curves at M-D and M-P interface.

Fig. (2.9) depicts the resonance (θ_{res}), is the angle where minimal reflectance is achieved, and it varies according to the device parameters like the wavelength of light and RI of material. Moreover, Fig. (2.10) shows the θ_{res} fluctuation with respect to the RI. The fundamental performance parameters including sensitivity, detection accuracy (DA), quality factor (QF) must be as high as possible for a good SPR sensor, and the corresponding numerical expressions for computing the parameters have been mentioned in Eq. (2.7-2.9), respectively. In summary, higher sensitivity shows the sensor's immediate response capability, detecting minor changes in the RI. High DA serves the SPR sensor's ability to contribute to accurate outcomes, whereas high QF represents the sensor's quality. Change in resonance angle ($\nabla\theta_{res}$) represents changes in the resonance angle shift, while the full-width-half-maximum (FWHM) signifies full width at half of the maximum reflectance of the sensor. Moreover, Eq. (2.7) testifies the sensitivity is proportional to the resonance angle change, whereas the DA and QF are inversely proportional to the FWHM in Eq. (2.8-2.9).

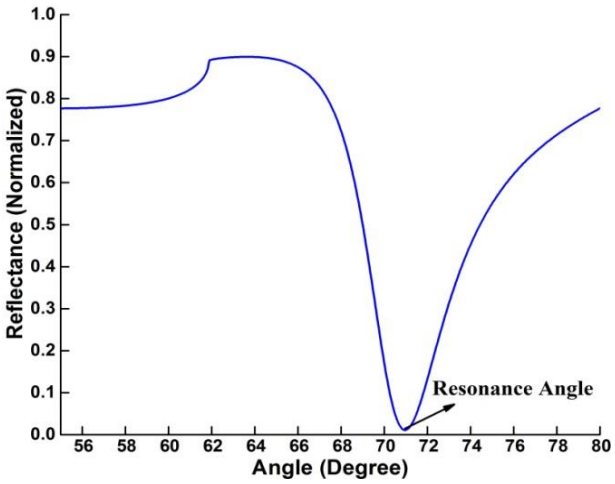

Fig. 2.9 SPR response in terms of reflectance.

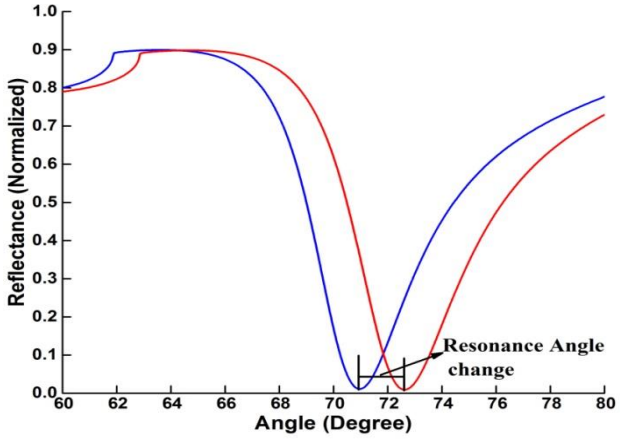

Fig. 2.10 The resonance shift ($\nabla\theta_{res}$) with respect to the RI change (∇n).

$$\text{Sensitivity(S)} = \frac{\text{Changeinresonanceangle}(\nabla\theta_{\text{res}})}{\text{Changeinrefractiveindex}(\nabla\text{n})} \tag{2.7}$$

$$\text{QualityFactor(QF)} = \frac{\text{Sensitivity(S)}}{\text{Fullwidthhalfmaxima(FWHM)}} \tag{2.8}$$

$$\text{DetectorAccuracy(DA)} = \frac{\text{Changeinresonanceangle}(\nabla\theta_{\text{res}})}{\text{Fullwidthhalfmaxima(FWHM)}} \tag{2.9}$$

2.7 Basic Principles

SPR is a physical process that can occur when plane-polarized light hits a thin metal film under total internal reflection conditions [13].

2.7.1 Total Internal Reflection (TIR)

When a light beam strikes a half-circular prism, it is bent in the direction of an interface plane, where it is going from a denser medium to a less dense medium, as illustrated in Fig (2.11a). If the incident light angle(θ) changes, the outgoing light is affected until it reaches a critical angle. At this point, all the incoming light reflects within the circular prism. This is called total internal reflection (TIR), as shown in Fig. (2.11b); though no light is coming out of the prism in TIR, the electrical field of the photons extends about a quarter of a wavelength beyond the reflecting surface.

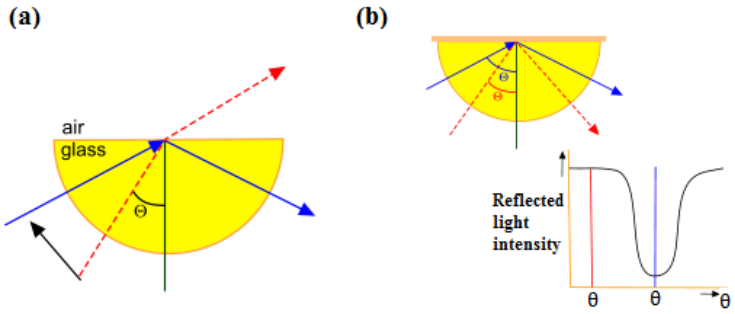

Fig. 2.11 (a) Reflection (b) Total Internal Reflection (TIR) [13].

2.7.2 Attenuated Total Reflection (ATR)

The Attenuated Total Reflection (ATR) technique be used to measure how a TIR infrared beam varies when it comes into contact with a sample. It can also can be used to determine the coupling between a LW in a high refractive index of dielectric medium and an SPW at low refractive index of metal film. An LW passes through a high refractive index prism and is totally reflected at the prism base generating an evanescent wave penetrating a metal film in configuration.

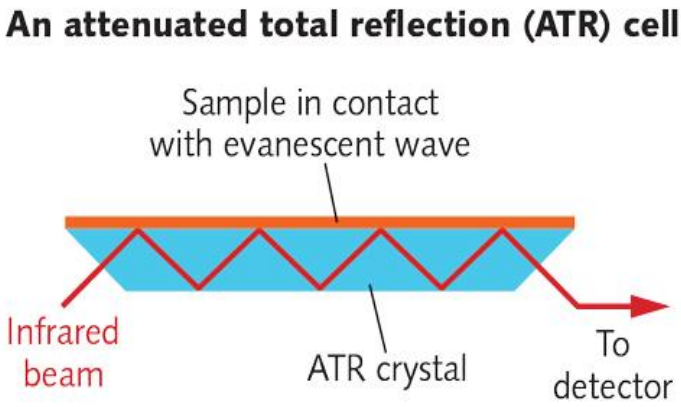

Fig. 2.12 Attenuated Total Reflection (ATR) [14].

ATR is a sampling technique that uses in conjunction with infrared spectroscopy, which enables the samples to be examined directly in a solid or liquid state without further preparation [14]. The sample is in the steel containers either side of the pink crystal. ATR uses a property of TIR resulting in an evanescent wave. A beam of infrared light is passed through the ATR crystal in such a way that it reflects at least once off the internal surface in contact with the sample. This reflection forms the evanescent wave, which extends into the sample. The wavelength of light, the angle of incidence, and the indices of refraction for the ATR crystal and the medium being probed define the precise penetration depth into the sample, which is normally between 0.5 and 2mm [14]. The number of reflections may be varied by varying the angle of incidence. The beam is then collected by a detector as it exits the crystal. Most modern infrared spectrometers can be converted to characterize samples via ATR by mounting the ATR accessory in the spectrometer's sample compartment. The accessibility of ATR- FTIR has led to substantial use by the scientific community.

2.8 Modelling of SPR reflectance

Surface Plasmon’s are particle waves of free electron plasma on a metal surface, which can be excited by p-polarized light under the resonance condition. A theoretical mathematical description for the resonance condition can be obtained by solving Maxwell equations for a

multilayer optical system, as represents in Eq. (2.10) [15], which provides the following mathematical solution for the resonance condition:

$$\frac{\omega}{c}\ \sqrt{\varepsilon_0}\ \sin\theta = \varepsilon_0 \sin\theta \sqrt{\frac{\epsilon_1 \epsilon_2}{\epsilon_1+\epsilon_2}} \tag{2.10}$$

Where, ω is the angular frequency of light, c is speed of light in vacuum, and ε_0, ε_1 and ε_2 are the permittivities of the prism, SPR metal layer and the adjacent medium, respectively. Conventional SPR measurements as applied in biosensors are used to monitor changes in thickness or refractive index of ultrathin organic films at metal surfaces [16]. The SPR phenomenon occurs when an incident beam of p-polarized light of a given wavelength strikes the surface at a given angle through a prism. In such conditions, photon–Plasmon surface electromagnetic waves (Surface Plasmon Polaritons) are created at the metal/dielectric interface. These waves propagate parallel to the metal dielectric interface and the associated optical electric field decays exponentially away from the surface with a typical decay length of 200 nm [16]. This results in a reduced intensity of the reflected light at this angle. The reflectance of the incident light at a given angle θ can be calculated using a three-layer Fresnel equation relating p-polarization [17], in which the sensing system consists of three media j, a glass prism-metallic film-sensing layer, denoted respectively by γ, μ and ρ subscripts. The reflectance R of the incident light is calculated as represented in Eq. (2.11).

$$\mathrm{R} = \left|\frac{\mathrm{r}_{\gamma\mu}+\mathrm{r}_{\mu\rho}\, \mathrm{e}^{2\mathrm{i}\mathrm{k}_\mu \mathrm{d}}}{1+\mathrm{r}_{\gamma\mu}\, \mathrm{r}_{\mu\rho}\, \mathrm{e}^{2\mathrm{i}\mathrm{k}_\mu \mathrm{d}}}\right|^2 \tag{2.11}$$

And the amplitude reflectance for prism-metal and metal-sensing layer interfaces are given by the following Eq. (2.12).

$$r_{\gamma\mu}=\frac{k_\gamma \backslash \epsilon_\mu - k_\mu \backslash \epsilon_\gamma}{k_\gamma \backslash \epsilon_\mu + k_\mu \backslash \epsilon_\gamma} \quad \text{and} \quad r_{\mu\rho}=\frac{k_\mu \backslash \epsilon_\rho - k_\rho \backslash \epsilon_\mu}{k_\mu \backslash \epsilon_\rho + k_\rho \backslash \epsilon_\mu} \tag{2.12}$$

Where,

$$k_j=\sqrt{\epsilon_j \frac{\omega^2}{c^2} - k_z^2} \quad \text{for j} = \gamma, \mu, \rho \quad \text{and} \quad k_z = \sqrt{\epsilon_\gamma}\,\frac{\omega}{c}\sin\theta$$

Here, ϵ_j and k_j are the dielectric constant and the wave-vector component perpendicular to the interface in the respective medium j (prism, metal or sensing layer), k_z is the component of the incident wave vector parallel to the interface, ω is the angular frequency of the incident light (ω (λ) = 2πc/λ), d is the thickness of the metallic film and c is the velocity of the incident light. According to the set of Eq. (2.11) and (2.12), the reflectance varies as a function of the dielectric constant ϵ_ρ of the sensing layer [17], which is the square of the refractive index. All these equations were obtained from references of [17] and [18]. These papers have shown the

details about the modeling SPR sensor using the transfer matrix theory. Moreover, LaSFN9 glass with a 50nm gold metal film was taken for proof-of principle demonstration of hypothesis testing approach in a conventional SPR system. Then, a more complicated sequence of layers was used to establish the sensitivity achievable by using hypothesis testing with a nanoparticle-inclusive sensor. Table 2.2 and 2.3 represent the parameters used in the modelling. The layers in the simulated nanoparticle-inclusive structure included a glass layer consisting of the LaSF9 prism and a 50nm thick metal layer, standard traditional SPR, either gold or silver coated with gold [17, 18].

Table 2.2 Layers in multi-layered nanoparticle simulation at λ=632.8nm

Layer No.	Material	Thickness(nm)	ϵ_1	ϵ_2
1	Prism(LaSFN9)	∞	3.4225	_
2	Gold	50	-13.4	1.4
3	SAM	5	2.25	_
4	Au Nanoparticles	24	-8.03	3.33
5	Water	∞	1.78	_

Table 2.3 Layers in multi-layered nanoparticle simulation at λ=543 nm

Layer No.	Material	Thickness(nm)	ϵ_1	ϵ_2
1	Prism(LaSFN9)	∞	3.4225	_
2	Gold	8	-5.84	2.11
3	SAM	5	2.25	_
4	Au Nanoparticles	24	-4.51	1.45
5	Water	∞	1.78	_
6	Silver	38	-12.8	0.43

A nanoparticle layer is located on top of the metal film. Attaching one of the binding molecules to the nanoparticle and introducing it to the sensor surface, where the complementary binding molecule is situated, is a popular method of introducing nanoparticles. This is generally done as a self-assembled monolayer (SAM). This modelling implies that Li

et al. used biotinylated gold nanoparticles with a diameter of 24nm to measure the simple biotin-streptavidin binding process [22]. It also assumed that the detection of analytes had been taking place in water. A collimated light source of varying wavelength was assumed to be uniform and steady, that is, all changes in reflectance beyond noise are assumed to be from the sample layer refractive index changes. The surface plasmon resonance angle mainly depends on the properties of the metal film, the wavelength of the incident light and the refractive index of the media on either side of the metal film [18]. Because the refractive index is sensitive to temperature, it is important to perform the measurements at defined temperatures. In some cases, this dependency can be exploited [19]. The refractive index is not dependent on the density of the media [20].

The metal must have the conduction band electrons, which are capable of resonating with the incoming light at a suitable wavelength [21]. This condition is satisfied by the metals, such as silver, gold, copper, aluminum, sodium and indium. In addition, the metal on the sensor surface must be free of oxides and sulphides, and it must not react with other molecules on exposure to the atmosphere or liquid [22]. Indium is too costly, sodium is too reactive, copper and aluminium have too broad an SPR response, and silver is too prone to oxidation among the metals. This proves the gold is the most practical metal to the build the high-performance SPR sensor. Gold is very resistant to oxidation and other atmospheric contaminants, but it is compatible with many chemical modification systems. The thickness of the metal layer plays a great importance in the modeling SPR sensor. The drop in reflective light gets shallower at an ideal thickness, and wider at the below optimum thickness [22]. The optimal thickness of the gold layer is ± 50 nm. The light source should be monochromatic and P-polarized (polarized in the plane of the surface) to obtain a sharp dip. All the light, which is not p-polarized, will not give any contribution to the SPR sensor, and will increase the background intensity of the reflected light [22]. Since in the metal film, the incident light and temperature are kept constant in experiments, the SPR signal is directly dependent on the change of refractive index of the medium on the sensor side of the SPR surface. Based on which characteristic of the LW interacting with the SPW is being measured, SPR sensors can be classified as follows:

2.8.1 Angle Interrogation

The component of the LW's wave vector parallel to the metal surface matching that of the SPW is determined by measuring the coupling strength at multiple angles of incident yielding the strongest coupling. The wavelength of LW used to excite an SPW is fixed.

2.8.2 Wavelength Interrogation

The component of the LW's wave vector parallel to the metal surface matching that of the SPW is determined by measuring the coupling strength at multiple wavelengths and determining the wavelength yielding the strongest coupling. The angle at which the LW is incident on the metal film is kept constant.

2.8.3 Polarization Modulation

The amplitude and phase of the TM-polarized wave interacting with the SPW change if the propagating constant of the SPW changes. Transverse electric-polarized LW does not interact with SPW's and thus exhibits no resonant amplitude or phase variations. Therefore, the polarization state of the incident LW consisting of both the polarization would also be sensitive to variations in the propagation constant of the SPW.

The modelling of SPR was performed using the transfer matrix method. Generally, the SPR modeling was done based on the wavelength interrogation and angle interrogation techniques. If the response of SPR is based on the wavelength then it is called wavelength interrogation. If it is based on angle, then it is called angle interrogation. The response is mainly based on some parameters i.e. thickness of metal film, dielectric constant of coating material, type of polarized transmission light, wavelength of transmission light.

Optical sensors based on resonant excitation of SPW's are often referred to as SPR sensors, and are optical devices that exploit the sensitivity of the propagation constant of an SPW to a refractive index to measure changes in the refractive index or changes in other quantities that can produce changes in the refractive index. A change in the refractive index to be measured produce a change in the propagation constant of SPW which results in a change in the characteristics of the LW interacting with the SPW.

2.9 History of SPR Biosensor

The term biosensor was introduced around 1975, relating to exploiting transducer principles for the direct detection of biomolecules at surfaces. Currently, the most prominent example of a biosensor is the glucose sensor, reporting glucose concentration as an electronic signal, which is based on a selective, enzymatic process. Some argued that all small devices are biosensors that are capable of reporting parameters of the human body (e.g. ion-sensitive field effect transistors (ISFETs) measuring pH). On other hand, a thermometer that records a fever should also be called as a biosensor. According to the present definition, in biosensors the recognition element (ligand) of the sensor or the analyte should originate from a biological source.

2.9.1 Early History of SPR Biosensors

Bio-molecular interaction monitoring is an application of SPR-based sensors, and this was initially demonstrated in 1983 by Lundstrom's study of physical methods for label-free and real-time applications [19]. The intrinsic properties of the molecules, such as mass, refractive index and charge distribution [20], were probed employing ellipsometry, refractometer, SPR, photothermic detection methods. Protein–protein interactions have been studied in real time, label-free, using ellipsometry at Sweden's National Defense Research Laboratory. Most importantly, the operating transducer mechanism exhibits the refractive index change at a light-reflecting surface. The ellipsometer has the problem of passing light through the bulk of the sample solution, despite being successful in detecting refractive index changes owing to biomolecule binding on optical transducer surfaces. Therefore, light-absorbing or particle-containing samples cannot easily be measured. The University of Twente (The Netherlands) was active in the search for new transduction principles for monitoring immunochemical reactions at field effect transistor devices (ImmunoFET) as well as at surfaces with an optical read-out(immunochemical optical biosensor, IMOB), during the same era [21]. Optical transducer principles including ellipsometry, SPR and interferometric principles (Mach Zehnder) have been seen as promising possibilities for direct transduction of bio-molecular binding event [22]. Successful measurements of immunochemical reactions based on SPR sensor have been carried out in the mid-1980s [23].

2.9.2 History of SPR Biosensors After 1990

In 1990, Pharmacia Biosensor AB has been launched the first commercial SPR product and the BIA-core instrument [24]. The instrument uses a most advanced, sensitive, accurate, reliable and reproducible direct biosensor technique, and SPR has been became the golden standard of transducer principles to measure real-time bio-molecular interactions. Manufacturers have been battling to achieve BIA-criteria core since the early 1990s. Fisons instruments made serious attempts to compete with BIA-core's technology [25]. For the investigation of bio-molecular interactions, their cuvette-based IA sys-instrument uses the evanescent field-based technology rather than SPR. The BIA-core 2000 instrument was introduced in 1994 with better detection and a new flow arrangement that allowed the sample to interface with the sensor at four different points. Signal correction could be done by employing data from the reference point. It has been also feasible to observe directly interactions of small molecule analytes responding to immobilised protein ligands after the introduction of BIA-core 2000 [26]. In 1995, the cuvette based SPR system of integrated bus

for intelligent sensors (IBIS) technologies was launched. The instrument is compatible with the BIA-core sensor chip. The IBIS II, a two-channel cuvette-based SPR instrument with auto-sampler operation, was introduced in 1997 [27]. IBIS Technologies started the development of an SPR imaging equipment after merging with SenS BV, a sensor chip coating firm, in 1999. In 2007, the scanning angle approach was employed to construct IBIS imaging-SPR (iSPR) equipment, which provides the requisite reliability and accuracy for microarray imaging of numerous bio-molecular interactions (4500). BIA-core X, a two-spot instrument, was introduced in 1996, and followed by the BIA-core 3000 in 1998. The latter was further enhanced with recovery tools to improve mass spectrometry interface [28]. Moreover, BIA-core Q was introduced for the food analysis market in 2000 Positioned for small molecule analysis and drug discovery. The introduction of BIA-core S51 marked a technological shift in terms of detection, flow cell design and sample capacity. The area of the detected spot was reduced from 1 to 0.01mm, and the number of spots increased from four to six. In 2004, a high-end instrument with four channels and five sensor locations was released (BIA-core A100). This instrument contains 20 in-line sensors to measure bio-molecular interactions in the flow cells, and it combines the flow cell of BIA-core S51 instrument with the performance of the four-channel BIA-core 3000. In 2005, Bia-core purchased HTS Bio-systems' grating coupler SPR device, which was co-developed with Applied Bio-systems (8500 Affinity Analyzer) and capable of photographing the sensor surface, in order to quantify up to 400 interactions simultaneously. This product (dubbed the Flex chip) was reintroduced in 2006 after a redesign [29].

2.10 Advantages of SPR

The Surface Plasmon Resonance has several advantages, some of which are mentioned below.

- Real-time Monitoring: Provides binding kinetics such as on and off rates on top of yes and no binding and affinity values.
- Label-free Detection: Measures interaction between analyte and ligand without spending time and money on expensive labeling reagents and protocols (i.e., radioactive fluorescent labels).
- Conserve Precious Samples: The nature of the technology requires only minimal amounts of sample, thus saving costs, reducing time needed for expression and purification.
- Reusable Sensor Chips: Regeneration buffers are used to disrupt the interaction between the analyte and ligand providing one with reusable sensor chips.

- Complex Sample Testing: Surface Plasmon Resonance can be used to test crude samples for applications such as serum analysis reducing time and cost associated with purification.
- Reliability and Accuracy: Ability to replicate experiments with ease through replicable sample injections and obtain accurate results from repeatable measurements.

2.11 Survey on the Prism-based SPR Sensor

This section looks at several numerical investigations done by other researchers based on prism-based SPR employing different structure for biomolecular interactions. Further, the evolution of prism-based SPR sensor for specific applications by many other researchers has been presented.

2.11.1 Evolution of prism-based SPR sensor for biomolecular interactions

Y. K. Prajapathi et al. proposed numerical analysis of standard four and five-layered SPR sensor that comprise metamaterials at visible range wavelength. They concluded that the proposed structure provides better performance compared to the conventional SPR sensor. Moreover, the metamaterial has been contributed to the sensor a broader dynamic range or efficient range of computable RI rises. It also has several advantages that can increase the resonance dip, which leads to higher sensitivity of the sensing resolution and dynamic range, for SPR sensor [30, 31]. J. B. Maurya et al. proposed an SPR sensor based on two different structures to improve the performance employing various types of prisms (BK7, SF11, and 2S2G), and metal materials (Au, Ag, copper (Cu), and aluminium (Al)) at 632.8 nm wavelength. Initially, they have been optimized each metal film's thickness and then elected the most desirable SPR performance content by comparing sensitivity, FWHM, and R_{min} parameters. Eventually, they concluded that the Ag renders high-QF and resolution, and Cu contributes better sensitivity [32]. S. Pal et al. used the new 2D material i.e., black phosphorus (BP), for sensors to enhance the performance parameters at 633 nm wavelength. The material had a sensitivity of 1.42 and 1.40 times greater than conventional SPR and the graphene-based SPR sensors, respectively. Better performance was achieved due to unique optical properties of BP, such as bandgap, higher charge mobility and increased binding of molecules on the surface sensor, though it renders little DA [33]. M. S. Rahman et al. incorporated Molybdenum disulfide (MoS_2) monolayer between the standard graphene and Au of SPR structure for enhancing sensitivity. They achieved the maximum sensitivity of 89.29°/RIU and 87.8°/RIU for double and monolayer of graphene-MoS_2 hybridization layers respectively for the proposed sensor. Finally, they highlighted that the proposed SPR with monolayer MoS_2 showed sensitivity, which was 10% higher than the sensor without MoS_2 [34].

Moreover, the MoS_2 offered agreeable QF and R_{min} performances compared to graphene [35, 36]. Furthermore, J. B. Maurya et al. utilized the dielectric material for enhancement of SPR sensor performance. The numerical analysis of SPR was done at 632.8nm wavelength and it was concluded that all performance parameters alter according to the sensing region's RI. The RI real part is directly proportional to the half-width half maxima (HMHM), and inversely to R_{min}. The RI imaginary part dielectric material is inversely proportional to HMHM, and directly proportional to the R_{min} [37]. The Silicon (Si)'s influence in SPR performance improvement employing a hybrid MoS_2-Graphene structure has been demonstrated in [35]. The MoS_2 layers are proportional to the sensitivity of the sensor at uniform graphene thickness. Moreover, Si affords massive DA and QF but degrades the little amount of sensitivity [38]. The numerical analysis of SPR sensor was performed at infrared wavelength, i.e., 1000nm, employing metamaterials. In this work, the authors considered the metamaterial RI and thickness are $n_{mat} = -\sqrt{\epsilon_{mat}\mu_{mat}}$ (where , μ_{mat}= -2.4+0.001i, ϵ_{mat}= -4+0.001i) and 349 nm, respectively; the RI of binding (single-standard Deoxyribonycic acid (ssDNA)) layers are n_b= 1.462, 1.466, 1.468; finally, the sensing medium RI for before and after adsorption of bimolecular are 1.33 and 1.35, respectively. The metamaterial enables abnormal sensitivity that is more than 300 °/RIU. In summary, the sensitivities for respected binding layers have been varied from 326.56 °/RIU to 454.36 °/RIU at n_b = 1.462; 327.19 °/RIU to 468.11°/RIU at n_b = 1.466; and 341.16 °/RIU to 489.88 °/RIU at n_b= 1.468 [39]. Another numerical investigation on SPR sensor has been presented in [41], where sensitivity is improved, and DA and QF performances diminish compared to existing work. The SPs generation at THz frequency is important for applications like biomedical sensing; therefore, Y. Xiang et al. studied plasmonic waves, which have the same properties as plasmonic waves in optical range wave because of that SPW's constraints within the boundary at THz frequency [41].

Furthermore, the angle and wavelength interrogation of Al-based SPR sensor performance have been performed theoretically and experimentally with trapezoidal BK7 prism. The Al performance was compared with other metal film material, such as Ag, Au, and Cu. Results concluded Al improves the performance in de-ionized water due to Al-surface oxide and constrained significant sensor degradation [42]. The performance analysis of graphene-based SPR was explored with a 13% improvement in sensitivity compared with existing work, where metal film thickness remains constant. In this work, the authors have been considered the RI (thickness) of the SF10 prism, Ag, MoS_2, Graphene, ssDNA and water to be 1.7786, 0.005625+4.276i (37 nm), 5.9+0.8i (M × 0.65 nm), 3+1.149106i (G × 0.34 nm), 1.462

(3.2 nm) and 1.3317, respectively [43]. Further investigation has been done on tungsten diselenide (WSe_2)-based SPR sensor and found the maximum sensitivity was found to be 237.5°/RIU for monolayer WSe_2 and seven layers of Si thickness [44].

Furthermore, the relation between sensitivity and surface resonance frequency (SRF) was analysed and it was found sensitivity is non-linear to SPR frequency as well as to number of graphene layers. The SRF and SPW's propagation velocity was computed by applying Eq. (2.13-2.14).

$$SRF = \frac{c_0}{n_{geo}} \frac{K_{SPW}}{2\pi} \tag{2.13}$$

Where, $K_{SPW} = \frac{2\pi}{\lambda} n_p \sin\theta_{SPR}$ (2.14)

Where, $\frac{c_0}{n_{geo}}$ is the propagation velocity of SPW, which is perpendicular to the confined evanescent wave, n_{geo} is $\sqrt[3]{n_{Au} n_S n_G}$ (n_{Au} represents the gold's RI, n_s represents the RI of sensing medium, and n_G represents graphene RI) [45]. The Otto configuration based SPR structure was designed with various combinations of the nano-composite and metal films for the sensitivity improvement. Results demonstrated better sensitivity of 200°/RIU at six layers of MoS_2 and monolayer graphene with TiO_2-Au composite material at 30nm thickness [46]. Further, M.S. Islam et al. presented the study of excitation, the nature of SPs, EM field distributions and magnitudes at both conventional and multilayer SPR structures. The SPWs are transpired when polarized light flows parallel to the interface. The strong plasmon induced on the sensing interface and captures less reflected light at resonance condition and vice-versa [47]. S. Pal et al. have been designed the BP-based SPR sensor with the consolidation of Au, Si and Transition Metal Dichalcogenides (TMDC) materials, such as WS_2 and WSe_2 for the enrichment of sensor sensitivity. The performance was achieved in terms of sensitivity, R_{min} and FWHM. The sensor accomplished excellent sensitivity of 184.6°/RIU with TMDC material and 163.1°/RIU without TMDC material [48]. R. Boruah el at. designed Kretschmann-based a novel SPR setup with double prisms for improving the performance of the sensor. This structure affords several advantages like intense output signals and wide-angular scan-ranges [49]. A. A. Michelson et al. inverted the interferometer and rotator, which accomplish phase and angle interrogations. The sensor was designed experimentally with a sensitivity of 7.2×10^{-7} RIU/0.1°, and figure of merit (FOM) of 316 at 1-1.4 range [50].

Moreover, S. K. Raghuwanshi et al. developed the SPR sensor by employing Teflon and metamaterial surfaces for powerful bio-recognition to explore the multi-layer sensor

structure's dispersion-customized properties. By using this sensor, the authors improved the sensitivity because it deducts side lobes' virtue in dual-mode. Moreover, the importance of SPW excitation methods for the sensors' design has been revealed [51]. C. A. De Souza Filho et al. described the effects of SPR biosensor, such as disturbances, noise, the incident light's temperature and wavelength. In addition, this design permits each component and the entire system to be evaluated individually. A solution has been presented to achieve increased energy-efficiency and facilitates handheld mobile phone-based sensors [52]. S. Scarano,et al. and M. Faca et al. studied analytical instruments as profitable and flexible diagnostic tools for an assortment of applications in bioanalytical chemistry, including SPR and SPR imaging. The bio-receptor has been immobilized on the bio-chip to decide the above systems' selectivity and ranges from the nucleic acid sequence to proteins, antibodies and new synthetic bio-receptors. It also enables label-free and multi-analyte detection. Moreover, a wide range of molecular weight target analytes can adapt to multiple assay designs, ranging from small molecules to living cells [53, 54]. The summary of the performance enhancement of the SPR sensor with different configurations has been presented in Table (2.4).

Table 2.4 Performance Enhancement of the SPR Sensor at 633nm Wavelength

References	Configuration	Performance Parameters			Conclusion
		S (°/RIU)	DA	QF (RIU^{-1})	
Y. K. Prajapathi et al. 2013 [31]	Prism+ Ag+Metamaterial+ Ag+ Au+ Water	-	-	-	The SPR sensor has the advantage of improving reflectance dip and S by employing the metamaterial layer.
J. B.Muryaet al.2015 [36]	Prism+ Au+ MoS_2 + Affinity+ Water	48.82	0.615	5.12	The SPR sensor proposed the effect of Si between metal and MoS_2.
	Prism+ Au+ Si+ MoS_2 + Affinity+ Water	48.65	10243	85365	

J. B.Murya et al.2016 [35]	Prism+ Si+ Graphene+ Affinity+ Sensing Layer	49.86	14.54	207.75	The sensor Ag + Graphene /MoS_2) presents the acceptable S, but the DA and QF are substantially higher than the existing work.
J. B.Murya et al.2017 [37]	Prism+ Metal+ Dielectric+ Water	-	-	-	The purely real part RI of the dielectric layer offers the contradicted results between$\nabla\theta$ and HWHM. To mitigate this problem increase the imaginary part of the complex RI of dielectric medium.
J. B.Muryaet al.2016 [32]	Prism BK7/SF11/2S2G)+ Metal Au/Ag/Cu/Al)+ MoS_2+Graphene+ Water	-	-	-	Ag furnishes the lower FWHM, which leads to high DA and QF; Cu renders high $\nabla\theta_{res}$, which leads to higher S.
M. S.Rahmanet al.2017 [34]	Prism+ Au+ MoS_2+ PBS solution	89.29	0.919	13.13	The hybrid structure of MoS_2-Grpahene is appropriated to enhance the S of the SPR sensor.
S. Palet al.2017 [33]	Prism+ Au+ BP+ Affinity+ Sensing Layer	180	0.29	-	The BP and BP-Si based structures render the highest S and DA, respectively. These are almost constant with a variation of sensing RI.
	Prism+ Au+ Si+ BP+ Affinity+ Sensing Layer	115	1.19	-	

2.11.2 SPR biosensor applications

Biosensor technology has expanded the bind illumination of DNA molecular diagnosing over and above 400 disorders, and this enumeration continues to grow. SPR sensors unfold several sensing applications for biochemical materials because of reduced pre-processing, and it can be measured in real-time. Many other researchers have employed the SPR sensor to detect DNA hybridization at visible range wavelength. Three basic desirable parameters are required for adequate SPR sensor performance, such as sensitivity, QF and DA. The RI value has been changed after incorporating phosphate-buffered saline (PBS) concentration into the structure, and the amount of shift has been measured by the subsequent expression presented in Eq. (2.15).

$$n_H = n_S + c_a \frac{dn}{dc} \tag{2.15}$$

Where, n_H is the sensing medium RI after hybridization, n_S is the sensing medium RI before hybridization, c_a is the concentration of an adsorbed molecule, and $\mathrm{dn/dc}$ is the increment in RI due to the adsorbed molecule. After its realization through current manufacturing technology, the suggested sensor can effectively diagnose complicated diseases, such as cancer and hepatitis B on DNA hybridization. For this reason, M. S. Rahman et al. showed that WS_2 based SPR sensor achieves higher resolution compared to graphene-based SPR sensor for DNA detection. This SPR sensor has the capability of distinguishing between complementary and single based mismatched DNA with a sensitivity of 95.71°/RIU at the optimal gold film [55]. Moreover, BP-based SPR sensor can detect the DNA with a sensitivity of 125 °/RIU and QF of 13.62 RIU^{-1} [56]. Two-dimensional (2D) and TDMC materials have been attractive for the enrichment of SPR sensor performance in terms of sensitivity to DNA hybridization. Further, S. Ahmed et al. suggested the WS_2-BP-based SPR sensor with a maximum sensitivity of 187°/RIU for 10 layers of BP and WS_2 monolayer. High performing sensors have prospective applications in medical diagnosis and detection of biochemical [57]. The review of the state of the art on SPR sensors for DNA hybridization has been presented in Table (2.5).

Furthermore, biomarkers can be detected in body fluids, such as saliva, urine, and blood plasma, for protein inadequacy [59]. W. Wu et al. showed protein detection performance at concentrations ranging between pg/mL to g/mL. For an instant, the levels of the human chorionic gonadotropin and the activated leukocyte cell adhesion molecule in the blood plasma of healthy individuals sojourn are approximately 1 ng/mL [60] and 100 ng/mL [59],

respectively. The numerical analysis of the germanium (Ge)-based SPR sensor has been presented with a maximum sensitivity of 132°/RIU at a thickness of 1.5 nm, where RI of protein, i.e., Bovine serum albumin is 1.435. Ge-graphene-based affords a sensitivity of 16% more than the only graphene-based SPR biosensor. Therefore, the authors concluded the Ge exhibited a better option for detecting protein detection by SPR biosensor [60].

Table 2.5 Review on SPR Sensor for DNA Hybridization

References	Configuration	Performance Parameters				Conclusion
		S (°/RIU)	DA	QF (RIU^{-1})	FOM	
M. S. Rahman et al. 2018 [44]	Prism+ Au+ WS_2+ Graphene+ Sensing Layer.	95.71	1.763	25.19	-	The sensor is capable of differentiating between the complementary and single-base mismatched DNA.
S. Pal et al.2018 [45]	Prism+ Au+ BP+ Graphene+ Sensing Layer	125	0.95	13.62	-	The sensor can work efficiently to detect the hybridization of DNA.
B. Meshgi-nqalamet al.2018 [46]	Prism+ Chromium+ Au+ BP+TDMC Material+ Sensing Layer	187.22	0.10	-	18.72	Ten layers of SPR Structure BP/monolayer WS_2 provides aimprovedS and FOM.

Besides, the kidneys play a crucial role in sustaining human health, maintaining a highly complex waste disposal arrangement. They are proficient in a continuous sorting method of non-recyclable scrap from recyclable scrap and clean the blood via filtering blood to exclude toxins and wastes. With this concern, a novel Cu-Gr-based SPR structure was designed with BSG prism for urea detection at near-infrared range wavelength. Results showed the FWHM is directly proportional to the Cu thickness at uniform urea RI of 1.49 [61]. The numerical analysis of the SPR sensor was performed at 670nm and 785nm wavelength. Urea RI fluctuates

from 1.335 to 1.347, such as 1.335, 1.337, 1.339, 1.342, and 1.347 while concentrates fluctuate at the concentrations of 0.625 ml/dl, 1.25 ml/dl, 2.5 ml/dl, 5 ml/dl, and 10 ml/dl, respectively [62]. The aluminum oxide-based sensor was proposed [63], which demonstrates 3.58% and 5.24% improvement in sensitivity at an RI of 1.33433 and the concentration of 50nM [64].

On the other hand, a waterborne disease is related bacterium, which is a world's most significant disease for health predicament. A great amount of work is required to create new technology to offer long-term drinking water [65]. Bacteria may be found in practically every part of nature that generates pathogenicity, which is both good and necessary for humans and the environment. Nearly 76 million ailments, 325000 hospitalizations, and 5000 deaths materialize in the United States each year due to food borne pathogens [66]. Contamination of bacteria from water supplies is a significant issue in developing countries and developed countries. The four bacterial pathogens, such as Salmonella species (spp.), Listeria monocytogenes, Campylobacter jejuni and Escherichia coli (E. coli) O157:H7, accounted for roughly 67% of food-related deaths. Till date, all the pathogens have been found in water supplies. Moreover, the main reservoir for entropathogenic E is humans, i.e., Enteroinvasive (E. coli), strains of enterotoxigenic E. coli, and enterohemorrhagic E. coli. A novel MoS_2-based SPR sensor was designed for identification of pseudomonas, such as bacteria by an SPR biosensor with very high efficiency. J. P. Nataro et al. have been utilized the three RI of bacteria concentration for comparing the result with other structures, such as graphene-based and conventional SPR sensors [67].

Furthermore, 17β- estradiol is one of the Endocrine-disrupting chemicals. To preserve environmental and public health, the detection of these chemicals is necessary within the natural systems by exploiting different types of investigation instrumental techniques, such as gas chromatography, mass spectrometry, and high-performance liquid chromatography. The challenge has been leading many researchers to perform a more straightforward and effective biosensor system for chemical sensing. The human estrogen receptor has been ordinarily employed for 17-estradiol ascertainment in biosensor systems [68-70]. The detection process has been performed at a linear dynamic range from 0.01 ng/mL-1000 ng/mL, with the lowest observable concentration at 10pg/mL, and with shyness ranging from 85% to 15%. IC50 signified analyte absorption of 1ng/mL inducing 50% of the SPR signal inhibition. The proposed configuration of the immunosensor is extremely specific and selective for estradiol [71]. Several harmful effects occur due to human activity and industrial development, such as various potentially dangerous human-made by-products, chemicals produced in combustion, and widespread in the environment. The principles of the SPR, test arrangement, surface

amendment methods and signal growth have been presented [72]. Also, the SPR sensor utilization has been explored in the past decade in the identification of pesticides, polycyclic aromatic hydrocarbons, heavy metals, and polychlorinated biphenyls [72]. D. Michel et al. proposed the SPR experimental set up for detecting Xanthan Gum employing Au as a metal film. The performance study demonstrated that SPR sensor was able to detect polysaccharide molecules, such as Xanthan gum up to 0.22 g/L. Moreover, the correlation between the reflected optical power and the dissolved Xanthan gum concentration was linear for the Concanavalin A, deposited on the metal film [73].

In summary, many other researchers have proposed several structure based SPR for different applications. Moreover, many proposed works have been investigated for their performances at 633nm wavelength. However, since the diseases are increasing in the world, technology is required for developing the prism-based SPR sensor, which gives high-efficient light launch at its coupling.

2.12 Survey on the Fiber Optic-based SPR Sensor

The prism-based SPR operates on TIR principle that ensues at P-M interface when the incident angle is greater than the critical angle. Therefore, the SPs excite at the surface, composing EW on either side of the P-M medium. The same principle appears in optical fiber-based SPR sensor except that the core-cladding interface is replaced instead of the P-M interface. Guided rays of the incident light pass through the core of the fiber. The EW propagates along with the core-cladding interface in the case of fiber. The SPR sensor confirms ATR principle to Kretschmann's configuration for detection mechanism. A fiber optic core–metal film–sensing medium forms the fiber-based SPR sensor for the process as presented in Fig. (2.13a). The middle portion of the cladding is extracted and coated around with thin metal films (Au, Ag, Cu, or Al) with a thickness of d; Fig. (2.13b) presents the resonance peak of fiber based SPR sensor at resonance condition employing the wavelength interrogation method. A polychromatic light source drives into one side of the fiber with decent optics and detects the transferred light at another side. J. Homola et al. reported the side polished SPR sensor with a single-mode optical fiber, which has a thin metal covering layer, represented in Fig. (2.14) [74]. Fig. (2.15) shows probe fabrication by composing and surfacing the metallic films over the etched portion of the fiber core.

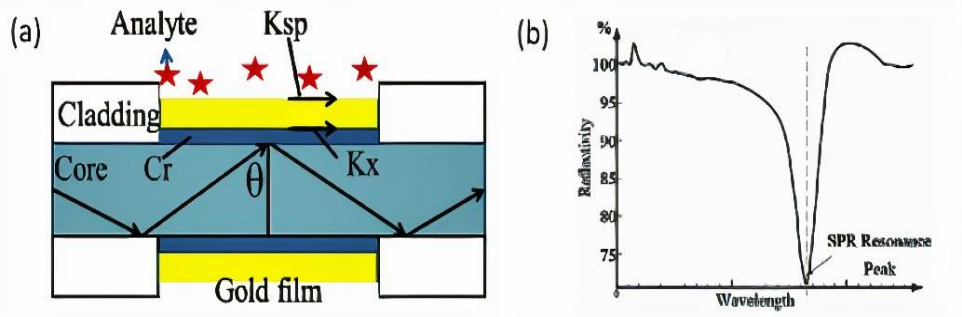

Fig. 2. 13 (a) Basic structure of optical fiber-based SPR. (b) SPR resonance peak.

A circular-shaped high-birefringence (Hi-Bi) photonic crystal fiber-based SPR sensor was designed with Finite- difference Time-domain (FDTD), and TiO_2materials. These properties were generated by FEM (Finite Element Method), utilizing the COMSOL software. The results are as follows: maximum wavelength-sensitivity (WS) 25000nm/RIU, Amplitude-sensitivity (AS) 1411 RIU^{-1} for RI 1.33-1.38 [75]. F. Wang et al. proposed the SPR sensor with two parallel photonic crystal fibers (PCF) and a D-shaped structure. Au was employed as a metal. The COMSOL software was used to analyze the performance parameters at the low RI at near-infrared (NIR) wavelength. Results showed maximum spectral sensitivity of 13,500 nm/RIU and resolution of 7.41×10^{-6} RIU at an RI range of 1.27 to 1.32 [76]. Z. Zhang et al. designed an SPR based on polymer tipped optical fiber (PTOF) with different metal materials, such as Au, Ag, Cu Al and TiO_2. Two tools, such as FDTD method and opti FDTD software, were used for performance analysis at different analyte RIs. The results achieved a sensitivity of 3798nm/RIU at analyte RI of 1.333, 5708 nm/RIU at 1.383. Therefore, this work concluded that Ag and Cu are suitable metals for PTOF-based SPR because high FOM, high sensitivity and minimum reflectivity are possible [77].

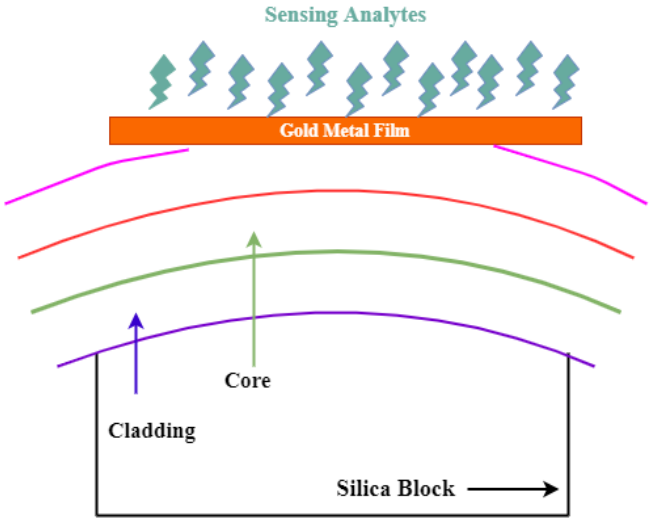

Fig. 2. 14 Side polished view of the Fiber-based SPR Sensor.

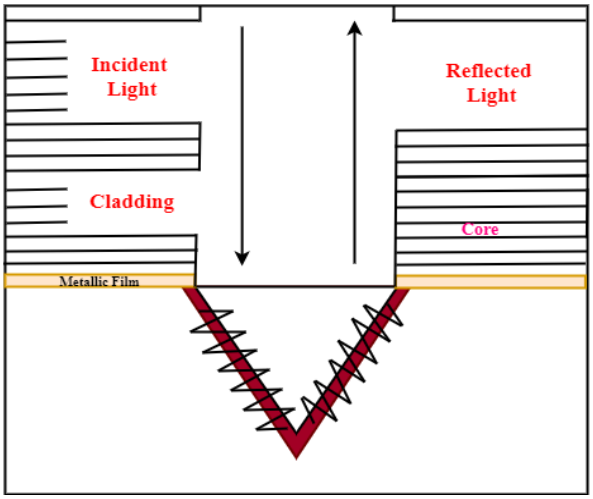

Fig. 2. 15 Fiber Optic-based SPR micro-sensor ([14], Fig. 3).

Moreover, N. Polley et al. designed the optical fiber-based sensor's periodic hole array for signal transduction, employing chemical wet lab techniques, using convenient and low-cost methods. The sensor renders the massive throughput by adopting this approach, and is ideal for commercialization, utilizing batch processing with a sensitivity of (420 $\pm$ 83) nm/RIU [78]. H. Qian et al. defined the convenient and low-cost principles for label-free biosensors, as shown in [79]. Acetylcholine was entrusted with behavioural conditions such as learning, memory, attention, excitement, and muscle contraction. Moreover, it plays an integral part in the functioning of the nervous system. K. Ravi et al. introduced the experimental operation on characterization and fabrication of fiber optic (FO)-SPR. This sensor was designed by employing Ag, Ta_2O_5, which are significantly increasing the electrical field intensity at the sensing surface. Consequently, an influential generation of SPR signal that enhances the sensitivity of the sensor has been developed [80]. V. Semwal et al. designed a novel FO-SPR employing Ag-rGO-pani as a metal film. It utilized X-ray diffraction, Fourier transforms infrared spectroscopy and Raman spectroscopy for characterization from the scanning and transmission electron microscopy. The sensor had a sensitivity of 75.09nm/pH for a pH of 11.35. Hence, the sensor unfolds several benefits, such as compact size, low cost, high S, reliability, repeatability, and remote sensing capability [81]. W. Qi et al. fabricated a novel FO-SPR with Au-graphene-staphylococcal protein A and co-modified the tilted fiber Bragg grating. The proposed sensor demonstrated huge sensitivity in detecting human immunoglobulin G. The biosensor offers several advantages, including rapid response, small size, high sensitivity, label-free and manufacturing ease. The obtained sensitivity and limit of detection are 0.096 dB/g/mL and 0.5 g/mL, respectively, for the sensor [82]. F. Zha et al. designed the PCF-SPR sensor with a D-shaped hole to use in real-time diagnostic purposes in

chemistry, biomedicine, advanced optics and chemical detection. The sensor can minimize the coupling effect and sense infiltration. The sensor had enhanced WS's performance of 14,600nm/RIU, and AS of 1475RIU^{-1}, FOM of 618 for RI varied from 1.30 to 1.42. Therefore, this sensor contributes to detecting a wide range of capabilities and has application prospects in biomedical fields [83]. Furthermore, a novel Smartphone-based sensor has been proposed by Q. Liu et al., consisting of the red-green dual colour with diffraction gratings narrow-band filters to accomplish high sensitivity, spectral data and low false detections. The SPR sensor was designed in an aqueous environment by employing the Ag/Au bi-layer structure at the centre of visible spectrum. This work was tested experimentally, and results found that the quadratic outcome in the RI range is 1.325 to 1.344 (R^2 = 0.992). The maximum noteworthy sensitivity of 18.59/RIU and a resolution of 5.3×10^{-4} RIU was achieved at the RI of linear outcome range of 1.325 to 1.330 [84]. This new structure has been confirmed an exceptional potential as the point-of-need and point-of-care platform for food protection, healthcare and knowledge of the environment, particularly in rural and remote areas. H. Fu et al. explored the theoretical basis of graphene-based FO-SPR and found better sensitivity performance compared to the conventional sensor. Theoretically, the sensor's sensitivity was amplified by 50% with 20 graphene layers [85]. Z. Fan et al. proposed Au coated PCF-SPR sensor for sensitivity analysis by considering FEM software. The performance demonstrated that sensitivity is directly proportional to RI analysis. For phase-matching conditions, three types of SPP modes and the primary modes are formed in PCF-SPR [86]. These modes work because the photon and electron resonance have been raised simultaneously with respect to RI analyte increases. The dispersion similarities of two lowest-order SP modes have emerged for a structure that comprises a thin silver sheet around a diminished fiber cladding; mode splitting was created by decreasing metal thickness. The phase-matching condition's fulfilment was tested by adopting an inventory of SPs and fiber modes [87]. Moreover, N. Cennamo et al. presented the low-cost computational and experimental reports for SPR configuration. The sensor was relayed on the plasmonic sensor platform and active higher-order filtering modes were used in the multimode plastic fiber—besides the sensor utilizing a tapered optical plastic fiber at the sensor network [88]. An RI and temperature sensor structure was designed based on hybrid mechanisms in a D-shaped all-solid photonic crystal fiber proposed in [89]. L. Peng introduced an innovative FO-SPR sensor with ring core microstructure and Ag metal film [90]. M. Li et al. developed a PCF filter that offers excellent benefits, such as narrow width and single polarization. These advantages came through a complete modal vector solver, relying on SPR theory at FEM [91]. L. C. C. Coelho et al. suggested the multiplexing of FO-SPR

sensor stationed in ladder topology, focussing on intensity analysis, and inscribed in wavelength while consolidating individual sensor with various FBGs. Results showed the highest sensitivity of 5000nm/RIU and RI resolution in the order of 10^{-4} RIU [92]. N.luan et al. proposed the exposed-core micro-structured optical fiber-SPR sensor, mounted on a silver cable [93]. A hollow fiber-based SPR sensor was intended for the realization of fast analyte RI detection [94]. N. Jing et al. introduced an SPR effect-based RI sensor [95]. S.K. Mishra et al. developed a commercial POF with a D-shaped macro-bend structure employing the heat setting and side polishing techniques in order to expose the core and enhance sensitivity for RI. In another event, S. K. Mishra et al. manufactured and characterized the profoundly sensitive FO-SPR sensor at low concentrations for ammonia gas detection [96].

2.13 Conclusion

This chapter has been described the basics of SPR sensors, including surface plasmon, and surface plasmon oscillation. Then, the sections explained the principles, different types of SPR configurations, advantages and history of SPR. Finally, it provided the latest review on prism-based and fiber optic-based SPR sensors. The literature has been investigated SPR parameters mostly at the visible range wavelength. Moreover, the investigated parameters are not reached the required standards. The literature has never mentioned the performance of dip of figure of merit (DFOM) and combined sensitive factor (CSF), which represent the overall performance of the sensor. It has focused on the performance enhancement of SPR sensors for very few applications, whereas several diseases are being discovered every day. The endorsement of SPR performance is missing in the existing literature. Therefore, this thesis looked at the possibility of coming up with a highly accurate SPR-based sensor for detecting.

Chapter-3

SPR performance enhancement for DNA hybridization employing black phosphorus, silver, and silicon

3.1 Introduction

Deoxyribonucleic acid (DNA) hybridization is a bio-molecular approach to estimate the level of inclusive relationship between successive pools of DNA, accomplishing intra-species genetic distance. Hybridized DNA sensing is a biochemical mechanism for the detection of DNA nucleotide binding between thymine (T) and adenine (A) or between cytosine(C) and guanine (G). Therefore, hybridized DNA sensing is broadly accepted in medical diagnosis [34]. This technology has been expanding to prevail the bind information of DNA molecule diagnosing more than 400 diseases, and this enumeration increasing further. Surface Plasmon Resonance (SPR) sensors can be applied to several sensing applications because of label-free and real-time analysis [97]. SPR implies an optical phenomenon described through an Electromagnetic (EM) wave interaction at the metallic-dielectric layers interface. The Surface Plasmon Waves (SPWs) are associated with the metallic surface are excited as P-polarized light passes through a metallic-dielectric interface [98]. Subsequently, SPWs oppose the light energy contained in plasmon and convert the light energy into a reflected light. Evanescent Wave (EW) is constituted on the opposite side of the interface as a consequence of the refracted photons in the Total Internal Reflection (TIR) [99]. This transmitted wave is propagated around the interface, and intensity decays exponentially in the direction perpendicular to the interface. SPR phenomenon causes resonant oscillations of SPWs and results in minimal reflectivity, which depends on the surface refractive index (RI). Therefore, minor variations in RI of the employed material in the SPR sensor transmute the resonant dip of reflected light intensity. Many other researchers also applied the Attenuated Total Reflection (ATR) method to evaluate the RI fluctuation [99]. Kretschmann and Otto have been suggested different prism-based SPR configurations comprise of metals, such as gold (Au) or silver (Ag) coating, to excite guided/leaky waves. The light penetration through the prism arises oscillations of Surface Plasmon Polarization (SPP), forming SPWs at a prism-metal interface [100], Polyvinylidence Fluoride (PVDF)-graphene [101]. Bloch surface waves produce an equivalent performance in terms of Sensitivity (S), and Figure of Merit (FOM) as SPP [102], dielectric planar waveguide mode [103]. Transparent conducting oxides (TCOs) furnish the high Detection Accuracy (DA) compared to SPP [104].

Furthermore, SPWs are adopted to detect DNA hybridization [105]. The researchers have been proposed the angular interrogation method to analyze the SPR sensor's performance accomplishing accurate measures of sensitivity [106]. Kretschmann has been presented the experimental demonstration, achieving higher outcomes using angle interrogation [9]. Au, Ag, and Copper (Cu) are commonly used metal materials in SPR sensors. However, Ag presents a high SPR ratio (the ratio between the absolute values of the real and imaginary parts of the dielectric constant) demonstrating a higher sensitivity. On the contrary, Ag experiences high susceptibility to the oxidation, compared to Au [107, 108]. To improve the sensitivity, authors in [109] have been proposed the enhanced metal film sensing surface delivering high bio-molecular absorption. The large-scale binding and adsorbent material remains the essential component for SPR sensors, and graphene is commonly adopted 2D-nano-material [110]. Moreover, graphene demonstrates high carrier mobility and optical transparency [111-113]. Therefore, graphene is widely employed in optoelectronic applications, such as touch screens, photodetectors, optical modulators, and polarizers. Black phosphorus (BP) is also a commonly accepted 2D nano-material in the photonic sensors, as a consequence of distinctive mechanical and optoelectrical characteristics. BP enhances sensing capability due to magnified interlayer coupling within the van der Waals forces, such as in graphene. The adsorption energy of BP is more significant than graphene and MoS_2, suitable for the efficient binding of biomolecules [114, 115]. A remarkable magnified sensitivity of biochemical SPR sensor by employing heterostructure of few-layer BP-graphene/TMDC materials is proposed [116]. In [56], authors presented the multi-layer SPR structure composed of graphene and Molybdenum disulfide (MoS_2) to enhance the surface biomolecular absorption and S. Moreover, to improve the DA and QF, this work has been proposed the intermediate silicon (Si) layer between Ag and graphene. It demonstrated lower Full-Width Half Maxima (FWHM), retaining acceptable sensitivity. In practice, a high-performance SPR sensor limits the FWHM to accomplish higher DA and QF. Therefore, to improve sensitivity, DA, QF and FOM simultaneously, this study proposes a novel SPR sensor employing multi-layer structures, comprising Ag, Si, BP and graphene.

3.2 Mathematical Modeling

This section presents the mathematical modeling for the proposed SPR structures employing the transfer matrix method

3.2.1 Reflectivity

Eq. (3.1) defines the wave vector component, which is perpendicular to the medium interface "j". Where ε_j is the dielectric constant of the layer, ω is the angular velocity=2πc/λ, λ is the wavelength of incident light, and subscript "j" represents the corresponding medium.

$$K_j = \sqrt{\varepsilon_j \left(\frac{\omega}{c}\right) + K_z} \tag{3.1}$$

Here, the incident wave vector component is parallel to the interface as specified Eq. (3.2).

$$K_z = \sqrt{\varepsilon_1}\,\frac{\omega}{c}\sin\theta \tag{3.2}$$

Eq. (3.3) shows the j^{th} layer's dielectric constant. Where n_j is an RI of j^{th} layer, θ is the incident angle, c is the velocity of light.

$$\varepsilon_j = \left(n_j\right)^2 \tag{3.3}$$

Eq. (3.4) presents the mathematical model to compute the reflectivity of the proposed SPR sensor.

$$R_{1234567} = \left|r_{1234567}\right|^2 = \left|\frac{(\mathrm{r}_{12} + \mathrm{r}_{234567}\ \ \mathrm{e}^{(2\mathrm{i}K_2 d_2)})}{(1 + \mathrm{r}_{12}\ \mathrm{r}_{234567}\ \ \mathrm{e}^{(2\mathrm{i}K_2 d_2)})}\right|^2 \tag{3.4}$$

$$r_{234567} = \frac{r_{23} + r_{34567}e^{2ik_3d_3}}{1 + r_{23}r_{34567}e^{2ik_3d_3}}, \quad r_{34567} = \frac{r_{34} + r_{4567}e^{2ik_4d_4}}{1 + r_{34}r_{4567}e^{2ik_4d_4}}, \quad r_{4567} = \frac{r_{45} + r_{567}e^{2ikd_5}}{1 + r_{45}r_{567}e^{2ik_5d_5}},$$

$$r_{567} = \frac{r_{56} + r_{67}e^{2ik_6d_6}}{1 + r_{56}r_{67}e^{2ik_6d_6}}, \quad r_{12} = \frac{\varepsilon_2/k_2 - \varepsilon_1/k_1}{\varepsilon_2/k_2 + \varepsilon_1/k_1}, \quad r_{23} = \frac{\varepsilon_3/k_3 - \varepsilon_2/k_2}{\varepsilon_3/k_3 + \varepsilon_2/k_2}, \quad r_{34} = \frac{\varepsilon_4/k_4 - \varepsilon_3/k_3}{\varepsilon_4/k_4 + \varepsilon_3/k_3},$$

$$r_{45} = \frac{\varepsilon_5/k_5 - \varepsilon_4/k_4}{\varepsilon_5/k_5 + \varepsilon_4/k_4}, \quad r_{56} = \frac{\varepsilon_6/k_6 - \varepsilon_5/k_5}{\varepsilon_6/k_6 + \varepsilon_5/k_5}, \quad r_{67} = \frac{\varepsilon_7/k_7 - \varepsilon_6/k_6}{\varepsilon_7/k_7 + \varepsilon_6/k_6}$$

$\mathrm{r}_{12}, \mathrm{r}_{23}, \mathrm{r}_{34}, \mathrm{r}_{45}, \mathrm{r}_{56}$ and r_{67} are the reflected amplitudes from 1-2, 2-3, 3-4, 5-6, 6-7 layers, respectively. Where d_m denotes thickness of each layer (m= 2, 3, 4, 5, 6).

3.2.2 Proposed SPR performance parameters

This work has analyzed the SPR performance of FOM along with three canonical parameters, such as sensitivity, DA and QF. High-performance SPR sensor demonstrates high sensitivity, DA, QF, and FOM considering the reflectance response employing angular interrogation technique. The resonance angle (θ_{res}) is defined as the angle where the minimal reflectivity is achieved. Eq. (3.5) defines the sensitivity as a ratio of change in the resonance angle to change in RI. Higher sensitivity represents the sensor's immediate response capability, detecting the minor difference in RI.

$$Sensitivity\ (S) = \nabla\theta_{res}/\nabla n \tag{3.5}$$

Eq. (3.6) defines the DA as a ratio of change in the resonance angle to FWHM. Superior SPR sensor demonstrates reduced FWHM achieving improved DA; moreover, enhanced DA represents the SPR sensor's capability to produce accurate outcomes. Eq. (3.7) defines the QF as a ratio of S to FWHM and Eq. (3.8) defines FOM [35].

$$DA = \nabla\theta_{res} / FHWM \tag{3.6}$$

$$QF = S / FWHM \tag{3.7}$$

$$FOM = S(1 - R_{\min}) / FWHM \tag{3.8}$$

3.2.3 Proposed SPR structure parameters

Fig. 3.1 shows the canonical diagram of the proposed work, which is established based on the Kretschmann configuration.

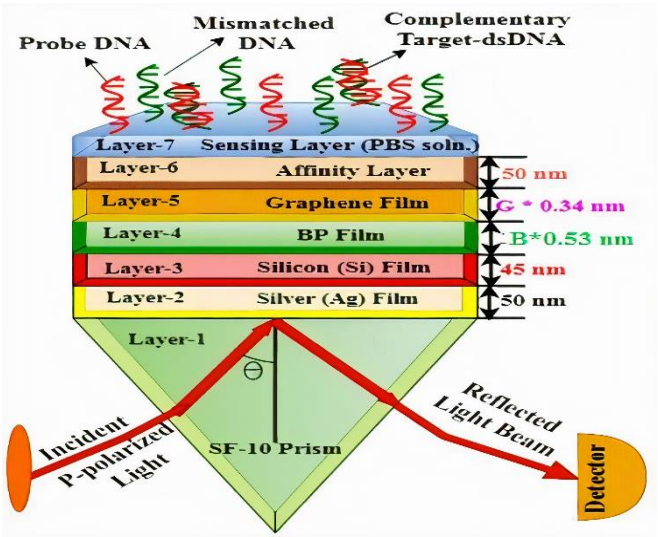

Fig. 3.1 Proposed schematic of proposed SPR sensor for DNA hydrization.

The SPR sensor structure presented in Fig. 3.1 is employed to detect the mismatched DNA event and complementary-double-stranded-DNA (dsDNA) hybridization. To obtain the enhanced S, this work has been used 633 nm wavelength [55]. Schott formula (SF-10) prism was employed as a substrate in the first layer having an RI of 1.723 [56, 117], which substantially contributes to enhancing the sensing parameters, such as sensitivity, DA, QF and FOM. The second layer is comprised of Ag, as deposited on the prism with an RI of 0.056206+4.27761i [32, 118]. The third layer is comprised of Si, as deposited on Ag with an RI of 3.916 [36]. Moreover, the thicknesses of Ag and Si are meant to achieve enhanced performance. The fourth layer is comprised of BP, as coated on the Si layer with an RI of 3.5+0.01i, which is spread nearly in nine layers with a cumulative thickness of 5 nm. The fifth layer is comprised of graphene, as coated on BP with an RI of 3+1.1487i, where BP and graphene

thicknesses are Bx0.53 nm and Gx0.34 nm, and B and G are the numbers of BP and graphene layers, respectively [56]. The sixth (affinity) and seventh (sensing) layers are Bio-Recognition Element (BRE), and Phosphate Buffered Saline (PBS) with RI of 1.625 and thickness of 50 nm, and 1.334, respectively [97, 119, 120]. This work proposes employing the PBS to achieve a carbon absorption-based ring structure, such as a single standard DNA (ssDNA). Table 3.1 summarizes the four SPR sensor structures, which were employed during this study.

Table 3.1 SPR Biosensor Structures

Structure	Combination
1. Conventional SPR	Prism (1)-Ag (2)-Sensing layer (7) (without Si, BP, graphene)
2. SPR sensor with graphene	Prism(1)-Ag(2)-Graphene(5)-Sensing layer(7) (without Si, and BP)
3. SPR sensor with BP (proposed work-1)	Prism(1)-Ag(2)-BP(4)-Graphene(5)-Sensing layer (without Si)
4. SPR sensor with silicon (proposed work-2)	Prism(1)-Ag(2)-Si(3)-BP(4)-Graphene(5)-Affinity layer(6)- Sensing layer(7)

3.3 Simulation Results

3.3.1 Thickness optimization of Ag, Si, BP and graphene layers

For the proposed SPR sensor structure-3 and 4, Ag and Si layer's thickness optimization have been conducted, retaining constant thickness for BP and graphene. The layer thickness optimization has been conducted by performing iterative simulation studies and performance analysis. To achieve the optimized thicknesses, enhanced sensitivity, lower minimum reflectance (R_{min}) and lesser FWHM are essential performance parameters during the optimization iterations. Sensitivity and R_{min} are essential parameters for Ag optimization, whereas FWHM and R_{min} for Si optimization. Resonance condition satisfies when the component of the incident wave vector, which is parallels to the interface, is equal to the propagation constant through the interface. This condition demonstrates the R_{min} gets less in SPR response because its total energy transmits to the SPW. Fig. 3.2(a) shows that S is increased with the increase of Ag thickness, but R_{min} decreases with increases of Ag thickness up to the optimized value of 50 nm. After the optimized Ag, R_{min} has been increased with Ag thickness. At 50 nm of Ag thickness, the minimum value of R_{min} and desirable S are achieved, which is intended for performance analysis. Therefore Fig. 3.2(a) confers 50 nm as the optimized thickness for Ag, demonstrating the intended R_{min} and S of 0.0034 and 91.23 °/RIU, respectively. Similarly, Fig. 3.2(b) shows the

optimization of the Si layer by employing structure-4. For the calculation of FWHM, the R_{min} must be greater than or equal to half of the maximum R_{min}. In this analysis, FWHM calculation is not possible at less than 45nm thickness. R_{min} decreases with Ag thickness increases up to the optimized value of 45 nm, but both R_{min}, and FWHM are increasing after 45 nm thickness. Hence, Fig. 3.2(b) confers 45 nm as the optimized thickness for Si, at 45nm, demonstrating the intended R_{min} and FWHM are 0.0011 and 0.05°, respectively.

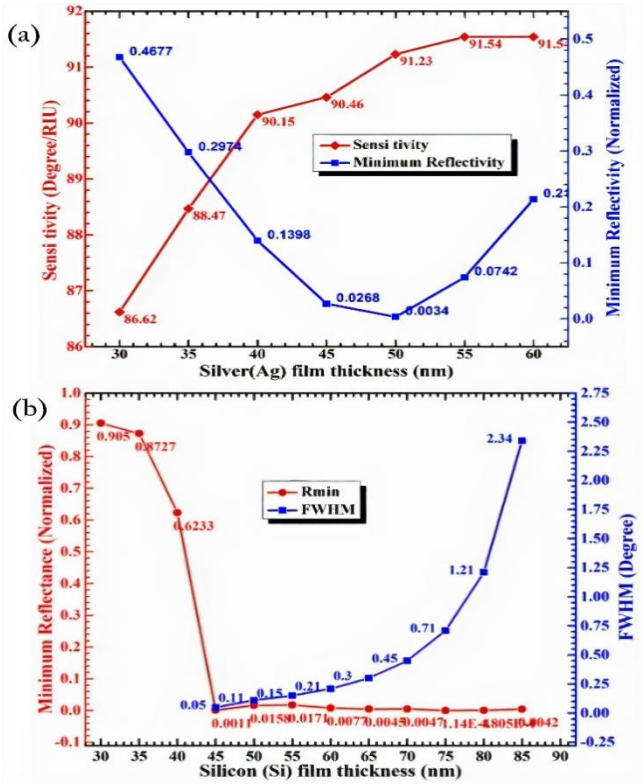

Fig. 3.2. Optimization of (a) Ag film thickness (b) Si film thickness.

Fig. 3.3(a) and 3.3(b) have presented the BP and graphene layers optimization at the optimized Ag thickness of 50 nm, respectively. The number of BP and graphene layers has been iterated within a range of 1 to 15, with an interval of 2. The iterative simulation has been studied and results has been presented in Fig. 3.3(a) and 3.3(b), revealing the resonance angles observed for BP layers as 55.09°, 50.86°, 55.72°, 56.46°, 57.33°, 58.35°, 59.57°, 62.8°, and for graphene as 58.59°, 59.19°, 59.85°, 60.56°, 61.33°, 62.20°, 63.11°, 64.13°, respectively.

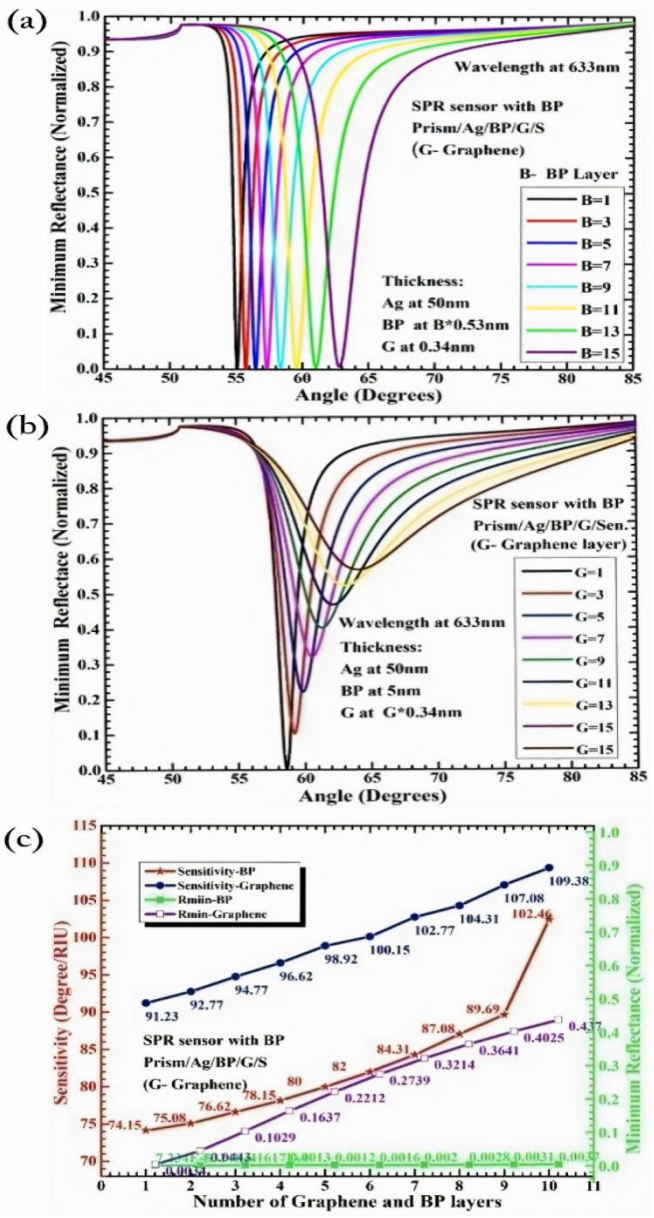

Fig. 3.3 SPR responses vs (a) BP layers (b) graphene layers, (c) SPR Parameters.

Fig. (3.3c) depicts the greater resonance angle shifts with increased number of BP or graphene layers, accomplishing the superior sensitivity. Improved sensitivity has been accomplished as a result of its properties, such as higher absorption efficiency, sluggish carrier efficient mass, and most relevant to the additional capture of charge carriers [120, 121]. This enhancement of sensitivity is acquired because of its plasmonic nanocavity [33]. Fig. 3.3(c) demonstrates the sensitivities 102.45 °/RIU for BP and 109.38 °/RIU for graphene, respectively. Although, the sensitivity is higher with increased number of graphene layers, Fig. 3.3(a), 3.3(b), and 3.3(c) show that it diminished the R_{min} for increased number of BP layers compared to graphene layers. Therefore, considering the tradeoff between the number of layers for BP and graphene deposition, for this simulation study, nearly nine BP layers were deposited for achieving the higher sensitivity and monolayer graphene, achieving diminished R_{min}.

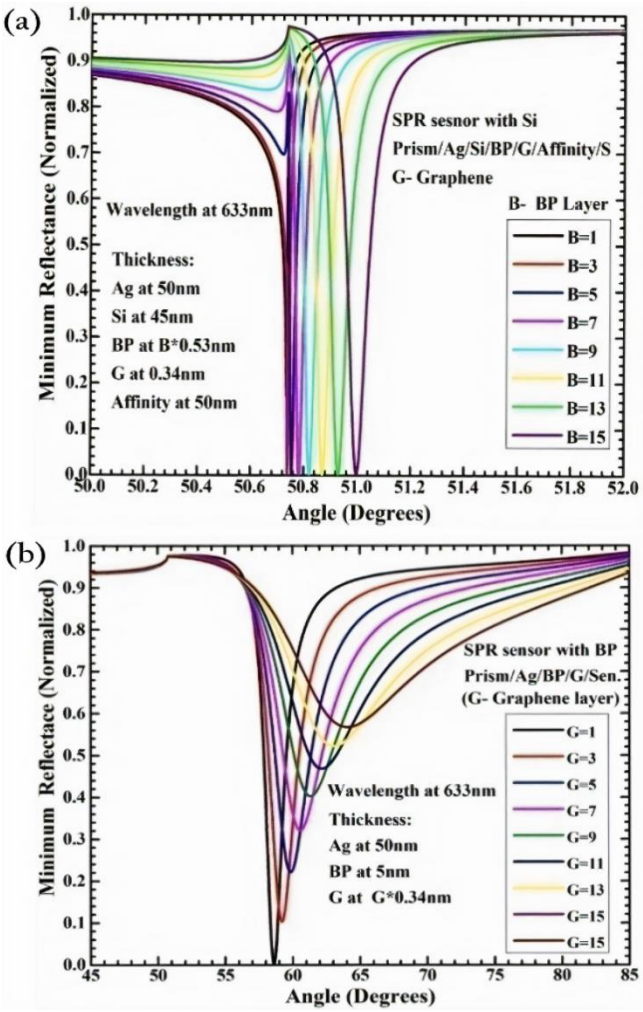

Fig. 3.4. SPR response vs (a) BP layers (b) graphene layers (Si, 45 nm).

Similarly, Fig. 3.4(a) and 3.4(b) present the BP and graphene layer optimization at the optimized Si thickness of 45nm, employing the structure-4. The observed resonance angles for variation in BP layers are 50.83°, 50.86°, 50.89°, 50.93°, 50.97°, 51.02°, 51.07°, 51.13°, and for graphene 50.74°, 50.78°, 50.82°, 50.83°, 50.87°, 50.93°, 51.0°, respectively. Fig. 3.4(a) shows the less R_{min} and increases the small amount of resonance shift with increases of BP layers. Fig. 3.4(b) shows the R_{min} increases with the additions of the graphene layer. From the definition, FWHM calculation is not possible at high RI because it's R_{min} greater than the half of the high reflectance value. Therefore, R_{min} and resonance shifts have been taken as essential parameters for optimizing the BP and graphene layers at structure-4. This simulation study comprised nearly nine BP layers achieving the higher resonance shift and monolayer graphene, producing diminished R_{min}. Table 3.2 and 3.3 have summarized the utilized parameters, such as structure configuration, RIs corresponding to the layers and desired layer thicknesses employed to achieve the outcomes for structure-3, and 4, respectively.

Table 3.2 Parameters for Optimizing Structure-3

Fig. no.	Structure	RI	Thickness
3 (a)	Prism/Ag/BP/ graphene/ Sensing layer	1.723/ 0.056206+4.27761i /3.5+0.01i/ 3 + 1.149106i/1.334	Ag = 50 nm, BP = B × 0.53 nm, (B is number of BP layers, graphene = 0.34 nm
3 (b)	Prism/Ag/BP/ graphene/ Sensing layer	1.723/ 0.056206+4.27761i/ 3.5+0.01i/ 3+1.149106i/ 1.334	Ag = 50 nm, BP = 5nm, graphene = G×0.34 nm. (G is number of graphene layers
3 (c)	Prism/Ag/BP/ graphene/ Sensing layer	1.723/ 0.056206+4.27761i/ 3.5+ 0.01i/ 3+1.149106i/ 1.334	Ag = 50 nm, BP = B ×0.53 nm, graphene = G×0.34 nm. (G is number of graphene layers

Table 3.3 Parameters for Optimizing Structure-4

Fig. no.	Structure	RI	Thickness
4 (a)	Prism/Ag/Si /BP/graphene/ affinity/ Sensing layer	1.723/3.916/ 0.056206+4.27761i/ 3.5+0.01i/ 3+1.149106i/ 1.625 /1.334	Ag = 50 nm, Si=45nm, BP= B × 0.53 nm, (B is number of BP layers), graphene = 0.34 nm, affinity=50nm
4 (b)	Prism/Ag/Si/ BP/graphen/ affinity/ Sensing layer	1.723/3.916/ 0.056206+4.27761i/ 3.5+0.01i/3+1.149106i/ 1.625/1.334	Ag = 50 nm, Si=45nm, BP = 5 nm, (B is number of BP layers), graphene = G×0.34 nm, affinity=50nm

3.3.2 Proposed SPR structures and performance comparison

Iterative simulations have been performed optimizing the Ag and Si thickness to 50 nm and 45 nm, respectively, achieving the desired performance parameters for the proposed SPR sensor. In Fig. 3.5, the solid lines show the SPR response before absorption of the ssDNA and dashed lines after absorption of the ssDNA for conventional, graphene-based, proposed work-1, and proposed work-2 SPR sensors. Fig. 5 presents the performance comparison of existing SPR sensors and proposed SPR sensors in structure-3 and 4. The red, blue, pink and cyan curves indicate the conventional, graphene-based and proposed SPR sensors (structure-3 and 4), respectively. The resonance angles and FWHMs

of different structures have been tabulated in Table 3.4. Moreover, the performance parameters, such as sensitivity, DA, QF and FOM, are computed employing Eq. (5-8) for the considered SPR sensors and reported them in Table 3.4. The proposed work-1 (structure-3) demonstrates a substantial resonance shift, indicating enhanced sensitivity of 91.54 °/RIU, which is 1.26 times higher than the conventional and graphene-based SPR sensors; however, it shown degradation in terms of DA and QF.

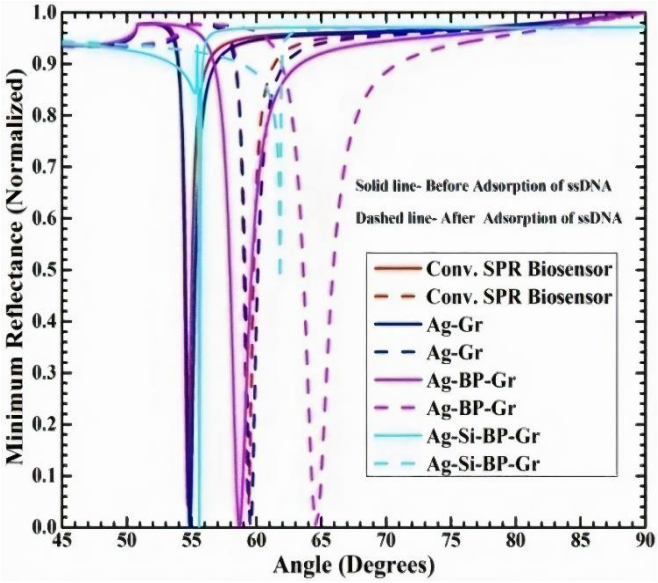

Fig. 3.5 SPR responses for pre and post DNA hybridization.

Therefore, to improve the DA and QF simultaneously, this study proposes the novel SPR sensor as presented in work-2 (structure-4). The proposed SPR sensor enhances the DA of 69 and QF of 1061.6 RIU^{-1}, which is 8.53, and 11.04 times higher compared to both conventional and graphene-based SPR sensors, respectively. Furthermore, the SPR sensor proposed a new performance parameter FOM, which no existed work has been offered. The proposed sensor confers an FOM of 554.58, which is the 4.47, and 5.77 times higher than the conventional and graphene-based SPR sensors, respectively.

3.3.3 Detection principle

The binding of the ssDNA target and the ssDNA probe results in dsDNA hybridization. At the instance of the ssDNA target is merged in PBS solution, which results in RI variation of the sensing region and commences DNA hybridization conforming to the molecular concentration. Subsequently, DNA hybridization drives a significant resonance shift as the propagation constant of the SPW enforces the re-distribution of the EM field. Eq. (3.9) computes the sensing layer's RI according to the PBS solution's concentration in the sensing layer [117].

$$n_d = n_a + c_a \, dn/dc \tag{3.9}$$

Where, n_d is the RI of the sensing layer at post DNA molecules absorption, c_a is the concentration of the adsorbed molecules, n_a is the increase in RI as a consequence of adsorption. The parameter dn/dc=0.182 cm^2/gm is utilized in the case of a standard buffer solution [117].

Table 3.4 Performance Parameters for Pre and Post DNA Hybridization

Structure	Conv. SPR	Ag/Gr	Ag/BP/Gr	Ag/Si/ BP/Gr
θ_{res}(°)-before ssDNA adsorption	54.68	54.86	58.69	55.88
θ_{res}(°)-after ssDNA adsorption	59.37	59.55	64.56	62.33
$\Delta\theta_{res}$ (°)	4.69	4.69	5.93	3.45
R_{min}(%)	2.6×10^{-3}	9.29×10^{-4}	6×10^{-4}	0.4776
FWHM	0.58	0.75	1.67	0.05
S ($°/RIU$)	72.15	72.15	91.54	53.08
DA	8.09	6.25	3.61	69
QF (RIU^{-1})	124.4	96.2	54.81	1061.6
FOM	124.07	96.11	54.78	554.58

Fig. 3.6(a) presents the minimum reflectance based on DNA hybridization method before and after the probe DNA for the proposed SPR sensors structure-3 and 4. The red and cyan curves intimate the event of pre and post-DNA addition, demonstrating the resonance angles of 58.27° and 59.09°, respectively, for the proposed SPR sensor structure-3. Similarly, blue and pink curves demonstrate the resonance angles of 50.63° and 51.13°, respectively, for the proposed SPR sensor structure-4. Therefore, the addition of probe DNA in both structures, constitute a substantial shift in the resonance angles of 0.82° and 0.5°, respectively. The electron-rich molecules in DNAs are responsible for changing the carrier concentration in the BP-graphene region, which changes the propagation constant of SPW and RI of the sensing region. The sensing layer is comprised of probe DNA pre-immobilized on graphene surface and PBS solution containing mismatched DNA.

Fig. 3.6(b) depicts the SPR response before (bare SPR) and after (probe DNA) combining DNA molecules, and mismatched target DNA for the proposed SPR structures-3 and 4. The cyan, red

and gray curves demonstrate the resonance angles of 58.27°, 59.09°, and 59.19°, respectively, for the proposed SPR sensor structure-3.

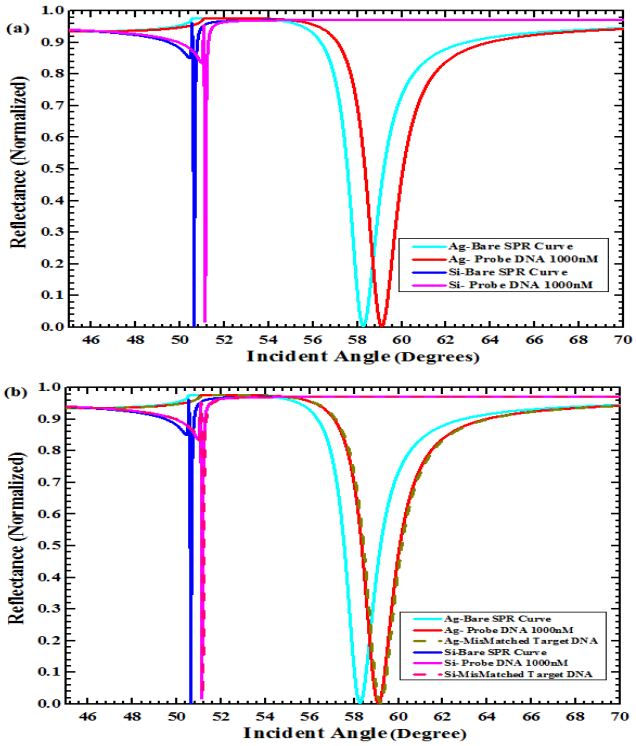

Fig. 3.6 (a) pre and post (b) pre, post and mismatched target DNA insertion.

Similarly, the blue, pink and green curves demonstrate the resonance angles of 50.63°, 51.13° and 51.18°, respectively, for the proposed SPR sensor structure-4. The observed deviations in the resonance angles are 0.1° and 0.05° post introduction of non-complementary DNA in the sensing layer, respectively, for structure-3 and 4. The resonance shifts are occurred due to the absence of hydrogen bonding between the mismatched pair and signify the absence of DNA hybridization. Consequently, it can be stated that there are no associated charges with the target DNA molecule that can incorporate a distinct change to the applied sensing region. Therefore, the proposed sensors are capable of distinguishing between mutations and Single Nucleotide Polymorphism (SNP) [97]. The proposed SPR sensor (structure -4) contributes to FWHM changes, such as 0.1°, 0.05°, which leads to improved accuracy, quality and resolution. Si affords higher-resolution performance than the Ag because of its property of an abundant electropositive element.

Fig. 3.7 (a) presents the SPR responses considering the hybridization between 1000nM DNA (red curve) and complementary DNA with various molar concentrations, such as 1000nM (blue curve), 1001nM (green curve), 1010nM (magenta curve) and 1100nM (cyan curve), demonstrating resonance angles of 59.09°, 60.39°, 60.64°, 60.74°, and 60.82°, respectively, for the proposed SPR sensor structure-3. Similarly, 1000nM DNA (red dashed) and 1000nM (blue dashed), 1001nM (green dashed),

1010nM (magenta dashed) and 1100nM (cyan dashed) have led to resonance angles of 51.13°, 51.91°, 52.06°, 52.11°, and 52.18°, respectively, for the proposed SPR sensor structure-4.

Table 3.5 θ_{res} and R_{min} with Increasing CT DNA for Structure-3

DNA concentration c_a in (nM)	θ_{res}(°)	$R_{\min}$	$\delta\theta_{SPR}^{P-T}$(°)	δR_{SPR}^{P-T}(%)
1000 [probe]	59.09	0..003467	-	-
1000 [CT]	60.39	0.003463	1.3	4×10^{-6}
1001 [CT]	60.64	0.003406	1.55	6.1×10^{-5}
1010 [CT]	60.74	0.003447	1.65	2×10^{-5}
1100 [CT]	60.82	0.003436	1.73	3.1×10^{-5}

Table 3.6 θ_{res} and R_{min} with Increasing CT DNA for Structure-4

DNA concentration c_a in (nM)	θ_{res}(°)	$R_{\min}$	$\delta\theta_{SPR}^{P-T}$(°)	δR_{SPR}^{P-T}(%)
1000 [probe]	51.13	0..01792	-	0.016835
1000 [CT]	51.91	0.001085	0.78	0.007931
1001 [CT]	52.06	0.09723	0.93	0.15758
1010 [CT]	52.11	0.1755	0.98	0.25268
1100 [CT]	52.18	0.2706	1.05	0.016835

Besides, Table 5 and 6 summarize the resonance angles and $R_{\min}$ values corresponding to the variation in complementary DNA concentration for the proposed SPR sensor structure-3 and 4, respectively. Moreover, Fig. 3.7 (a), and Table 3.5 and 3.6 are revealed that as the molecular concentration of complementary target DNA increases with RI variation in the sensing layer, further results in the higher value's resonance angle shift. Therefore, minor variations in the molecular concentration in the sensing layer have been detected, showing the resonance angle shifts. Eq. (3.10-3.11) are used to compute the variation in resonance angle and $R_{\min}$ correlate it to the molecular concentration of DNA in the sensing layer.

$$\delta\theta_{SPR}^{P-T}(^\circ) = \left|\theta_{SPR}^{Probe} - \theta_{SPR}^{Target}\right| \tag{3.10}$$

$$\delta R_{\min}^{P-T}(\%) = \left|R_{\min}^{Probe} - R_{\min}^{Target}\right| \tag{3.11}$$

Where, the attributes of θ_{SPR}^{Probe}, R_{min}^{Probe}, θ_{SPR}^{Target}, R_{min}^{Target} are the resonance angle and R_{min} for probe and complementary target DNA, respectively. The complementary target DNA molecules interact with the graphene surface during the DNA hybridization and commence the n-doping effect [119, 121 and 123]. The attributes mentioned above are employed to detect the DNA hybridization process.

From Table 3.5, it has been observed that when the hybridization occurs between 1000nM DNA and complementary DNA, the observed $\delta\theta_{SPR}^{P-T}(°)$ and $\delta R_{min}^{P-T}(\%)$ are 1.3 and 4×10^{-6} for the proposed SPR sensor structure-3. Similarly, from Table 3.5, it has been noticed the observed $\delta\theta_{SPR}^{P-T}(°)$ and $\delta R_{min}^{P-T}(\%)$ values are 0.78° and 0.016835, respectively, for the proposed SPR sensor structure-4. Therefore, observing the shift in resonance angle $[\delta\theta_{SPR}^{P-T}(°) > min(\delta\theta_{SPR}^{P-T}(°))]$ and minimum reflectivity $\delta R_{min}^{P-T}(\%) > min(\delta R_{min}^{P-T}(\%))]$ indicates the successful detection of DNA hybridization. On the contrary, at the violation of the mentioned conditions, indicate the absence of DNA hybridization. Furthermore, Fig. 3.7(b) exhibited the variation in $\delta\theta_{SPR}^{P-T}(°)$ and $\delta R_{min}^{P-T}(\%)$, conserving the DNA concentration. The significant shift in $\delta\theta_{SPR}^{P-T}(°)$ and $\delta R_{min}^{P-T}(\%)$ have been observed as the DNA concentration is increasing. Also, the proposed SPR sensor structure-3 (w/o Si) has been demonstrated a high resonance shift, which leads to a higher sensitivity than the structure-4 (with Si). Enhanced sensitivity has been achieved by employing structure-4 as a result of higher absorption capability of BP and graphene. The reason for achieving higher sensitivity for the proposed designated structure using BP/graphene layers is due to the higher penetration depth of the evanescent field in biomolecular sensing layer because of its higher real part of RI and a smaller value of its imaginary part causing low energy losses [35]. On the other hand, structure-4 demonstrated that R_{min} is reduced at high DNA concentrations, signifying reduced reflected energy and higher transmitted energy to SPW. Therefore, structure-4 is accomplished the substantial improvement in DA and QF along with the desired sensitivity.

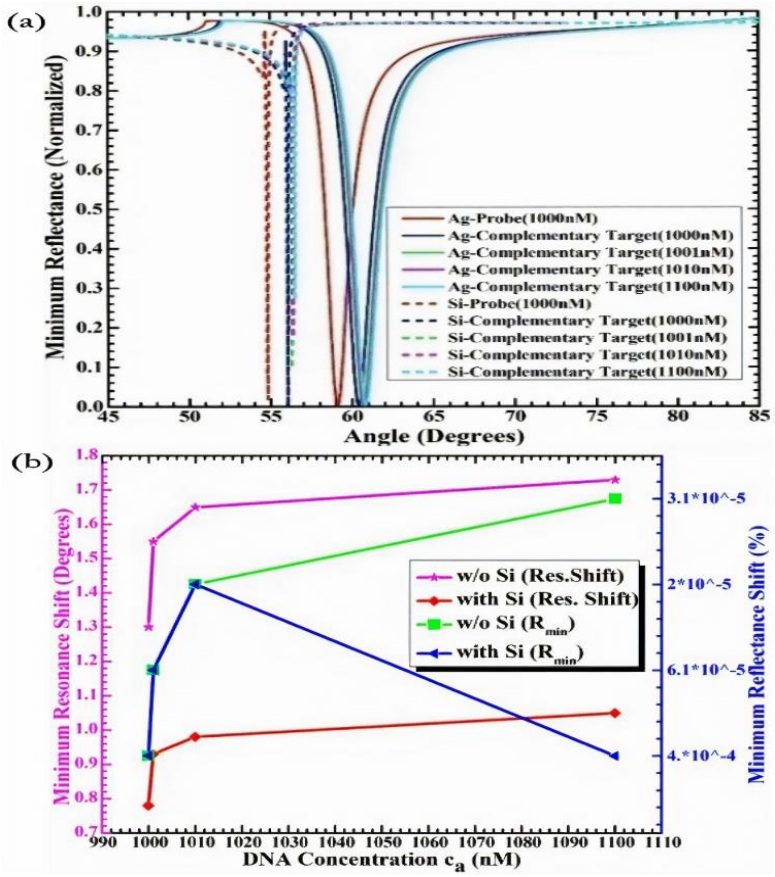

Fig. 3.7 (a) Variation in CT-DNA molecule concentration (b) SPR parameters.

3.3.4 Performance analysis: a comparative study

Finally, Table 3.7 presents the comparative study between the proposed SPR sensor structure-3 (work-1), structure-4 (work-2) and existing sensors. Structure-3 accomplishes the enhanced sensitivity of 91.54°/RIU employing a combination of Ag and BP. However, minor degradation in DA and QF is observed. To enhance the DA and QF, Si layer is employed in structure-4, accomplishing the enhanced DA and QF of 69, and 1061.6 RIU^{-1}, respectively. Therefore, structure-4 is achieved a higher position compared with the existing SPR sensors. Moreover, the FOM performance are also computed using Eq. (8) and found FOM of 54.78 and 554.58 for structure-3 (work-1) and structure-4 (work-2), respectively. Structure-4 improved FOM of 10.12 times higher than structure-3. Therefore, the present numerical simulation analysis has been revealed that the proposed SPR sensor structure-4 (work-2) leads to agreeable solution for detecting DNA hybridization, with high sensitivity, QF, DA and FOM.

Table 3.7 Comparative study on the Proposed Work with Existing Works

S. no.	Reference	Structure used	S (°/RIU)	DA	QF (RIU^{-1})	FOM
1	Rahman et al. 2017 [97]	SF-10 Prism-Au-graphene-MoS_2-PBS solution	87.8	1.28	17.56	-
2	Wu et al. 2107 [116]	BK-7 Prism-Ag-BP-graphene-5-layer-sensing layer	217	-	-	-
3	Saika et al. 2017 [55]	SF-10 Prism-Au-BP-graphene-PBS solution	125	0.95	13.62	-
4	Alka et al. 2015 [117]	SF-10 Prism-Au-graphene-affinity layer-sensing layer	33.98	0.298	2.78	-
5	Maurya el. al. 2015 [32]	SF-10 Prism-Au-graphene-Affinity-sensing layer	27.29	4.16	4.12	-
6	Proposed work-1	SF-10 Prism -Ag - BP-graphene Layer-PBS solution	91.54	3.61	54.81	54.78
7	Proposed work-2	SF-10 Prism-Ag-Si-BP-graphene Layer- affinity-PBS solution	53.08	69	1061.6	554.58

3.4 Conclusion

This work has been presented two SPR sensor structures employing a combination of Ag, Si, BP and graphene for accomplishing the superior performance parameters, such as sensitivity, DA, QF and FOM. The literature shows the research studies that have been performed to modify the SPR structure to improve the sensitivity. However, the degradation in DA and QF remain unaddressed. On the other hand, the proposed SPR sensor structures have demonstrated enhanced sensitivity, DA, QF and FOM compared to conventional and graphene-based SPR sensors by adopting optimized thickness of Ag and Si. Moreover, the proposed structure-3 demonstrated higher sensitivity of 91.54 °/RIU, which is 1.26 times greater than conventional and graphene-based SPR sensor. However, minor degradation in DA and QF is observed, whereas the proposed structure-4 with Si layer accomplished the DA of 69 and QF of 1061.6 RIU^{-1}, which are (both DA and QF) 8.53 and 11.04 times higher

compared to conventional and graphene-based SPR sensor, respectively. Moreover, the maximum FOM value of 554.58 is achieved for proposed sensor, which shows 4.47 and 5.77 times higher than conventional and the graphene-based SPR sensors, respectively. After its realization through the existed manufacturing technology, the proposed sensors can effectively diagnose multifarious diseases, such as cancer and hepatitis-B, based on DNA hybridization.

Chapter-4

Sensitivity enhancement of the SPR biosensor for Pseudomonas bacterial detection employing a silicon-barium titanate structure

4.1 Introduction

Pseudomonas infections are diseases of the genus caused by bacteria commonly surviving in soil, water, and plants. Pseudomonas infections can be obtained in a healthy person, and the disease may spread to various areas of the human body, such as the blood, skin, ear and lungs. Pseudomonas bacteria species are saprophytic, but some are associated with humans due to opportunistic infections. The high mortality rates in such diseases reduces antibiotics' resistance power, weakens the immune system, and diminishes bacterial exoenzyme development. The potential modes of transmission of such bacteria are polluted water and food [125-128]. Therefore, to overcome the issue discussed in the previous chapter as well as to detect the Pseudomonas bacteria, this section presents an SPR oriented sensor structure, which is a promising solution [129, 130 and 47]. Researchers have been begun exploring the SPR sensor structures in Pseudomonas bacterial detection [128, 131-133]; however, complete succession is still elusive. Based on the light coupling mechanism, the SPR sensors are categorized into different types, such as grating coupled, prism coupled, waveguide coupled, and fiber optic SPR sensors. Among all the types, the prism coupled SPR sensors are preferable as they can be easily realized while other sensors suffer from the inefficient launching of light inside the fiber [134]. To simulate the guided or leaky waves, SPR sensor is utilized in two configurations, such as the Kretschmann configuration that comprised of a metal film on the prism's surface, and Otto configuration that carries air between the prism-metal interface [100, 135].

In SPR geometry, when an incident electromagnetic (EM) wave passes through a prism at a higher angle than a critical angle, it penetrates the surface, and produces surface plasmon waves (SPWs) on the prism-metal (P-M) interface due to the oscillations of surface plasmon polaritons (SPPs). Moreover, the evanescent wave (EW) excites by the SPWs at the metal-dielectric (M-D) interface when the EW wave vector is equal to the SPWs. The intensity of EW crumbles exponentially with a perpendicular direction to the P-M interface [33]. Consequently, the SPWs is opposed the light energy contained in the Plasmon, and transformed it into reflected light. The SPR phenomenon induces the resonant oscillations of SPW that depend on the refractive index (RI) of the surface, results in minimal reflectivity [99]. Therefore, the resonance dip of reflected light intensity transmutes minute RI variations

of the employed material in the SPR sensor. To test the RI fluctuations, the researchers have been utilized the Attenuated Total Reflection (ATR) approach and analyzed sensitivity and Figure of Merit (FOM) [99, 103, 109]. In [105, 106], the researchers employed the SPWs oriented SPR for the bacterial detection, and results demonstrated that the angular interrogation approach provides the accurate sensitivity measurements.

Gold (Au), silver (Ag) and copper (Cu) are commonly employed metal films for the SPR sensor; however, Ag exhibits a high SPR ratio (the ratio between the absolute values of the real and imaginary parts of the dielectric constant), promising the highest sensitivity. On the contrary, Ag faces high susceptibility to oxidation compared to Au [107]. The conventional prism-based SPR biosensor with a single metal offers lower sensitivity performance; however, enhancing the sensitivity is the ultimate goal of all researchers. Subsequently, many other authors have proposed hybrid structures of SPR sensors with a combination of dielectric materials to enhance the sensitivity performance [108]. It is essential for the SPR sensors that the elementary components survive the large-scale binding and adsorbent material. Therefore, Black phosphorus (BP) is a commonly acceptable two-dimensional (2D) material compared to graphene and molybdenum disulfide (MoS_2) on account of higher adsorption energy, which efficiently binds the biomolecules [56]. Also, BP has been a widely recognized 2D nano-material in photonic sensors as an outgrowth of distinctive mechanical and optoelectrical properties [115, 116 and 136]. Furthermore, the Silicon (Si) contributes a sharp resonance dip resulting in a higher quality factor (QF) [137]. In [138], the authors proposed a Si-BP-based SPR sensor and results observed that the performances of QF and FOM are 8.53, 4.47 times higher than the conventional SPR sensor and graphene-based sensors, respectively. Moreover, SPR requires substantial resonance shifts for enhancing the performance parameters [114]. Therefore, Barium titanate ($BaTiO_3$) is one of the commonly employed dielectric materials on account of its unique properties, such as low dielectric losses, high RI and high dielectric constant, translating minute RI variations into higher sensitivity [139, 140]. Besides, an essential phenomenon for SPR sensing is the bonding of Pseudomonas with an affinity layer. Researchers have been demonstrated many bacterial attachments of Pseudomonas over the affinity layer, such as toluene, nicotine for carbon sources, and poly (trifluoroethyl methacrylate) for hydrophobic plastic, with no or little surface charge [141].

Therefore, this work presents a novel SPR sensor by employing the Si-$BaTiO_3$ structure to detect Pseudomonas bacteria. The proposed structure is sandwiched between the Ag and BP; the affinity layer has been deployed as a protection layer for the detection process. Moreover, three different types of affinity layers have been employed, such as toluene, nicotine, and poly (trifluoroethyl methacrylate). The literature is demonstrated that S decreases after adding Si to an SPR structure;

however, this proposed novel SPR sensor employing Si-$BaTiO_3$ structure generates the highest sensitivity and FOM for detecting Pseudomonas bacteria.

4.2 Design and Methodology

This subsection exhibits the design consideration, and methodology for the proposed SPR structure.

4.2.1 Design consideration for the proposed SPR sensor

Fig. 4.1 presents the proposed Si-$BaTiO_3$ oriented SPR biosensor in Pseudomonas bacterial detection. In this design, the borosilicate glass (BK7) prism is employed as a substrate in the first layer for coupling the incident light at a wavelength (λ) of 633nm. Eq. (4.1) computes the prism's RI, which is 1.5151 at a λ of 633nm [114]. The second layer is comprised of Ag, coated on the surface of the prism with the RI of 0.056260+4.2776i, which is obtained by applying Eq. (4.2) [142, 143].

$$n_{BK7} = \left(1 + \frac{1.0396\lambda^2}{\lambda^2 - 0.006} + \frac{1.0105\lambda^2}{\lambda^2 - 103.5607} + \frac{0.2318\lambda^2}{\lambda^2 - 0.02}\right)^{1/2} \tag{4.1}$$

$$n_{Ag} = \left(1 - \frac{\lambda^2 \lambda_c}{\lambda_p^2(\lambda_c + i\lambda)}\right) \tag{4.2}$$

Table 4.1 Different Structures and configurations

Structure	Configuration
1. with **$BaTiO_3$**	BK7(1)-Ag(2)- **$BaTiO_3$**-BP(5)-Affinity(6)-Sensing layer(6)
2. with Si	BK7(1)-Ag(2)-Si(3)-BP(5)-Affinity(6)-Sensing layer(7)
3. with Si-**$BaTiO_3$** (Proposed Work)	BK7(1)-Ag(2)-Si(3)- $BaTiO_3$ (4)-BP(5)-Affinity(6)-Sensing layer(7)

Furthermore, the third layer is comprised of Si as deployed on the Ag with the RI of 3.960 [144]. The optimal thicknesses for the metal film and Si are derived through the iterative optimization method. Where, $\lambda_c = 1.7614 \times 10^{-5}$ meter (m) indicates the wavelength of collision (the collision of two atoms in a given volume), and $\lambda_p = 1.4541 \times 10^{-7}$ m represents the wavelength of plasma (the plasma oscillation wavelength) [145]. The fourth layer is comprised of $BaTiO_3$ as deposited on Si with the RI of 2.4042 [128, 38] and thickness of 5nm, which was furnished higher SPR performance in [128]. The fifth layer is comprised of BP, coated on $BaTiO_3$, with the RI of 3.5+0.01i and thickness of 0.53nm [138]. The proposed structure equips the affinity layer as the sixth layer to protect the detection mechanism, which involves the pseudomonas bacterial adsorption on the BP layer's surface. Furthermore, this study is considered three different RI values of the affinity layer to expose the Pseudomonas bacteria, such as 1.437 [poly (trifluoroethyl methacrylate)], 1.49368 (toluene) and 1.5265

(nicotine) with a composite thickness of 3nm [128, 134]. Finally, the seventh layer is a sensing medium with the RI of 1.33. In bacteria's presence, the sensing medium's RI varies from 1.33 to 1.34, relying on the culture concentration and motility [114]. Table 4.1 shows the three SPR sensor structures and their configurations, which have been throughout this work.

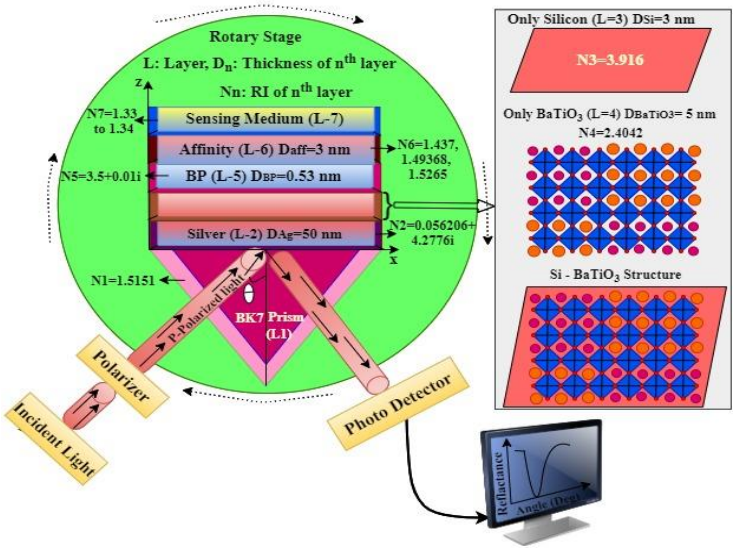

Fig. 4.1 Schematic diagram of the proposed Si-$BaTiO_3$ oriented SPR sensor.

4.2.2 SPR sensor Methodology for the proposed SPR sensor

As shown in Fig. 1, a monochromatic light source at 633 nm wavelength has been utilized in this work, and the respective data are generated in a computer-associated spectrometer. The numerical analysis of the proposed SPR sensor is studied by employing the Fresnel multilayer reflection theory and the transfer matrix method. The incident light is propagated into the prism at the wavelength (λ), and the reflected wave transpired at the P-M interface, generating the EW wave. The EW with the propagation constant (PC) of incident wave vector (k_x)through the Si layer and propagates along the x-direction. Minimum reflection transpires at the resonance condition, where it can satisfy a condition that he PC of k_x is equal to the wave vector of SPs (k_{spw}), controlled by the theta as expressed in Eq. (4.3) and (4.4). Eq. (4.5) computes the SPR resonance angle (θ_{res}), which is defined as the angle where the minimum reflection is attained.

$$k_x = k_{spw} \tag{4.3}$$

$$\frac{2\pi}{\lambda_{633}}\left(n_p \sin\theta\right) = \frac{2\pi}{\lambda_{633}}\sqrt{\frac{n_{Ag}^2 n_{AlAs}^2}{n_{Ag}^2 + n_{AlAs}^2}} \tag{4.4}$$

$$\theta_{SPR} = \left(\sin\sqrt{\frac{n_{Ag}^2 n_s^2}{n_{BK7}^2\left(n_{Ag}^2 + n_s^2\right)}}\right)^{-1} \tag{4.5}$$

Where, n_{Ag}, n_{Si} and n_S are the RI of Ag, Si and sensing medium, respectively. This work has been implemented the angular modulation procedure to study the proposed composition. Moreover, we utilized the Fresnel multilayer reflection theory and transfer matrix method to investigate P−polarized incident light wave reflectivity. The plot between the total reflected intensity (R_p) and incidence angle is referred to as the SPR curve. The mathematical expression for measuring the R_p is mentioned in Eq. (4.6), representing Fresnel's R_p model analysis [146, 147], whereas r_p represents the reflection coefficient as Eq. (4.7). Further, Eq. (4.8) represents a description of the transverse RI [40]. In Eq. (4.7), H is the characteristics matrix of the SPR structure sensor, which can be derived through Eq. (4.9) [149]. Furthermore, Eq. (4.10) computes the arbitrary stage constant β_k for the k^{th} layer [150].

$$R_p = r_p r_p^* = \left| r_p \right|^2 \tag{4.6}$$

$$r_p = \frac{(H_{11} + H_{12} n_N) - (H_{21} + H_{22} n_N)}{(H_{11} + H_{12} n_N) + (H_{21} + H_{22} n_N)} \tag{4.7}$$

$$n_k = \left[\frac{\mu_k}{\varepsilon_k} \right]^{1/2} \cos\theta_k = \sqrt{\frac{\varepsilon_k - (n_p \sin\theta)^2}{\varepsilon_k^2}} \tag{4.8}$$

$$H_{if} = \left[\prod_{k=2}^{N-1} \begin{pmatrix} \cos\beta_k & -i\sin\beta_k \\ -i n_k \sin\beta_k & \cos\beta_k \end{pmatrix} \right]_{if} = \begin{bmatrix} H_{11} & H_{12} \\ H_{21} & H_{22} \end{bmatrix} \tag{4.9}$$

$$\beta_k = \frac{2\pi}{\lambda} n_k \cos\theta_k (z_k - z_{k-1}) = \frac{2\pi}{\lambda} d_k \sqrt{\varepsilon_k - (n_p \sin\theta)^2} \tag{4.10}$$

Eq. (4.11) computes the k^{th} layer's wave impedance, which is represented as z_k [150]. Finally, Eq. (4.12) estimates the angle of input θ_k for a k^{th} layer [150]. Where, ε_k and d_k represent permittivity and thickness of the k^{th} layer, respectively.

$$z_k = \frac{k_x n_k \cos\theta_k}{(2\pi c/\lambda_{633})\varepsilon_k^2} \tag{4.11}$$

$$\theta_k = \left(\cos\sqrt{1 - (n_{k-1}/n_k)(\sin\theta)^2} \right)^{-1} \tag{4.12}$$

4.2.3 SPR performance parameter

Sensitivity is an essential parameter for the attainment of the SPR biosensor efficiency. Eq. (4.13) describes the sensitivity as the ratio of change in SPR resonance angle ($\nabla\theta_{SPR}$) to change in the RI (∇n) [138]. Sensitivity is considered as an essential performance parameter to measure the SPR biosensor's efficiency. Eq. (4.14) and (4.15) compute the QF and FOM, which are further derived from sensitivity and used to measure the SPR sensor's performance [138, 151]. Where, FWHM signifies the full width half maximum that can be computed by the difference of higher and lower angle at 50% of the SPR response.

$$S = \frac{\nabla \theta_{res}}{\nabla n} \tag{4.13}$$

$$QF = \frac{S}{FWHM} \tag{4.14}$$

$$FOM = S \times \frac{1 - R_{\min}}{FWHM} \tag{4.15}$$

4.3 Results and discussion

4.3.1 Thickness optimization of Ag and Si

As portrayed in Fig. 4.1, the proposed SPR sensor is designed by employing the Si-$BaTiO_3$ structure between Ag and BP layers. This work performed the iterative simulation study by exploiting the transfer matrix method and measured the SPR performance parameters as presented subsequently. The proposed structure requires optimized Ag's thicknesses at a constant thickness of the residual layers such as $BaTiO_3$, BP and affinity layer for analysis. The minimum reflection (R_{min}) occurs at the resonance condition, where it can satisfy the PC of k_x is equal to the k_{spw}, which is controlled by the incident angle. Fig. 4.2(a)-(d) represent the R_{min} measured with angular interrogation method for various thicknesses of Ag (40-55 nm) and of Si (1-4 nm) at constant thicknesses of $BaTiO_3$, BP and affinity layers, i.e., 5nm, 0.53nm and 3nm, respectively.

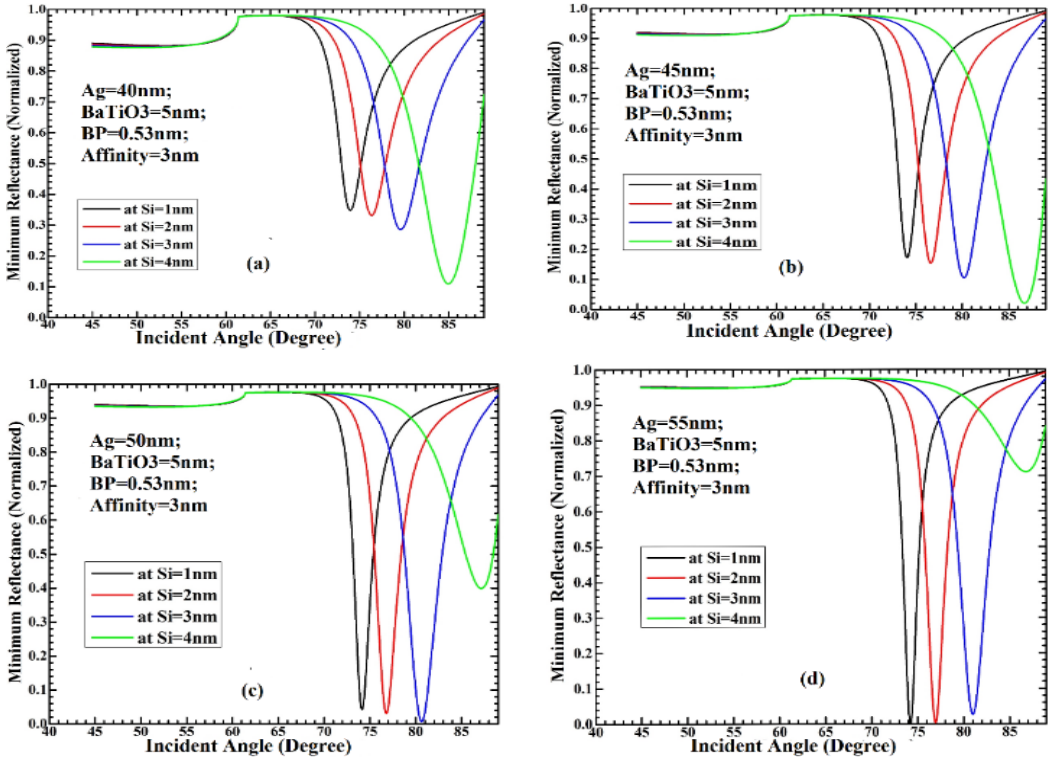

Fig. 4.2 Reflectance curves at (a) Ag of 40 nm (b) Ag of 45 nm (c) Ag of 50 nm (d) Ag of 55.

The reason for these constant thicknesses of $BaTiO_3$ and affinity is that N. Mudgal et al. proposed a high performing SPR structure with $BaTiO_3$ and affinity thicknesses of 5nm and 3nm,

respectively [128]. In addition, beyond these thicknesses, the sensor becomes absorbent, leading to high damping or attenuation in the SPR response. It signifies low SPR performance that demonstrates reduced transmitted energy and higher reflected energy to SPW [33]. Furthermore, in [128, 131 and 132], the authors used the poly affinity medium initially (RI of 1.437) to investigate the optimal structure by applying the iteration method. Therefore, this work also considered the poly affinity medium with an RI of 1.432 that offers low absorption loss [33] for analyzing optimized structure. These respective thicknesses are employed for the remaining affinity RIs mediums' performances (1.49368 and 1.5265). For accurate affinity ranking and stoichiometric computations, SPR curves should be normalized [152].

Fig. 4.2(a) depicts R_{min} response at a constant Ag thickness of 40nm with various Si layer thicknesses such as 1, 2, 3 and 4nm. The measured resonance angle and R_{min} (degree (normalized)) pairs are 73.94° (0.3478), 76.36° (0.3314), 79.62° (0.2856), and 84.95° (0.1095) for the Si layer of 1, 2, 3 and 4 nm, respectively. Similarly, Fig. 4.2(b) presents R_{min} at the Ag thickness of 45 nm for the reflected responses at various Si layer thicknesses of 1, 2, 3, and 4 nm. The measured resonance angle and R_{min} (degree (normalized)) pairs are 74.07° (0.1727), 76.62° (0.1554), 80.19° (0.105), and 86.71° (0.0206) for the Si layer of 1, 2, 3, and 4 nm, respectively. Furthermore, Fig. 4.2(c) represents the reflected response for Ag thickness of 50 nm at various Si layer thicknesses of 1, 2, 3 and 4nm constituting the resonance angle and R_{min} (degree (normalized)) pairs at 74.16° (0.04132), 76.8° (0.031), 80.63° (0.0004938), and 87.19° (0.3989), respectively. Finally, Fig. 4.2(d) demonstrates the reflected response for Ag thickness of 55 nm with different Si layer thickness of 1, 2, 3, and 4 nm framing the resonance angle and R_{min} (degree (normalized)) pairs at 74.2° (0.0005422), 76.93° (0.0031), 80.63° (0.0266), and 86.89° (0.7107), respectively.

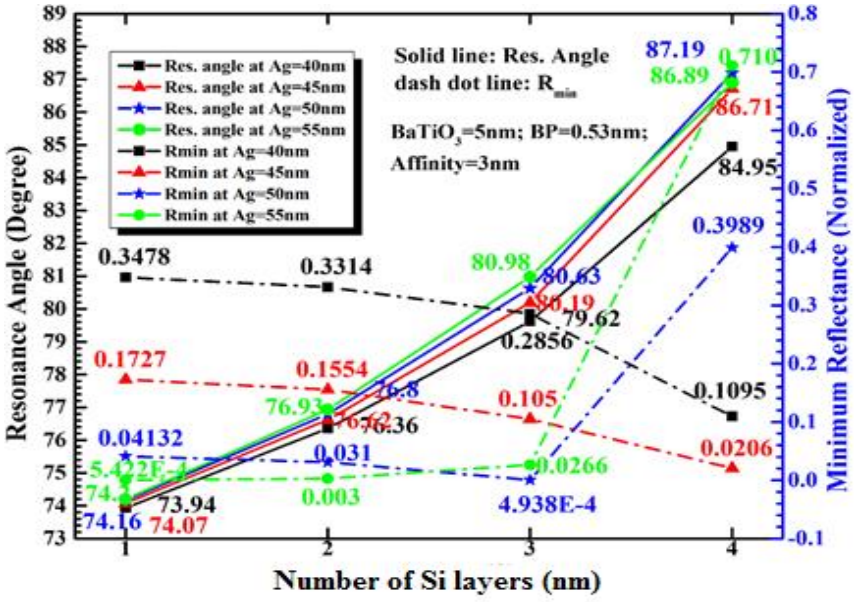

Fig. 4.3 SPR performance parameters at various Ag and Si thicknesses.

The variations in R_{min} indicate the spatial extension of SPs in a medium that depends on SPs' propagation length (PL) in the parallel direction. PL signifies a distance in propagation direction covered by SPs, decaying exponentially due to losses within the metal by the electron factor [153]. From the SPR phenomenon, the SPR resonance angle changes according to the thickness variation or layer's RI. From Fig. 4.3 and Table 4.2, it apparent that the minimal R_{min} is observed at an Ag thickness of 50nm and Si thickness of 3nm. On the contrary, at the Ag thickness of 50nm and Si thickness of 4nm, an increase in R_{min} is observed; therefore, this structure combination is inadvisable for further investigation of the proposed sensor.

Table 4.2 SPR performance parameters at various Ag and Si thicknesses

Si thickness (nm)		1	2	3	4
Ag=40nm	θ_{res}(°)	73.94	76.36	79.62	84.95
	R_{min}	0.3478	0.3314	0.2856	0.1095
Ag=45nm	θ_{res}(°)	74..07	76.62	80.19	86.71
	R_{min}	0.1727	0.1554	0.105	0.0206
Ag=50nm	θ_{res}(°)	74.16	76.8	80.63	87.19
	R_{min}	0.04132	0.031	$4.938E^{-4}$	0.3989
Ag=55nm	θ_{res}(°)	74.2	76.93	80.63	86.89
	R_{min}	$5.422E^{-4}$	0.0031	0.0266	0.7107

Table 4.3 Refractive index and optimal thickness parameters

Material Name	Refractive Index	Optimal Thickness	References
BK7	1.5151	-	[114]
Ag	0.056260+4.2776i	50nm	[143, 144]
Si	3.960	3nm	[145]
$BaTiO_3$	2.4042	5nm	[128, 146]
BP	3.5+0.01i	0.53nm	[138]
Affinity	1.437/1.49368/1.5265	3nm	[128, 131]
Sensing	1.33-1.34	-	[128]

In summary, structure configurations at Ag, Si (50nm, 4nm), and (55nm, 3nm), respectively, have been solicited to accomplish enhanced performance. Finally, this work has been considered an Ag thickness of 50nm, Si of 3nm as the best possible combination for adequate SPR performance, which has been utilized to study further. Table 4.3 has been summarized the refractive index and optimal thickness parameters of the various materials employed in the proposed SPR sensor.

4.3.2 Proposed SPR performance comparison

The reflectance curves of the proposed structure-3 are compared with the other structures (1 and 2) as shown in Fig. 4. In comparison process, the RIs for before and after adsorption have been considered as 1.33 and 1.34 for computing the performance parameters in terms of sensitivity, QF and FOM. The solid line signifies the response of before adsorption, whereas the dotted line indicates response of after adsorption. The red, blue and green colours are represented for structure-1, 2, and 3, respectively.

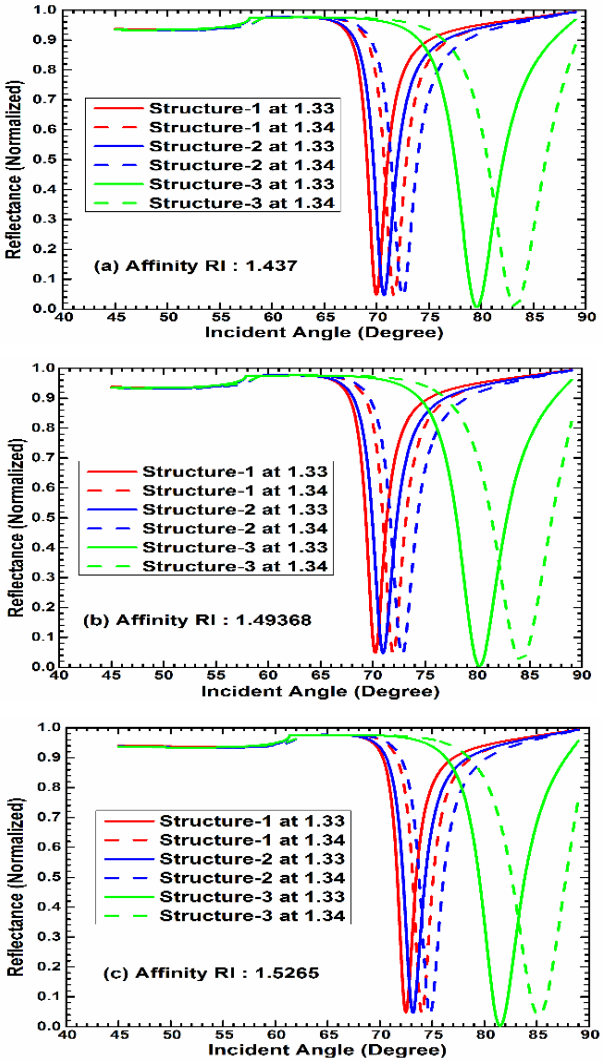

Fig. 4.4 Reflectance curves affinity RI of (a) 1.437 (b) 1.49368 (c) 1.5265.

The outlined performance parameters of structures for all bacterial attachments have been mentioned in Table 5. It is seen from Table 4.4 that structure-3 accomplishes an excellent sensitivity and had lower R_{min} performances compared to structures-1 and structures-2, as a consequence of the high penetration depth of SPW, high dielectric RIs for Si, and $BaTiO_3$, which can offer enhanced SPR performance. Moreover, the adsorption capability is increased by deposition of BP on surface of $BaTiO_3$, thereby restraining the environment and leading to low absorption loss [33]. In addition,

the proposed structure-3 provides an acceptable QF of 86.65 RIU^{-1} and FOM of 86.43 [131]. The graphical representation of sensitivity and QF performances are shown in Fig. 5 and FOM in Fig. 6 for three different affinity layers' RIs and structures. In summary, structure-3 has been shown better performance compared to other two structures-1 and 2.

Table 4.4 SPR performance parameters at ∇n of 0.01

RI of Bacteria (Affinity)			1437	1.49368	1.5265
Structure-1	R_{min}	1.33	0.0486	0.0484	0.0480
		1.34	0.0449	0.0441	0.0435
	S (°/RIU)		150	154	155
	QF (RIU^{-1})		86.21	86.03	85.64
	FOM		82.02	81.89	81.53
Structure-2	R_{min}	1.33	0.0474	0.0466	0.0463
		1.34	0.0425	0.0414	0.0407
	S (°/RIU)		159	163	168
	QF (RIU^{-1})		77.56	77.99	79.25
	FOM		73.92	74.34	75.57
Structure-3	R_{min}	1.33	0.0068	0.0039	0.0025
		1.34	0.0066	0.0210	0.0359
	S (°/RIU)		326.1	353	370
	QF (RIU^{-1})		81.32	84.45	86.65
	FOM		80.77	84.12	86.43

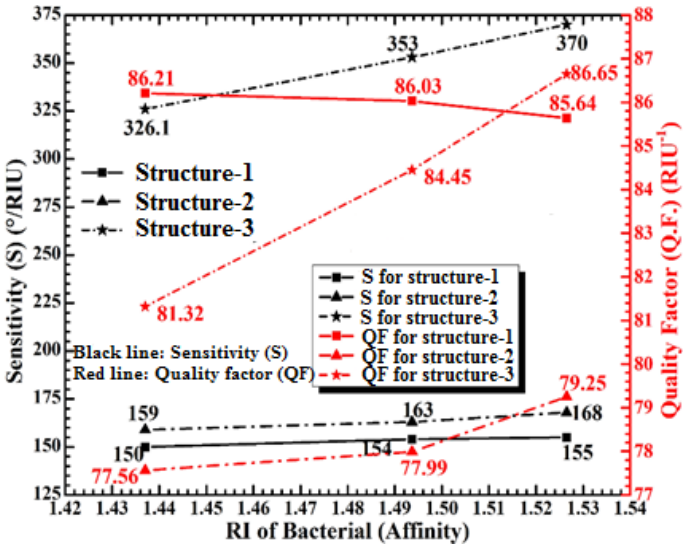

Fig. 4.5 S-QF representation vs. RI of affinity layer.

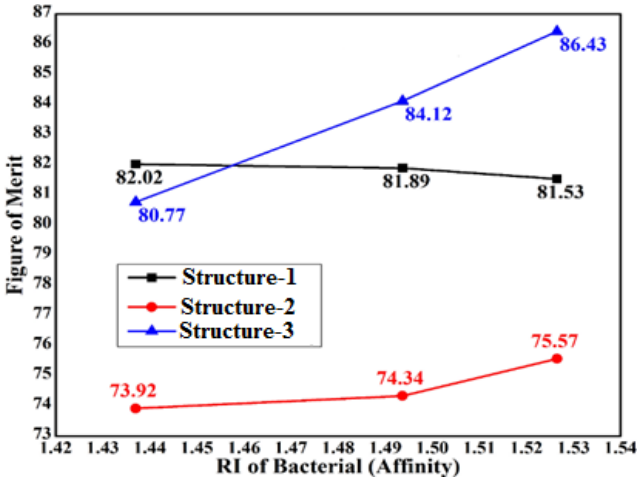

Fig. 4.6 FOM representation vs. RI of affinity layer.

4.3.3 Performance analysis of proposed SPR sensor with increasing the thickness of different layers

For analyzing the performance of the proposed structure-3 further, Fig. 4.7(a-c) present the reflectance intensity curves with respect to an angle for different affinity layers and RIs of the sensing layer, varying from 1.33 to 1.34 with an interval of 0.001. Fig. 4.7(a) depicts for the affinity RI of 1.437 (trifluoroethyl methacrylate), Fig. 4.7(b) signifies for the affinity RI of 1.49368 (toluene), and Fig. 4.7(c) signifies for the affinity RI of 1.5265 (nicotine). The measured resonance angles fora structure-3 at different different RIs are reported in Table 4.5.

In summary, this performance has been shown a substantial variation in resonance angles even when considering a minor variation in RI of the sensing layer which results in higher sensitivity for the proposed SPR biosensor. Therefore, it has been shown that structure-3 expressively affects the vibratory resonance angle for various Pseudomonas bacteria concentrations.

Though it has been shown the reflectance responses only with structure-3, the sensitivity performance has been computed for all structures in Table 4.1. Therefore, Table 4.6 has shown the sensitivity performance for all structures at different units of change in the RI (∇n). The sensing RI varies from 1.33 to 1.34, with an interval of 0.001. Fig. 4.8(a-c) show the graphical represents of all structures, respectively, whereas Fig. 8(a) plots the sensitivity performance for structure-1, Fig. 4.8(b) for structure-2, and Fig. 4.8(c) for structure-3. All acquired sensitivities of Fig. 4.8(a-c) at different unit change of RI (∇n) have been presented in Table 4.6; the outlined sensitivities of structure-1 vary from 130 -155°/RIU at all affinity RI of 1.437, 1.49368, and 1.5265. The reason for this sensitivity variation is because of the penetration depth (PD). The PD measures the SPs' interaction length in the transverse direction, which is sensitive due to the binding of biomolecules on the sensing surface to detect the sensing medium's RI shift [153]. The achieved sensitivities of structure-2 vary from 130-159°/RIU at

an affinity RI of 1.437, 155-180°/RIU at an affinity RI of 1.49368, 160-180°/RIU at an affinity RI of 1.5265, respectively. Finally, the succeeded sensitivities of structure-3 are varied from 285-326.1°/RIU at affinity RIs of 1.437, 270-353°/RIU at affinity RI of 1.49368, and 310-370°/RIU at affinity RI of 1.5265, respectively. Table 4.6 and Fig. 4.8(a-c) witness that structure-3 has been furnished a vast sensitivity compared to structure-1 and 2 under its hybrid properties, including the most abundant electropositive element, low dielectric losses, high RI, and high dielectric constant. Also, structure-3 administers high SPs, which are more sensitive due to the binding of bio-molecules on the sensing surface to detect the sensing medium's RI change.

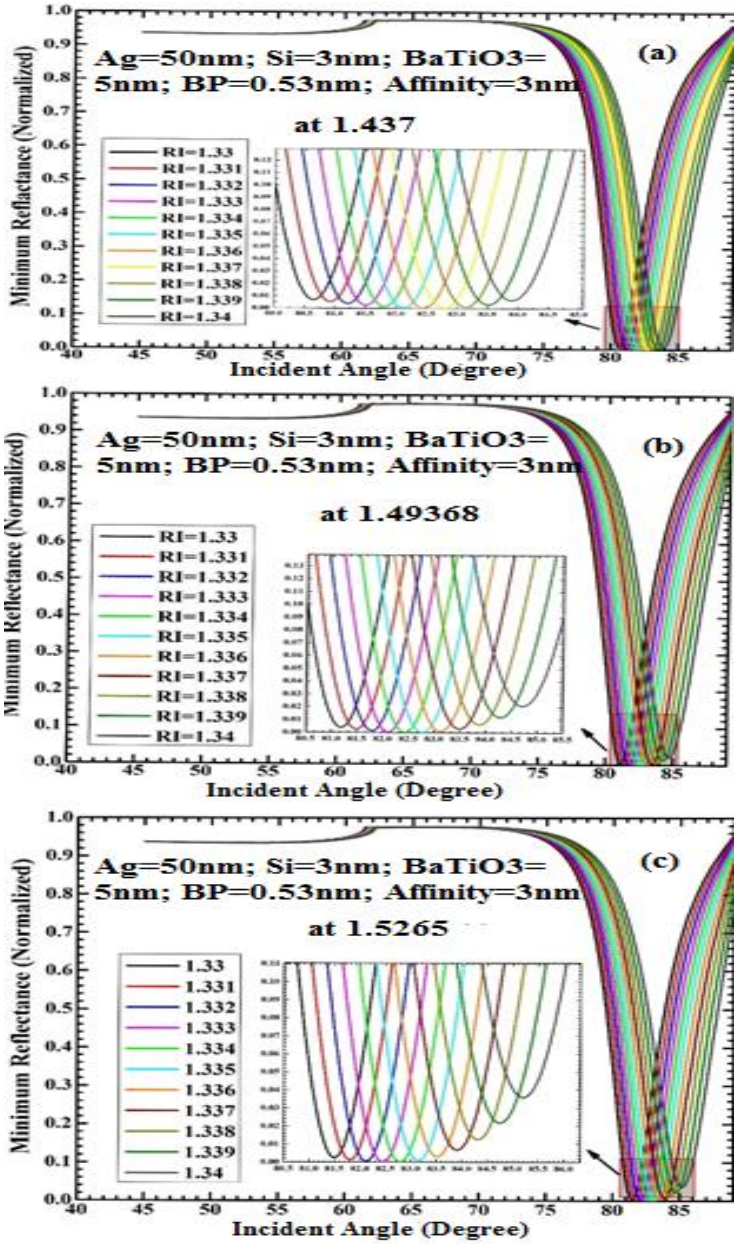

Fig. 4.7 Reflectance curve At affinity RI (a) of 1.437 (b) 1.49368 (c) 1.5265.

Table 4.5 Measuring θ_{res} vs sensing RIs for structure-3

RI of Bacteria (Affinity)		1.437	1.49368	1.5265
Resonance Angle (°) at different sensing RIs	1.33	80.63	81.2	81.51
	1.331	80.94	81.47	81.82
	1.332	81.2	81.78	82.13
	1.333	81.51	82.09	82.44
	1.334	81.82	82.44	82.79
	1.335	82.13	82.79	83.14
	1.336	82.44	83.14	83.54
	1.337	82.79	83.49	83.89
	1.338	83.14	83.89	84.33
	1.339	83.49	84.29	84.73
	1.34	83.89	84.73	85.21

Table 4.6 Measuring SPR Parameters of sensitivity for All Structures

		Structure-1			Structure-2			Structure-3		
RI of Bacteria		1.437	1.49368	1.5265	1.437	1.49368	1.5265	1.437	1.49368	1.5265
Sensitivity (S) (°/RIU) at respected ∇n	0.001	130	130	140	130	180	180	310	270	310
	0.002	155	155	155	155	155	180	285	290	310
	0.003	`146.67	`146.67	`146.67	`146.67	163.33	163.33	293.3	296.66	310
	0.004	142.5	155	145	155	165	165	297.5	310	320
	0.005	150	150	150	158	158	160	300	318	326
	0.006	146.67	146.67	146.67	155	161.67	161.67	301.7	323.33	338.33
	0.007	151.43	151.43	151.43	157.14	164.29	164.29	313.20	327.14	340
	0.008	148.75	153.75	155	155	160	166.25	313.75	336.25	352.5
	0.009	152.22	152.22	152.22	156.67	162.22	166.67	317.75	343.30	357.77
	0.01	150	154	155	159	163	168	326.1	353	370

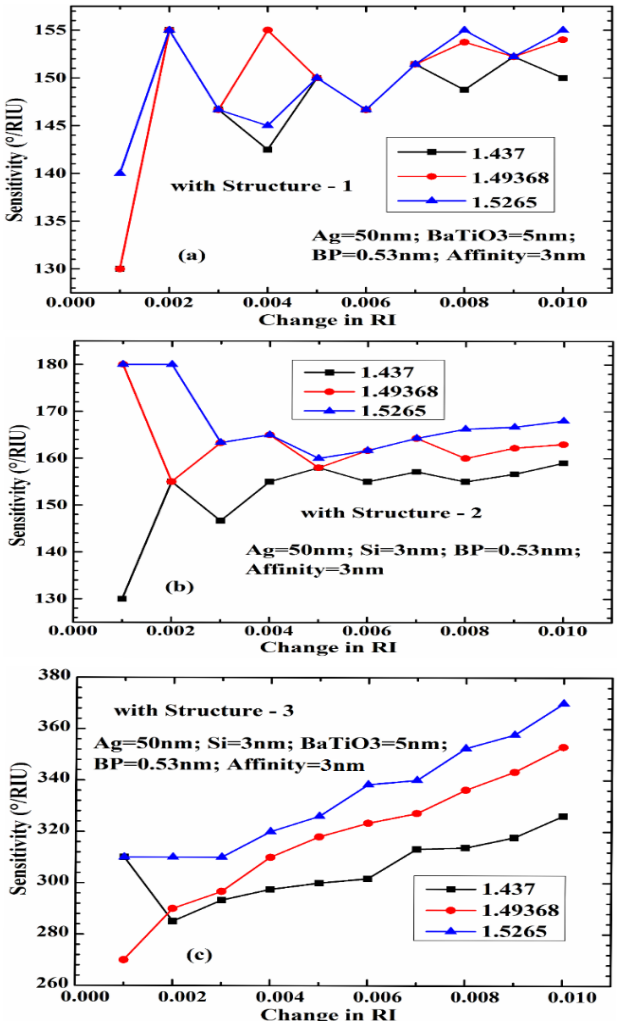

Fig. 4.8 Sensitivity with the change in sensing RI for different structures.

Moreover, the sensitivity performance of the proposed SPR sensor has been investigated by increasing the thickness of Si and $BaTiO_3$. Fig. 4.9 depicts the sensitivity performance with several Si layers at different affinity layer's RIs. The performance shows the highest S of 326.1°/RIU for affinity RI of 1.437, 353°/RIU for affinity RI of 1.49368 and 370°/RIU for affinity RI of 1.5265. Therefore, the performance outcome has been demonstrated the sensitivity of a novel SPR structure is proportional to the Si layers. Similarly, Fig. 4.10 presents the sensitivity measurement with different BaTiO3 thicknesses for all affinity layer's RIs. The performance exhibits the maximum sensitivity of 365°/RIU for affinity RI of 1.437, 353°/RIU affinity RI of 1.49368, and 370°/RIU for affinity RI of 1.5265. Fig. 4.10 is shown that the $BaTiO_3$ thickness of 5nm is optimal to achieve higher sensitivity and beyond 5nm, sensitivity decreases as a consequence of the low penetration depth of SPW that occurs due to the increased damping. Also, it depends on the top layer's (i.e., BP) adsorption property, which is both an absorber and an adsorber [33]. Finally, these inclusive performances have been demonstrated the sensitivity of the proposed SPR sensor increases with the thickness of Si and $BaTiO_3$ layers.

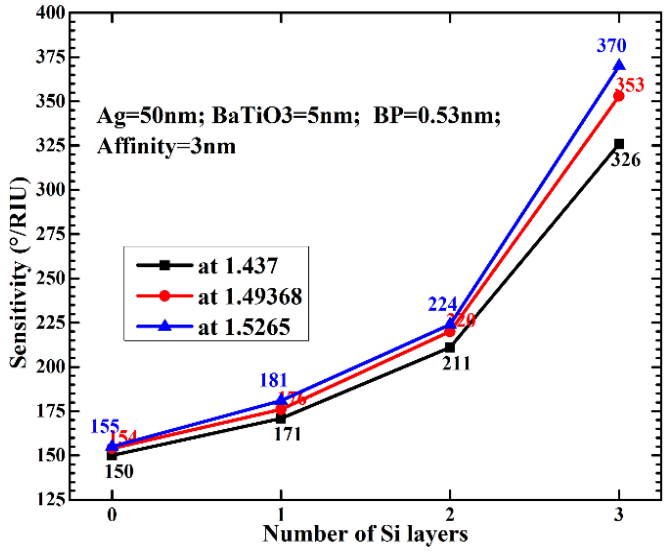

Fig. 4.9 Representing sensitivity for several the Si thickness from 1nm to 3 nm.

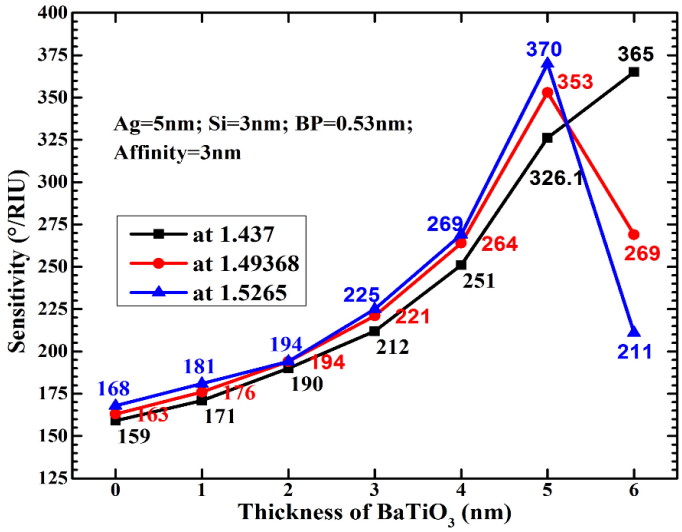

Fig. 4.10 Sensitivity measurement at various thicknesses of $BaTiO_3$ layers.

Sensitivity can be improved further for all structures by increasing the affinity layer's thickness, as shown in Fig. 4.11; it shows the sensitivity variation with increment of affinity layer's thickness for all structures at RIs of affinity layer. In each structure, the sensitivity is increasing with the thickness of the affinity. The maximum sensitivities for structure-1 are 150, 158, and 159°/RIU at the affinity RIs of 1.437, 1.49368, and 1.5265, respectively. Similarly, the sensitivity of 163, 168, 172°/RIU for the structure-2; and finally, the sensitivity of 366, 401, 410°/RIU for the structure-3 at the affinity RI of 1.437, 1.49368, 1.5265, respectively. In summary, Fig. 4.11 is demonstrated that at 5nm, the affinity layer's thickness is optimally exposed optimal to deliver higher sensitivity, and beyond this, sensitivity persists down. Finally, the performance manifests the effects of affinity thickness in the performance enhancement of the proposed SPR further for detecting the Pseudomonas bacteria.

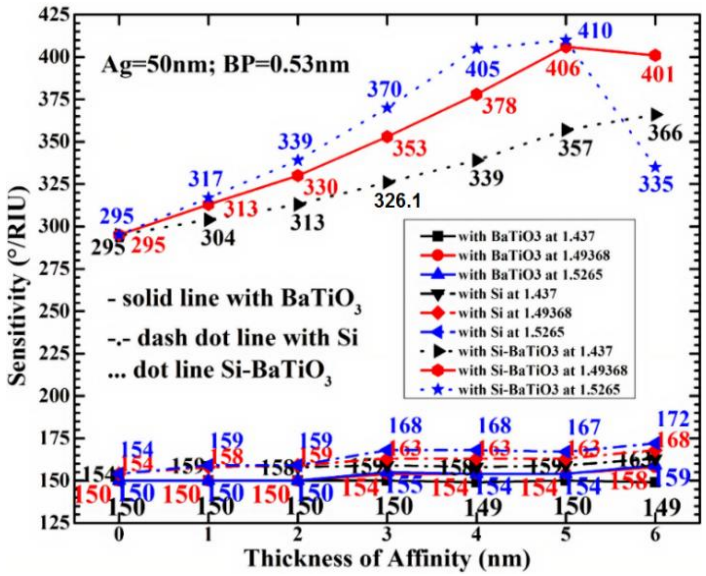

Fig. 4.11 Sensitivity measurement for different thickness of affinity layers.

4.3.4 Performance analysis: comparative study

In the conclusion of this performance analysis, Table 7 has been presented the performances of the proposed work (Si-$BaTiO_3$ oriented SPR) with existing works, and the same is graphically represented in Fig. 4.12; The proposed work is exhibited a higher sensitivity of 326.1, 353, 370°/RIU compared to all existing works at all RIs of affinity (bacteria) layer of 1.437, 1.49368, and 1.5265. In addition, this work has accomplished an agreeable QF for pseudomonas bacterial detection. Moreover, the FOM of 82.02, 84.12, and 86.43 has been computed by employing the proposed structure at all affinity layer's RIs, respectively.

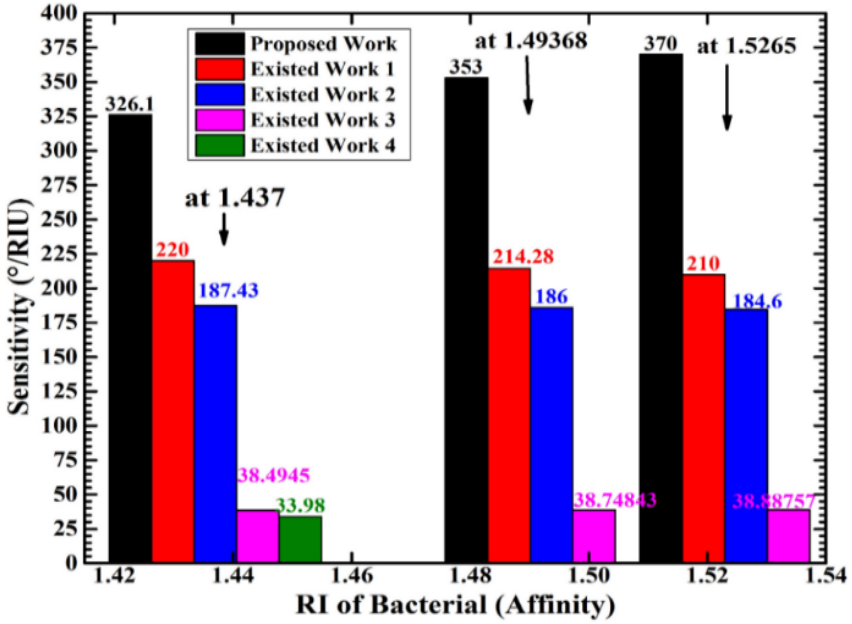

Fig. 4.12 Comparison of proposed sensitivity with existing works sensitivity.

Table 4.7 Comparative study on SPR Performance Analysis

Reference	Configuration	RI of affinity layer	S (°/RIU)	QF (RIU^{-1})	FOM
Present Work	BK7-Ag-Si-$BaTiO_3$-BP- Affinity-Sensing layer	1.437	326.1	86.21	82.02
		1.49368	353	86.03	84.12
		1.5265	370	86.65	86.43
Existed Work-1 [128]	BK7-Ag-$BaTiO_3$-Graphene- Affinity-Sensing layer	1.437	220	101.38	-
		1.49368	214.28	96.52	-
		1.5265	210	93.75	-
Existed Work-2 [131]	BK7-ZnO-Au-Graphene- Affinity	1.437	187.43	29.33	-
		1.49368	186	28.66	-
		1.5265	184.6	28.17	-
Existed Work-3 [132]	Chalcogenide Prism-Au-Graphene-Affinity- Sensing layer	1.437	38.4945	25.5144	-
		1.49368	38.74843	28.2838	-
		1.5265	38.88757	28.1793	-
Existed Work-4 [133]	SF10- Au-Graphene-Affinity- Sensing layer	1.437	33.98	2.7802	-

4.4 Conclusion

In this work, the proposed SPR sensor has been comprised of an Ag metal film, BP for the performance improvement, and affinity layer to protect the detection process, whereas Si used to produce a sharp resonance dip, and $BaTiO_3$ to render the high RI, low dielectric losses and high dielectric constant. Moreover, three bacterial attachments of Pseudomonas over the affinity layer have been constituted, such as toluene, nicotine, and trifluoroethyl methacrylate. The proposed Si-$BaTiO_3$ based SPR sensor structure has been exhibited the improved sensitivity of 370°/RIU, QF of 86.65RIU^{-1}, and FOM of 86.43 compared with the existing sensors. The highest performance parameters have been transpired for the RI alteration of 0.01 (i.e., 1.33-1.34) at the bacterial nicotine attachment (RI of 1.5265). Moreover, a higher sensitivity has been achieved by increasing the thickness of the affinity layer in this work. The literature has been demonstrated that sensitivity diminishes with the use of an alloy with Si combination in SPR structure. However, the proposed structure has been shown that improvement in the sensitivity using Si-$BaTiO_3$ alloy structure is because of its properties including most abundant electropositive element, low dielectric losses and high RI. Therefore, the presented SPR

structure furnishes an efficient SPR performance to detect the Pseudomonas bacteria and contributes towards a new platform in bio-sensing applications.

Chapter-5

Design and analysis of high-performance SPR Biosensor based on different novel hybrid structures

5.1 Introduction

The SPR can also be used in detection of the biological samples that have a very small range of refractive index. The sensor's high sensitivity performance with little variation in analyte (biomolecules) concentration demonstrates the sensor's better sensing capabilities, as it can detect extremely minute structural differences. This chapter presents two other SPR sensors employing thallium-based structure to validate the high-performance. In the first work, the numerical analysis of an SPR sensor is performed by considering the angular interrogation method and observed high sensitivity performance for thallium bromide-based structure. Being inspired by the impact of thallium bromide properties, in the second work, another novel SPR sensor is proposed employing thallium bromide-based structure to validate the high-performance. The SPR high-performance is validated by using the wavelength region method as well as by the FDTD solution tool.

5.2 Mathematical Equations

The transfer matrix method has been used for N-layer modelling to compute the proposed sensor's reflectivity (R_p) due to its efficiency as well as not required any approximations. Let assume that the k^{th} layer's thickness of d_k is considered along the Z-axis, ε_k signifies the dielectric constant of k^{th} layer. By employing the boundary conditions, the tangential field at $z = z_1 = 0$ are presented regarding of tangential field at $z = z_{z-1}$ as follows in Eq. (5.1):

$$\begin{bmatrix} A_1 \\ B_1 \end{bmatrix} = C_{ij} \begin{bmatrix} A_{N-1} \\ B_{N-1} \end{bmatrix} \tag{5.1}$$

Where, A_1 and B_1 symbolize the tangential components of electrical and magnetic fields, respectively, at the first layer boundary. $A_{N-1}$and B_{N-1} are corresponding fields for the n^{th} layer boundary. The C_{ij} signifies the properties matrix of the SPR sensor combined structure, and for P-polarized incident light, it can be given as Eq. (5.2).

$$C_{ij} = \left[\prod_{K=2}^{N-1} \begin{pmatrix} \cos\beta_k & -i\sin\beta_k / e_k \\ -ie_k \sin\beta_k & \cos\beta_k \end{pmatrix} \right]_{if} = \begin{bmatrix} C_{11} & C_{12} \\ C_{21} & C_{22} \end{bmatrix} \tag{5.2}$$

Where, Eq. (5.3) denotes a description of the transverse RI. Moreover, Eq. (5.4) measures the arbitrary stage constant β_k for the k^{th} layer, whereas Eq. (5.5) and (5.6) represent the wave impedance (z_k) and input angle (θ_k) for k^{th} layer. Here, λ is the wavelength of an incident light beam, n_p is the prism's RI, θ is the incident angle, μ_k is the permeability of the k^{th} layer [154]. Finally, Eq. (5.7) and (5.8) denote the mathematical expressions of Fresnel's R_p mode analysis for computing the R_p and reflection coefficient (r_p) of an incident light, respectively [154].

$$n_k = \begin{bmatrix} \mu_k \\ \varepsilon_k \end{bmatrix}^{1/2} \cos\theta_k = \sqrt{\frac{\varepsilon_k - (n_p \sin\theta)^2}{\varepsilon_k^2}} \tag{5.3}$$

$$\beta_k = \frac{2\pi}{\lambda} n_k \cos\theta_k (z_k - z_{k-1}) = \frac{2\pi}{\lambda} d_k \sqrt{\varepsilon_k - (n_p \sin\theta)^2} \tag{5.4}$$

$$z_k = \frac{k_x n_k \cos\theta_k}{(2\pi c/\lambda_{633})\varepsilon_k^2} \tag{5.5}$$

$$\theta_k = \left(\cos\sqrt{1-(n_{k-1}/n_k)(\sin\theta)^2} \right)^{-1} \tag{5.6}$$

$$R_p = |r_p|^2 \tag{5.7}$$

$$r_p = \frac{(C_{11} + C_{12} n_N) q_1 - (C_{21} + C_{22} n_N)}{(C_{11} + C_{12} n_N) q_1 + (C_{21} + C_{22} n_N)} \tag{5.8}$$

Sensitivity is defined as the ratio of change in SPR resonance angle ($\nabla\theta_{res}$) to change in the RI (∇n) and is a crucial factor for considering a better SPR sensor. The sensor's high sensitivity performance with little variation in analyte (biomolecules) concentration demonstrates the sensor's better sensing capabilities, as it can detect extremely minute structural differences. In addition, this study computes performances of QF, FOM, combined sensitivity factor (CSF) and DA, demonstrating the quality and accuracy of the sensor. The mathematical expressions to compute above-defined parameters have been shown in Eq. (5.9-5.13), whereas FWHM is the full width half maximum and R_{max} is the maximum reflectivity in the reflectance curve [155,156]. The performance of the quality factor and figure of merit manifest the product quality and noise impact in a sensor, respectively. Finally, the sensor's overall performance has been investigated with the combined sensitivity factor.

$$S = \nabla\theta_{res} / \nabla n \tag{5.9}$$

$$QF = S / FWHM \tag{5.10}$$

$$FOM = S \times (1 - R_{\min}) / FWHM \tag{5.11}$$

$$\text{Detection} - \text{Accuracy (DA)} = \frac{\nabla\theta_{res}}{\text{FWHM}} \tag{5.12}$$

$$CSF = S \times \left(R_{\max} - R_{\min}\right) / FWHM \tag{5.13}$$

5.3 A highly Performed SPR Biosensor Based on Bismuth Ferrite-Bromide materials-BP/Graphene Hybrid Structure

5.3.1 Design Consideration

The schematic structure of highly performed SPR biosensor based on the $BiFeO_3$-bromide materials-BP/graphene has been depicted in Fig. 5.1; the Kretschmann-based SPR biosensor consists of six layers, and all layers' RIs are operated at 633nm wavelength. The choice of a prism is also one of the crucial factors for SPR design in order to obtain optimal performance. Therefore, the performance for the three different RI prism-based sensors have been analysed first, and the considered prisms are Chalcogenide (2S2G), Schwerflint (SF10) and BoronKron (BK7), having the RI of 2.358 [157, 158], 1.723 [157] and 1.515 [159], respectively. Furthermore, the $BiFeO_3$ with RI of 2.9680 is coated over the Ag metal film with complex RI of 0.056266+4.27761i [159]. Similarly, several bromide materials, such as rubidium bromide (RbBr), potassium bromide (KBr), sodium bromide (NaBr), caesium bromide (CsBr), lithium bromide (LiBr), silver bromide (AgBr) and thallium bromide (TIBr), depositing on the $BiFeO_3$ with RI of 1.55, 1.5566, 1.6389, 1.6934, 1.7830, 2.2421 and 2.5728, respectively [160, 161].

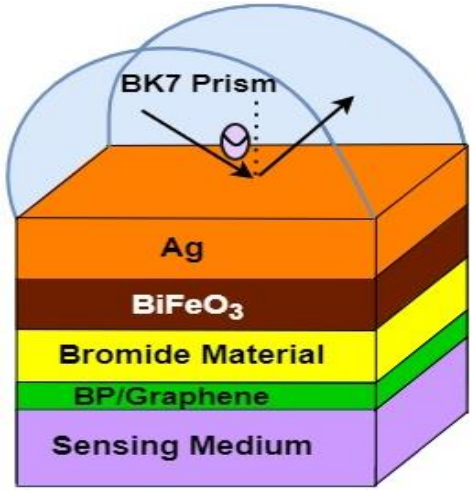

Fig. 5.1 Schematic structure design for Proposed SPR biosensor.

The thickness of $BiFeO_3$ and bromide material have been optimized by applying the iteration method, whereas Ag's constant thickness of 48nm gives better SPR performance [112]. Then, the BP/graphene is placed on the bromide materials and is utilized as BRE due to its high absorption capability, which leads to high SPR performance. The RI of BP and graphene are 3.5+0.01i and 3.0+1.149i with thicknesses of 0.53nm [157] and 0.34nm [138],

respectively. In the proposed SPR biosensor, the change of RI before and after the adsorption of biomolecules is assumed to be 0.005 [128, 162]. This proposed structure observes the performance for minute variation in the adsorption molecules. The list of optimized designed parameters for the proposed SPR structure has been presented in Table 5.1.

Table 5.1. List of Designed Parameters of Proposed SPR Structure

Layer	Refractive Index	Thickness
2S2G/SF10/BK7-prism	2.358/1.723/1.515	-
Silver (Ag)	0.056266+4.27761i	48nm
$BaTiO_3$	2.9680	5nm
RbBr/KBr/NaBr/CsBr/LiBr /AgBr/TIBr	1.55/15566/1.6389/1.6934/1.7830/ 2.2421/2.5728	5nm
BP/graphene	3.5+0.01i/ 3.0+1.149i	0.53nm/0.34nm
Sensing medium	1.33-1.335	-

5.3.2 Simulation Results

Initially, the performance shows the importance of prism's RI that can affect the sensitivity for the proposed SPR biosensor. Here, three prism RIs have been considered that are variable, and then the response of change in resonance angle ($\nabla\theta_{res}$) and sensitivity are presented in Fig. 5.2(a). The results show that both response curves decrease with an increase in the prism's RIs. Therefore, it can be demonstrated that a relatively low RI can accomplish a relatively high sensitivity, and the reason can be adduced by employing Snell's law with a simplified structure, as shown in Fig. 5.2(b). Here, an incident light passes through a prism (n_p) into another dielectric medium (n_2), whereas the incident and refraction angles are θ_i and θ_2, respectively. The n_{2S2G}, n_{SF10} and n_{BK7} signify the RI of three different prisms, and their relationship is $n_{2S2G} > n_{SF10} > n_{BK7}$. From Snell's law, it shows the mathematical expression: ($n_p \sin\theta_i = n_2 \sin\theta_2$). Now, assuming that θ_2 is constant and n_2 is varying to ($n_2 + \nabla n$). If the changes occur in the incident angle of three different prisms, then it should meet the relation of $\nabla\theta_{2S2G} > \nabla\theta_{SF10} > \nabla\theta_{BK7}$ due to relation of $n_{2S2G} > n_{SF10} > n_{BK7}$. The lower RI of prism can have high resonance angle shift according to the changes in RI (∇n) because the reflection angle equals the incident angle. Hence, higher SPR performance can be achieved by employing lower RI of the prism.

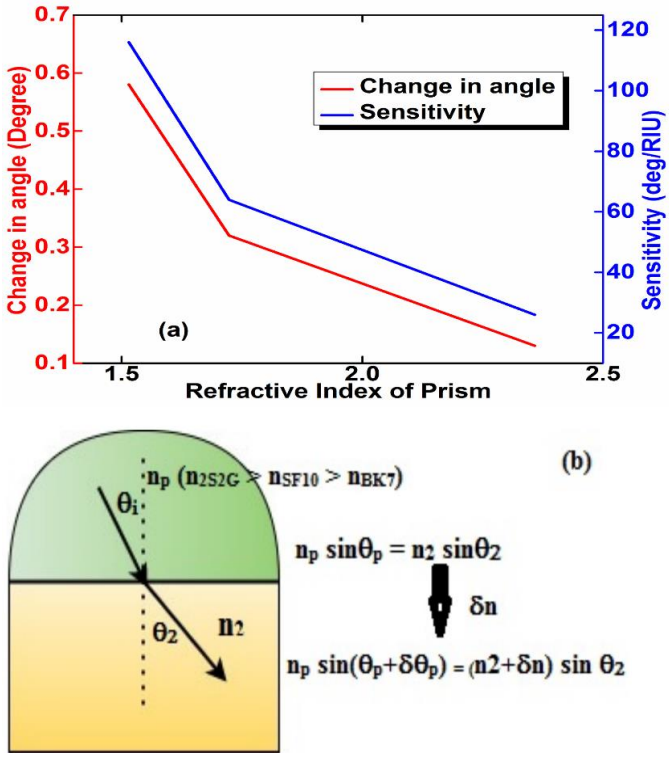

Fig. 5.2 (a) SPR parameters vs RI of prism (b) Basic structure to analyze Snell's law.

This work considered the 2S2G, SF10, and BK7 prisms for optimizing the better SPR performance. Their reflectance responses are plotted in Fig. 5.3 with Ag thickness of 48nm, whereas Fig. (5.3a), Fig. (5.3b) and Fig. (5.3c) are represented for 2S2G, SF10 and BK7 prisms-based structures, respectively. The solid line signifies the before adsorption (sensing RI of 1.330), and the dashed line indicates after adsorption (sensing RI of 1.335) of the biomolecules. The measured parameters of θ_{res}, $\nabla\,\theta_{res}$, and sensitivity for Fig. 5.3 have been reported in Table 5.2. The summary of the results have been observed that $\nabla\theta_{res}$ are 0.13, 0.32 and 0.58°, and sensitivities are 26, 64 and 116deg/RIU (refractive index unit) for 2S2G, SF10 and BK7 prisms, respectively. Therefore, better sensitivity achieves by employing BK7 due to a more negligible Kerr effect and low absorption loss [138, 155], and the same prism is used as the coupling prism in the proposed SPR structure to enhance the performance.

Furthermore, the optimized thickness of $BiFeO_3$ and another dielectric layer are also essential factors that can affect the proposed SPR performance. The authors in [128] optimized the layer thickness from the performance of minimum reflectance (R_{min}) by applying the iteration process of reflection theory's Fressnel model. Therefore, to obtain optimized thickness of dielectric layers, Fig. 5.4 depicts the R_{min} performance with respect to the $BiFeO_3$ thickness at different TIBr thicknesses. In this event, as a dielectric layer, TIBr has been used because it

has highest RI of all, which may offer high absorption loss and damping effect in the SPR response.

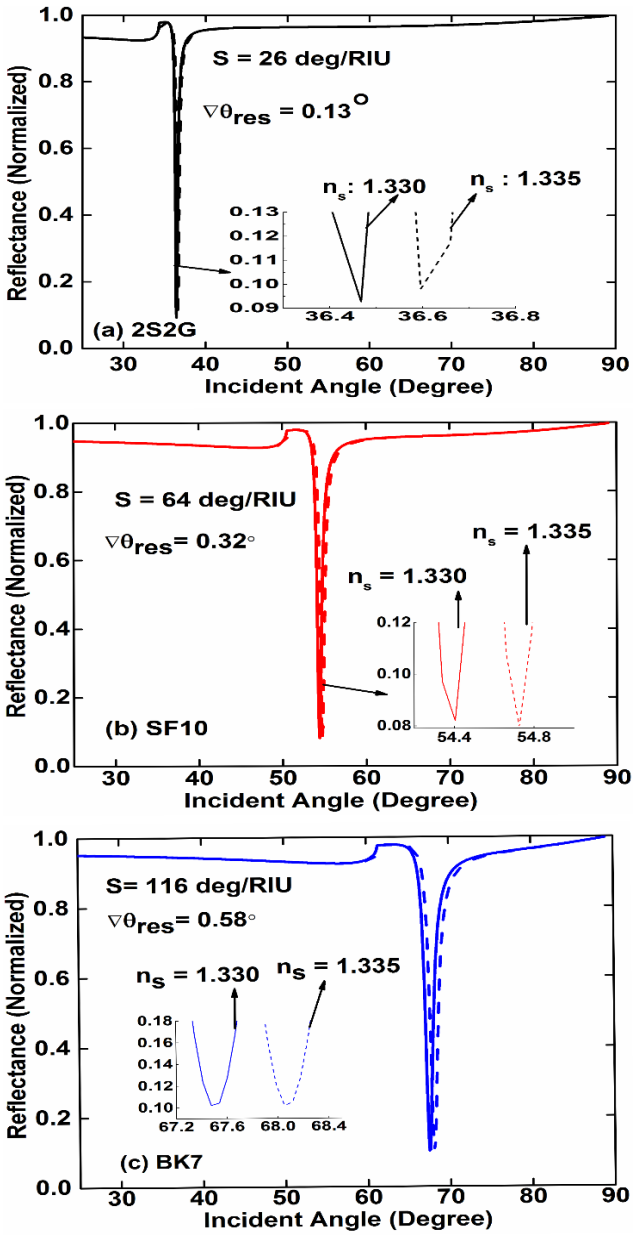

Fig. 5.3 Reflectance responses (a) 2S2G (b) SF10 (c) BK7.

Table 5.2. Measured SPR Parameters for Fig.3

Utilized Prism	Resonance angle (θ_{res}) at different sensing RIs (°)		Change in θ_{res} at change in RI of 0.005 (°)	Sensitivity (°/RIU)
	1.330	1.335		
2S2G	36.47	36.6	0.13	116
SF10	54.41	54.73	0.32	64
BK7	67.47	68.05	0.58	116

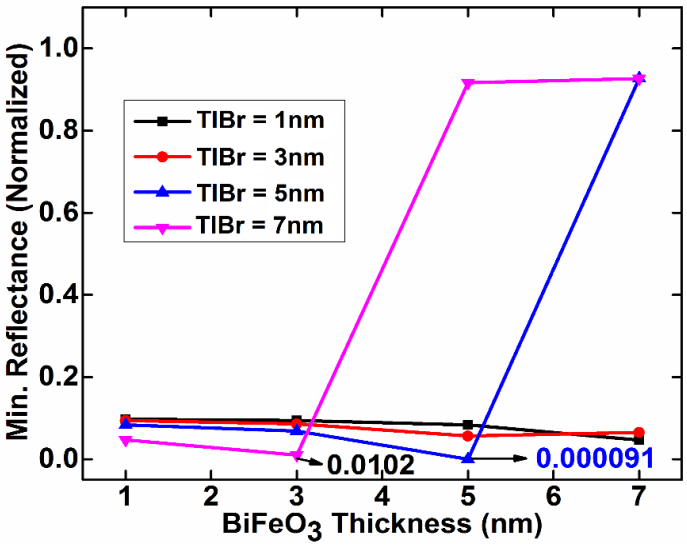

Fig. 5.4 Measurement of R_{min} vs thicknesses of $BiFeO_3$ and TIBr.

From Fig. 5.4, it can be clearly witnessed that the less R_{min}, which is essential for optimal performance [137], has been occurred at the $BiFeO_3$ and TIBr thicknesses of 5nm and 5nm, respectively. The less R_{min} is transpired due to the spatial extension of SPs in a medium that depends on SP's propagation length (PL) in the parallel direction [138]. The computed value of less R_{min} at the optimal thicknesses (i.e., $BiFeO_3$ of 5nm, TIBr of 5nm) is 0.000091; therefore, this study has been concluded that the thicknesses of $BiFeO_3$ of 5nm and TIBr of 5nm are used for further analysis of the proposed SPR structure.

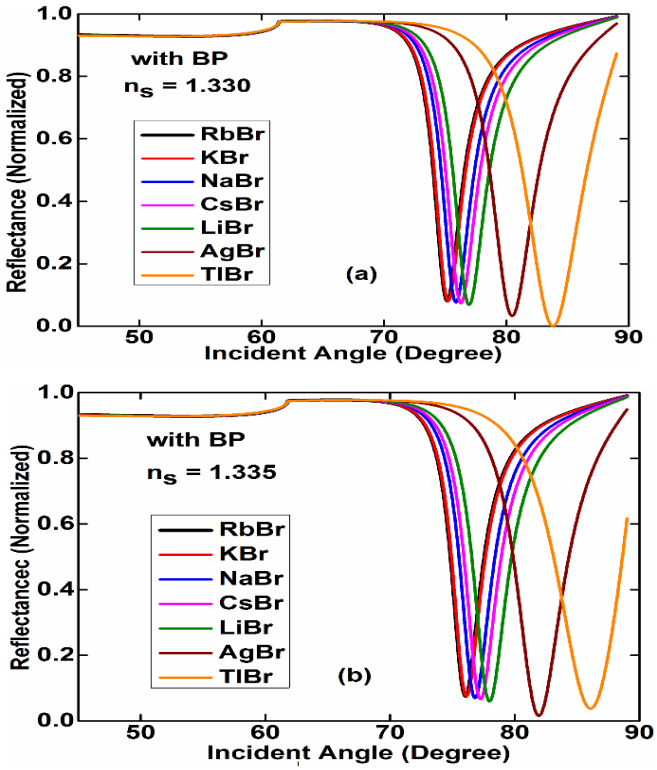

Fig. 5.5 SPR responses vs angle with BP at RI of sensing of (a) 1.330 (b) 1.335.

Furthermore, Fig. 5.5 presents the reflectance response in terms of the incidence angle for different bromide dielectric materials in order to observe the finest bromide material in the proposed SPR structure. In Fig. 5.5, the responses are plotted for BP-based (Bismuth Ferrite-bromide materials-BP) at sensing RI of 1.330 (Fig. 5.5a) and 1.335 (Fig. 5.5b). Similarly, in Fig. 5.5, the responses are plotted for graphene-based (Bismuth Ferrite-bromide materials-graphene) at sensing RI of 1.330 (Fig. 5.5a) and 1.335 (Fig. 5.6b). Asymmetry in the reflectance curves has been observed in the plots due to the high changes in RI of the sensing medium that can affect the FWHM measurement [163]. The computation of R_{min} performance for Fig. 5 and 6 has been reported in Table 5.3. It is noticed that the accomplished performances are almost equal for each bromide material, while the least R_{min} is obtained for Bismuth Ferrite-TIBr-BP composite structure at the sensing RI of 1.330, whereas it has been increased in the remaining cases. The reason for less R_{min} is that the spatial extension of SPs in a medium [138]; and high R_{min} transpires due to the attenuation or damping of electromagnetic wave's effect and RI of dielectric materials i.e., bromide materials [38].

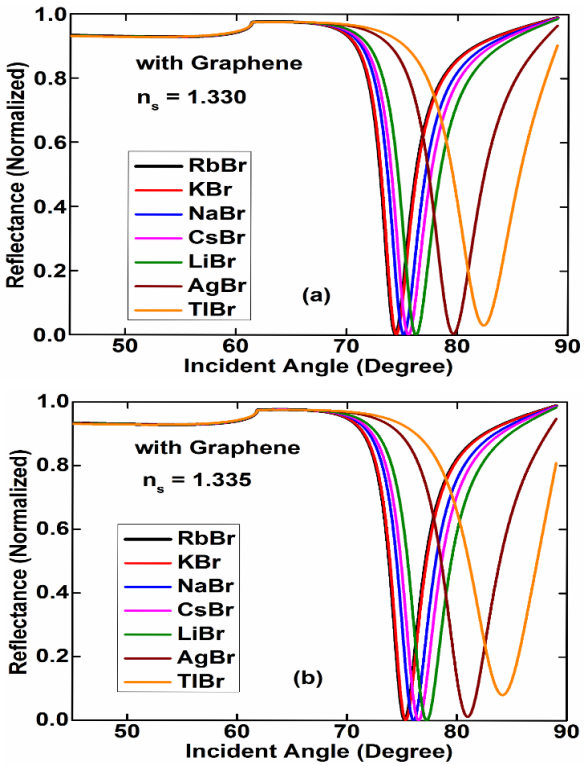

Fig. 5.6 SPR responses vs angle with graphene at RI of sensing of (a) 1.330 (b) 1.335..

Finally, Table 5.3 explores that less R_{min} has been transpired for the TIBr-BP-based structure. In the remaining cases, the graphene-based structure has been accomplished less R_{min} performance than BP combined structure. Moreover, the SPR performance parameters, such as sensitivity, QF, FOM and DA for Fig. (5.5) and (5.6) are computed by applying Eq.

(5.9-5.12). The computed SPR parameters are mentioned in Table 5.4, whereas Fig. 5.7(a-d) show their graphical representations. Fig. (5.7a) demonstrates that the $\nabla\theta_{res}$ and sensitivity are directly proportional to the RI of bromide materials due to high RI and less damping that offers the high penetration depth of the evanescent field of the SPW. Also, it has been enhanced due to the high absorption capacity of the top layer, i.e., BP and graphene [142]. The highest achieved sensitivities are 468 and 354°/RIU for BP and graphene-based structures, respectively. The summary of the results havae been demonstrated the proposed SPR biosensor with $BiFeO_3$-bromide-BP-based structure can accomplish better sensitivity performance than the $BiFeO_3$-bromide-graphene-based structure. Therefore, from Fig. (5.7a), it has been cleared that the high RI of bromide materials can be chosen for better SPR performance in terms of $\nabla\theta_{res}$ and sensitivity, using the hybrid structure of $BiFeO_3$ and 2D material, i.e., BP or graphene. Similarly, Fig. (5.7b), (5.7c), and (5.7d) have been shown the performance of QF, FOM and DA, reporting that they have been an almost equal increment of FWHM, resonance angle shift up to the bromide RI of 1.7830 (< RI of LiBr), beyond that it increases their performance. From Eq. (5.10-5.12), it is clear that the QF, FOM, and DA are inversely proportional to the FWHM. Though FWHM is increasing concerning the RI of bromide materials due to high damping, the performance of QF, FOM, and DA is also increasing because it offers a high resonance angle shift. It signifies that high absorption molecules and low loss can be generated at high RI of bromide materials with the hybrid structure of $BiFeO_3$ and BP/graphene. The maximum achieved QFs' are 87.80 and 60.00RIU^{-1}; FOMs' are 87.79 and 58.18; DAs' are 0.44 and 0.30 for BP-based and graphene-based structures, respectively.

Table 5.3. Measurement of R_{min} with BP and Graphene at Different Sensing RIs

Name of Bromide Material	Minimum Reflectance with BP		Minimum Reflectance with Graphene	
	n_s = 1.330	n_s = 1.335	n_s = 1.330	n_s = 1.335
RbBr	0.0817	0.0766	0.0029	0.0020
KBr	0.0814	0.0760	0.0028	0.0019
NaBr	0.0770	0.0704	0.0017	0.00097
CsBr	0.0738	0.0663	0.0011	0.00046
LiBr	0.0680	0.0591	0.00054	0.00012
AgBr	0.0286	0.0112	0.0040	0.0116
TIBr	0.00009	0.0773	0.0303	0.0803

Table 5.4. Measurements of SPR Parameters with BP and Graphene

Name of Bromide Material	S (°/RIU)		QA (RIU^{-1})		FOM		DA	
	BP	Graphene	BP	Graphene	BP	Graphene	BP	Graphene
RbBr	176	166	70.68	52.87	64.91	52.72	0.35	0.26
KBr	176	168	70.40	53.17	64.97	53.02	0.35	0.27
NaBr	186	176	69.66	52.38	64.60	52.29	0.35	0.26
CsBr	194	186	69.78	53.14	64.63	53.08	0.35	0.27
LiBr	202	194	68.24	52.15	63.60	52.12	0.34	0.26
AgBr	308	264	75.31	53.99	73.16	53.77	0.38	0.27
TlBr	468	354	87.80	60.00	87.79	58.18	0.44	0.30

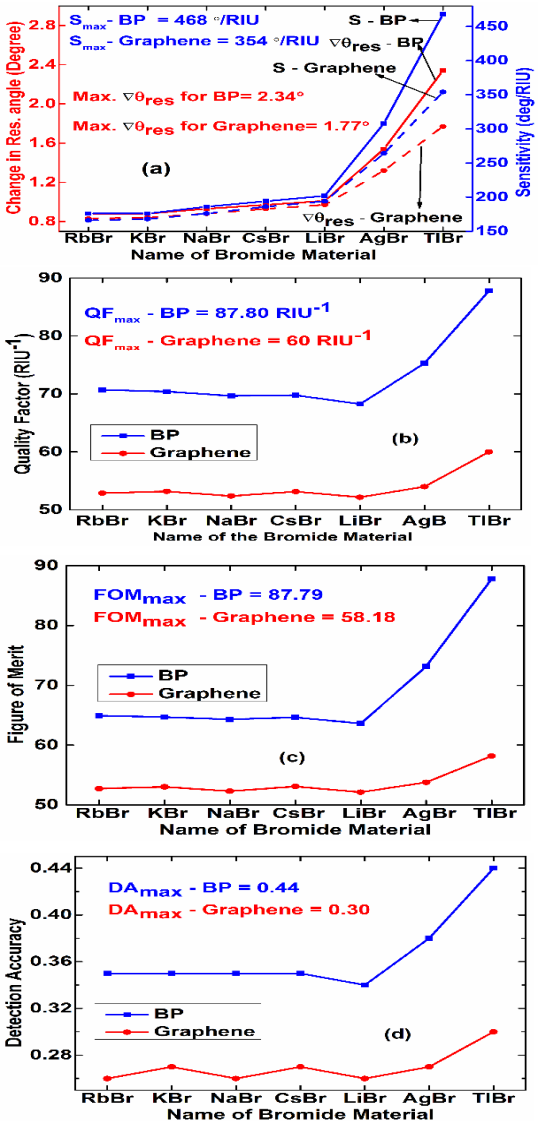

Fig. 5.7 (a) Change in resonance angle and Sensitivity (b) QF (c) FOM (d) DA.

For a better understanding of the impact of $\nabla\theta_{res}$ using the proposed SPR sensor, Fig. 5.8 presents the variations in $\nabla\theta_{res}$ concerning the bromide material's RI at different amount of ∇n in the sensing medium, whereas Fig. 5.8a and Fig. 5.8b depict for BP and graphene-based structures. The results have been observed the $\nabla\theta_{res}$ is directly proportional to the ∇n amounts of the sensing medium. Moreover, the $\nabla\theta_{res}$ amount is slightly increased until the RI of 1.7830 (<RI of LiBr); beyond that the $\nabla\theta_{res}$ amount is highly increased, which is leading to higher sensitivity due to high absorption capability. Also, the BP-based structure has been accomplished a higher $\nabla\theta_{res}$ amount than the graphene-based structure at each ∇n amount of the sensing medium. This investigation has been further demonstrated the stability and rationality of the proposed SPR biosensor.

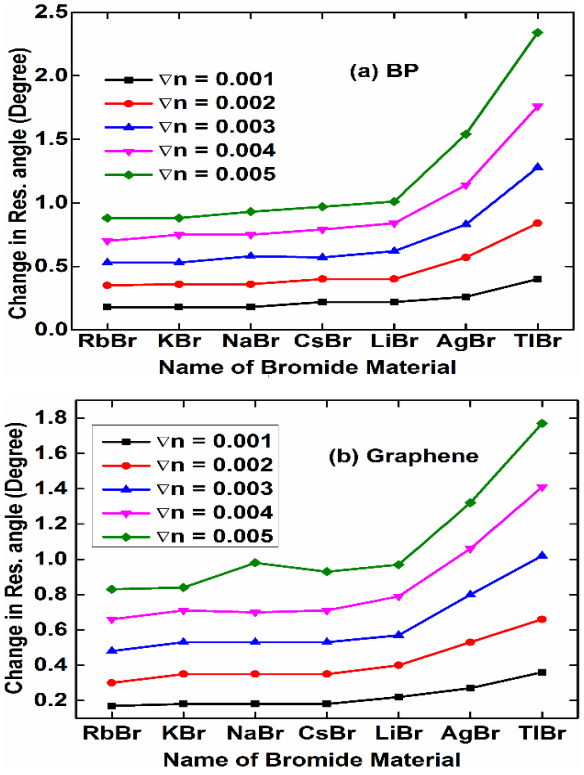

Fig. 5.8 Change in resonance angle Vs RI with (a) BP and (b) Graphene.

Finally, the performance of the proposed structure has been compared with the previously reported structures done by other researchers, as tabulated in Table 5.5. The highest performance parameters for the proposed SPR structure are sensitivity of 468 deg/RIU, QF of 87.80RIU^{-1} and FOM of 87.79, and DA of 0.44. This study has been clearly exhibited exceptional performance compared to the other latest work for highly performed SPR biosensors. The sensitivity performance of the proposed sensor is comparatively less than the sensitivity of ref. [164]. However, it has been shown better minimum reflectance performance compared to ref. [164] due to the high SPR ratio of Ag as desired. Moreover, the desired SPR

parameters, such as QF, FOM and DA, are measured to observe the performance of the proposed sensor and achieved noble values. In addition, this structure is used a simpler structure compared to the structure of ref. [164] in terms of design complexity and achieved better performance. Therefore, the proposed SPR sensor can accomplish high-performance in the biomedical and biomolecular applications.

Table 5.5 Performance Comparison of Proposed and Existing Work

Ref. No.	Structure of the SPR sensor	S(deg/RIU)	QF	FOM	DA
[165]	BK7/Ag/WS_2/Ni/graphene	243.31	-	34.03	-
[164]	BK7/Cu/Ni	480	-	-	-
[164]	BK7/Cu/Ni/WS_2	426	-	-	-
[166]	SF10/Ni/BlueP/WS_2	270	-	-	-
[167]	BK7/Ag/$BaTiO_2$/Ag/graphene	280	-	-	-
[168]	BK7/Cu/Ni/BP/MXene	304.47	-	-	-
[169]	FK51A/Ag/$BaTiO_2$/blue P/MoS_2	347.82	60.52	-	-
[33]	Prism/Au/BP	180	-	-	0.29
[155]	Prism/Air/MoS_2/Al/MoS_2/graphene	190.83	-	-	-
[170]	Prism/Au/MoS_2/Au/graphene	182	-	-	-
[171]	Prism/Ag/$PtSe_2$	162	-	14.93	0.1493
[171]	Prism/Ag/$PtSe_2$	165	-	14.12	0.1412
[172]	Prism/Ag/$PtSe_2$/WS_2	194	34.22	17.64	0.091
[172]	Prism/Ag/$PtSe_2$/WS_2	187	29.39	15.72	0.084
Presented work	Prism/Ag/$BiFeO_3$/TIBr/BP	468	87.80	87.79	0.44
	PrismAg/$BiFeO_3$/TIBr/Graphene	354	60	58.18	0.30

5.4 Performance Enhancement of a Novel Surface Plasmon Resonance Biosensor using Thallium Bromide

5.4.1 Structure Design

The schematic structure of the proposed SPR sensor for bio-sensing applications (i.e., ssDNA) has been presented in Fig. 5.9. The Kretschmann SPR biosensor consists of six layers, and all layers' RI are operated at 633nm wavelength. This structure design has been utilized the BK7 prism as the first layer (n1) to offers the minimum Kerr factor, having the RI of 1.515 [115]. The second layer (n2) is composed of Ag, as coated over the prism base with a complex

RI of 0.056266+4.27761i. In addition, the dielectric layers, such as AlAs and TIBr, are deposited on Ag for protection against oxidation and enhanced sensor performance. Therefore, the third and fourth are comprised of AlAs and TIBr, as coated over the Ag with RI of 3.1099 and 2.5728, respectively. The Ag and TIBr's thickness is optimized by applying the iteration method, where the constant thickness of AlAs is 5nm. The fifth layer (n5) is BP deposited over the TIBr with an RI of 3.5+0.01i and a thickness of 0.53nm [115]. Finally, the sixth layer (n6) is a sensing medium for the water biomolecules adsorption, and RI varies from 1.33 to 1.332. This proposed structure observes the performance for minute variation in the adsorption molecules. To compare the proposed structure's performance, it is considered three other dissimilar SPR structures with the above-defined layers.

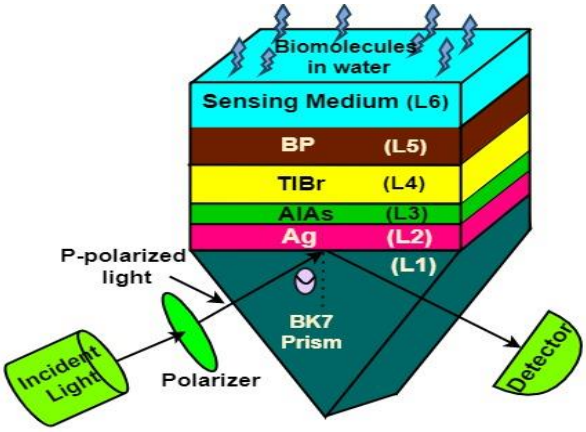

Fig. 5.9. Proposed SPR biosensor structure ("L" denotes the Layer).

5.4.2 Results and Discussion

The proposed SPR sensor requires the optimized thickness of Ag and TIBr to analyze the optimized performance. This thickness optimization is obtained from the performance of R_{min} by the applying iteration process. The reason for it is that many other researchers have been optimized their proposed SPR structures by applying the iteration method [155, 169]. They have been optimized their layer structures based on the R_{min} performance. Fig 5.10(a-c) present the reflectance responses for different thicknesses of Ag (i.e., 40-50nm with an interval of 5nm) and TIBr (i.e., 1-7nm with an interval of 2nm), whereas the residual layers have constant thicknesses, i.e., AlAs of 5nm, and BP of 0.53nm. Fig 5.10(a) shows the reflectance responses in terms of an angle for the different TIBr thicknesses, whereas Ag is remained at 40nm thickness. The obtained results are R_{min} of 0.3418, 0.3071, 0.1720, and 0.7808 at resonances angles of 75.05, 78.35, 83.52, and 86.38° for assigned TIBr thicknesses, respectively. The variations in R_{min} is occurred due to the spatial extension of SPs in a medium that depends on SP's propagation length (PL) in the parallel direction. The PL is a distance in

propagation direction covered by SPs, decaying exponentially due to losses within the metal by the electron factor [114].

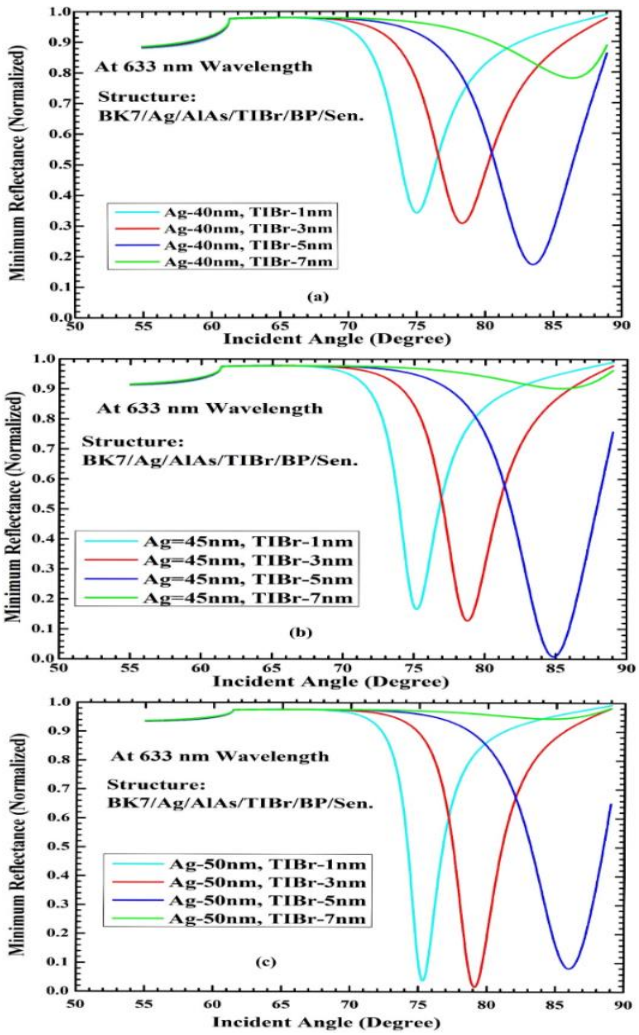

Fig 5.10. Ag and TIBr Optimization at Ag thickness of (a) 40nm (b) 45nm (c) 50nm.

Similarly, Fig 5.10(b) displays the reflectance responses at a constant thickness of Ag is 45nm. The attained R_{min} values are 0.1657, 0.1277, 0.0081, and 0.9023 at resonance angles of 75.22, 78.79, 84.85 and 85.46° for allotted TIBr thicknesses, respectively. Finally, Fig 5.10(c) represents the reflectance responses at a constant thickness of Ag is 50nm. The acquired R_{min} values are 0.0383, 0.0166 and 0.0803 at resonance angles of 75.32, 79.13 and 86.01° for the TIBr thicknesses of 1nm, 3nm and 5nm, respectively. At thickness of 7nm, the resonance dip is distressed by the limitation resonance condition (i.e., the total energy of SPs transfer to the detector) and loss of the metal electron factor. The outlined measurements of R_{min} and resonance angles for fig. 5.10(a-c) are represented in Table 5.6, which is demonstrated that less R_{min} is generated at the Ag and TIBr thickness of 45nm and 5nm, respectively. Hence, it has been concluded the optimized thickness values of Ag and TIBr are utilizing in the proposed

SPR sensor for further performance analysis. After optimizing layers thicknesses, the parameter list and different structures for the proposed work have been presented in Table 7 and 8 successively, which are utilized for further investigation of this study.

Table 5.6 Measured Parameters for different thicknesses of Ag and TIBr

Ag Thickness	TIBr Thickness	Minimum Reflectance	Resonance angle (°)
40	1	0.3418	75.05
40	3	0.3071	78.35
40	5	0.1720	83.52
40	7	0.7808	86.38
45	1	0.1657	75.22
45	3	0.1277	78.79
45	5	0.0081	84.85
45	7	0.9023	85.46
50	1	0.0383	75.32
50	3	0.0166	79.13
50	5	0.0803	86.01
50	7	-	-

Table 5.7 Parameter List for Designed Proposed SPR Structure

Layer	Refractive Index (RI)	Thickness
BK7-prism	1.515	-
Silver (Ag)	0.056266+4.27761i	45nm
Aluminum arsenide (AlAs)	3.1099	5nm
Thallium Bromide (TIBr)	2.5728	5nm
Black Phosphorus (BP)	3.5+0.01i	0.53nm
Sensing medium	1.33-1.332	-

Table 5.8 List of Considered Structure with defined Layers

Structure No.	SPR Biosensor Name	Combination
I	Conv.	BK7-Ag- Sen.
II	BP-based	BK7-Ag- BP-Sen.
III	AlAs-based	BK7-Ag-AlAs-BP-Sen.
IV	Proposed	BK7-Ag-AlAs-TIBr-BP-Sen.

The reflectance curve of the proposed structure-4 has been compared with the other structures (1, 2, and 3), as shown in Fig. 5.11. In the comparison process, this study has been considered the RIs, before and after adsorption as 1.33 and 1.332, indicating the RI's minute variation for computing the performance parameters in terms of sensitivity, QF, FOM, and CSF. The solid and dotted SPR reflectance curves signify before and after adsorption, and cyan, blue, red and green colours represent for structures-I, II, III, and IV, respectively. The outlined performance measurements of Fig. 5.11 have been mentioned in Table 5.9, which can demonstrate that FWHM and change in resonance angle are increased from structure-I to IV. The SPR parameters of sensitivity, QF, FOM, and CSF are measured using Eq. (5.9-5.11 and 5.13). The SPR sensor has a maximum sensitivity of 105°/RIU for structure-I, 120°/RIU for structure-II, 155°/RIU for structure-III, and 475°/RIU for structure-IV. The sensitivity of the structure-II (i.e., BP-based SPR) is greater than the structure-I (i.e., conventional SPR) due to its exceptional properties, including low dielectric losses, high RI, high molar mass of the substance (233.192 g/mol), crystal forms of a perovskite structure and high-density value (6.02 g/cm-3) [173].

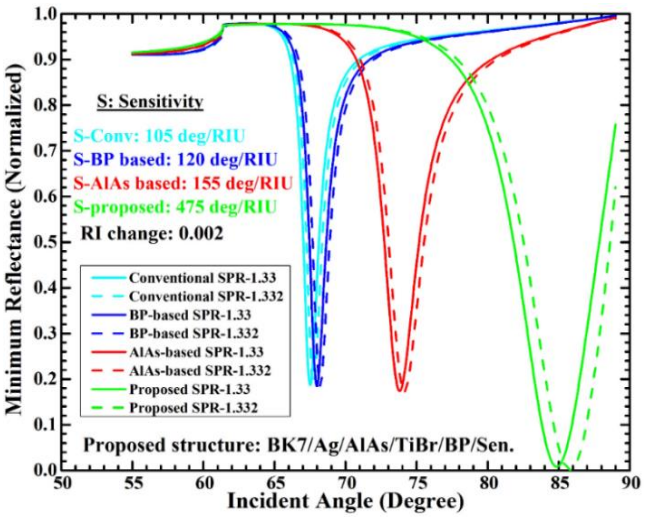

Fig. 5.11 Reflectance responses vs an angle for all defined structures.

Similarly, structure-III (i.e., AlAs-based SPR) showed more sensitivity than structure-II because of the high work function of a bandgap of 2.16 eV, a high dielectric constant of 10.9, and a high-density function of 3.81 g/cm3. Also, its cubic crystal structure offers more efficient biomolecular bindings on the AlAs surface [174]. Finally, structure-IV (i.e., proposed SPR) has been accomplished the noteworthy sensitivity, which is a huge performance enhancement than the structure-III. The reasons behind this enhancement are high RI value, high bandgap of 2.68 eV, high thermal expansion coefficient of $51\times 10^{-6}/℃$, vast density factor and dielectric constant of 7.50 g/cm^3 and 30.3, successively [174]. However, after adding the TIBr bromide

material, the SPR sensor offers massive sensitivity but increased broader SPR response, i.e., FWHM due to damping [175]. In addition, the proposed sensor has been presented the acceptable QF, FOM and CSF even though it has high FWHM. The obtained QF, FOM and CSF are 80.37RIU^{-1}, 79.72 and 77.90, respectively, for the proposed SPR sensor. This study mainly focus on the sensitivity performance of SPR because in the literature study, it has been found that the sensitivity is one of the most important parameters for better SPR biosensor. Moreover, many researchers have been explored several structures in order to improve the SPR sensitivity performance only. In addition, the higher sensitivity with minute variation in the biomolecules shows the quick response of the sensor, which is one of its great advantages. Therefore, though structure-II has a slightly higher performance in terms of QF, DA, FOM and CSF, it has a huge difference in terms of sensitivity. Therefore, the proposed structure is useful to enhance the SPR biosensor for bio-sensing applications (e.g., ssDNA) and open a novel way for TIBr utilization bio-sensing region.

Table 5.9 Measured Parameters for All Considered Structures

SPR Biosensor	Resonance angle (°)		Performance Parameters					
	1.33	1.332	$\nabla\theta_{res}$	FWHM	S (°/RIU)	QF (RUI^{-1})	FOM	CSF
I. Conv.	67.52	67.73	0.21	1.09	105	96.33	78.31	77.91
II. BP-based	67.97	68.21	0.24	1.18	120	101.69	82.90	82.47
III. AlAs-based	73.82	74.13	0.31	2.42	155	64.05	52.90	52.70
IV. Proposed	84.85	85.80	0.95	5.91	475	80.37	79.72	77.90

Moreover, the effect of TIBr in the proposed SPR structure has been observed from Fig. 5.12, which shows the reflectance responses for increasing AlAs layers. The reflectance responses in Fig. (5.12a) have been drawn for different AlAs layers at the TIBr constant thickness of 1nm, and similarly, Fig. (5.12b) shows for TIBr thickness of 3nm and Fig. (5.12c) shown for TIBr thickness of 5nm. Fig. 5.12 shows that a resonance shift occurred at each layer of AlAs. From Fig. 5.12(a-c), the performances of resonance shift change and R_{min} are contrary to each other because of the low extinction coefficient of AlAs and TIBr [175]. The FWHM of these SPR responses increases with the number of AlAs and TIBr layers due to SPs damping [175]. Fig. (5.13) presents the graphical representation of measurement of R_{min} and sensitivity for all responses in Fig. (5.13); the extreme achieved sensitivities are 190°/RIU in Fig. (5.12a), 220°/RIU in Fig. (5.12b) and 475°/RIU in Fig. (5.12c). Fig. 5.14(a-b) have been

shown the graphical representation of variations in R_{min}, resonance angle and sensitivity, respectively, with respect to the sensing RI. Furthermore, Fig. (5.14a) revealed the structure-IV offer a shallow value of R_{min} than all other structures, i.e., I, II and III. Hence, the structure-IV transfers maximum energy of incident light to the detector, in contrast to other structures. The resonance angle is directly proportional to the sensing RI. Fig. (5.14b) has been exhibited the sensitivity variations with respect to the sensing RI, resulting that the proposed structure has been accomplished a huge sensitivity compared to the structure-III, which is better than structure-II and I.

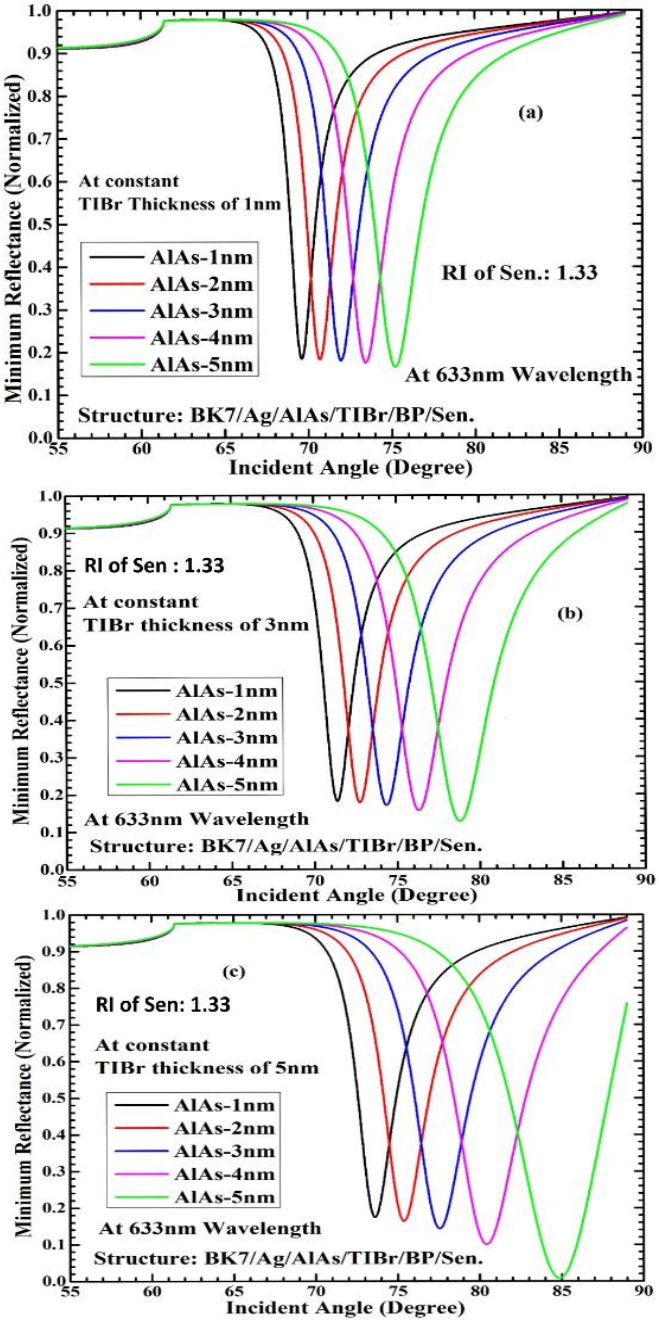

Fig. 5.12 SPR responses vs an angle at TIBr thickness of (a) 1nm (b) 3nm (c) 5nm.

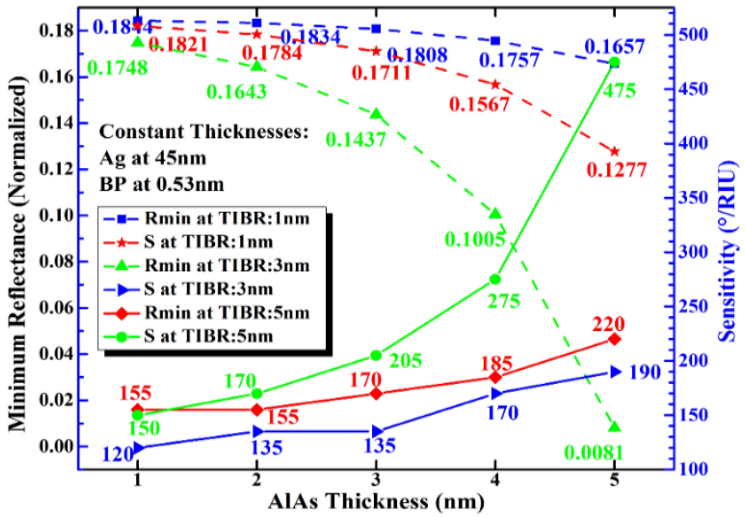

Fig 5.13 Graphical representation of R_{min} and sensitivity of proposed sensor.

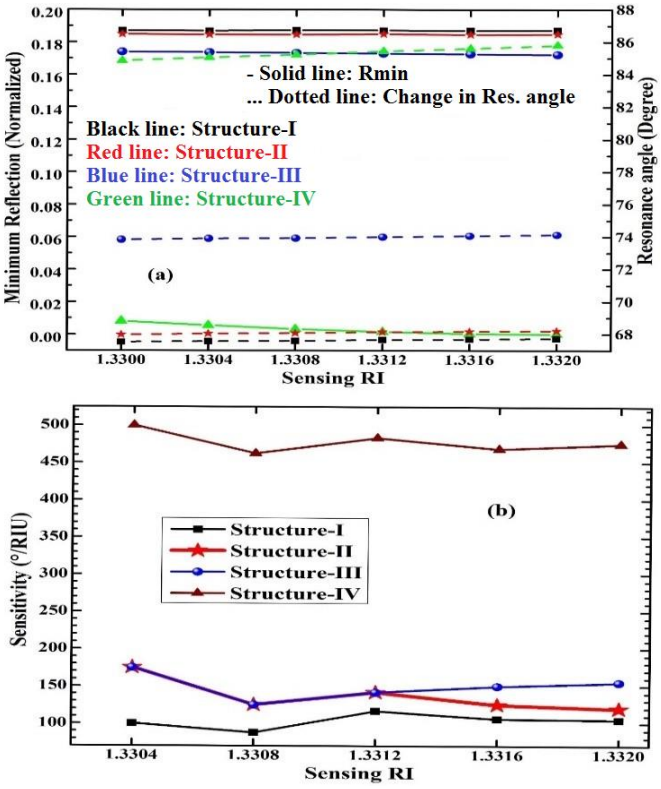

Fig. 5.14 (a) R_{min} and resonance angles (b) Sensitivity variations.

The evanescent field intensity (EFI) or electric field enhancement factor (EFEF) is a function of both incident light angle and its polarization components. The EFI and EFEF are utilized for the vibrations of p-polarized vectors as a function of the coordinate system at the interface plane, which is defined as being parallel to the excited light beam. Eq. (5.14) and (5.15) are mathematical expressions for computing the EFI and EFEF, respectively [176]. Where, n is the ration of N^{th} layer and prism's RI, t is the transmittance coefficient of the SPR sensor.

$$EFI = \frac{4\cos^2\theta\sin^2\theta}{(1-n^2)\left[(1+n^2)(\sin^2\theta - n^2)\right]} \tag{5.14}$$

$$EFEF = \frac{\varepsilon_1}{\varepsilon_n}|t|^2 \tag{5.15}$$

Fig. 5.15(a-d) explore the (EFI) at each surface interface for all structures, including I, II, III and IV. It is accomplished the highest EFI at the Ag-sensing interface for structure-I, BP-sensing interface for structure-II, AlAs-BP interface for structure-III and TIBr-BP interface for structure-IV. Structure-II to IV confirm that the BP of 2D-material increases the field intensities, and the TIBr-BP interface is furnished the highest-intensity factor rather than all other interfaces. The EFI is decayed to zero at the end of the angular variations. Fig. 5.16 presents the electric field enhancement factor (EFEF) with respect to an incident angle for all structures, this can be measured by applying Eq. (5.15) [175]. In the literature, it is well known that the field intensity is inversely proportional to the reflectivity (i.e., its extreme value of field intensity is minimum in the reflectivity). The greater SPs' excitation is transpired at the instant of strongest field intensity due to less R_{min}. From Fig. 5.16, it can be easily concluded that the structure-IV generates high EFI, which symbolizes greater SPs excitation compared to all other structures, i.e., structure-III, II and I.

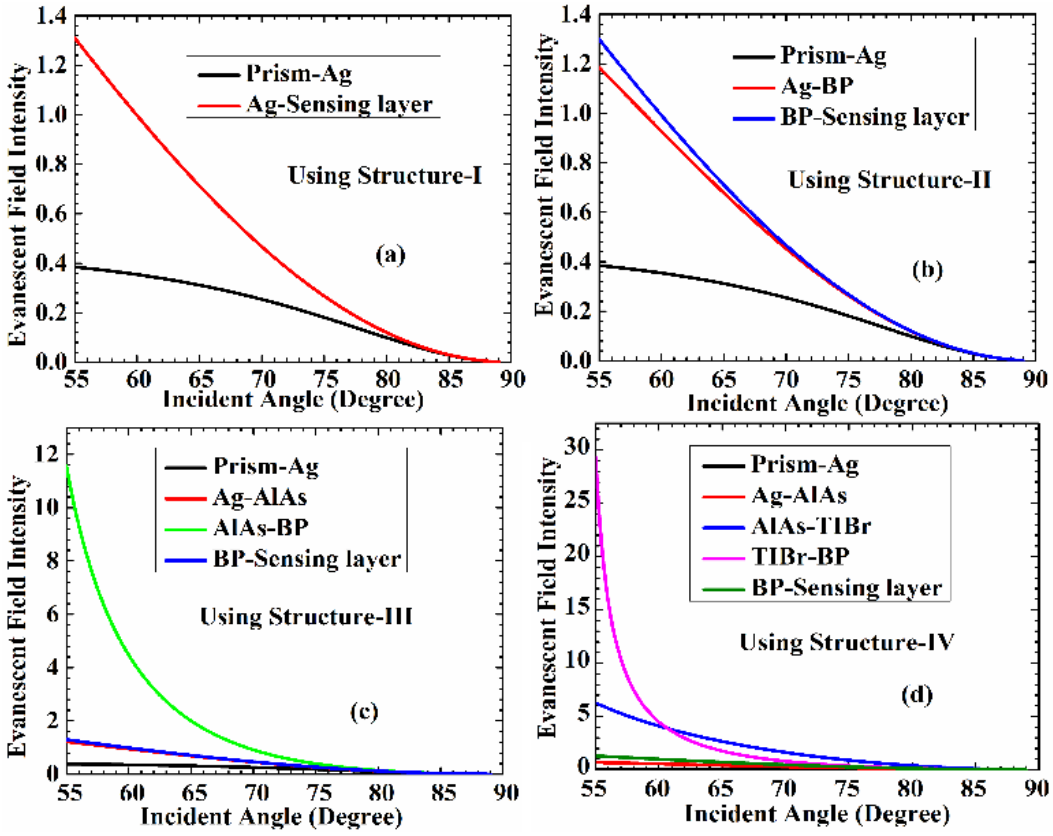

Fig. 5.15 EFI for (a) Structure-I (b) Structure-II (c) Structure-III (d) Structure-IV.

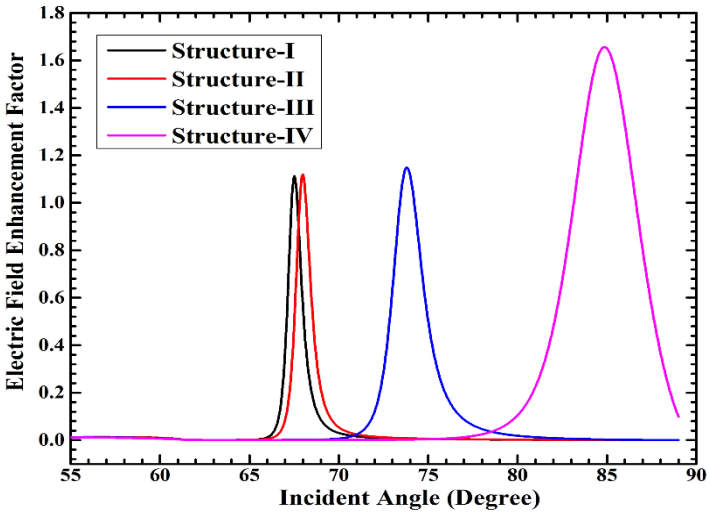

Fig. 5.16 Representation of EFEF vs Incident angle for all structures.

Finally, Table 5.10 presents a comparative study between the performances of the proposed structure and existing structures. From that table, it is evident the proposed structure is furnished the enhanced sensitivity of 475, QF of 80.37, and FOM of 79.72. Moreover, it also introduced the novel SPR parameter, i.e., CSF of 77.90. Therefore, the comparative study reveals that the proposed SPR sensor furnishes an agreeable solution for bio-sensing applications, such as ssDNA, with high sensitivity, QF, FOM, and CSF.

Table 5.10 Performance Comparative Table

Ref. No	Utilized technique	Structure of the SPR sensor	S (°/RIU)	QF (RUI^{-1})	FOM	CSF
[33]	Prism	Prism/Au/BP	180	-	-	-
[155]	Prism	Prism/Air/MoS_2/Al/MoS_2/graphene	190.83	-	-	-
[170]	Prism	Prism/Au/MoS_2/Au/graphene	182	-	-	-
[171]	Prism	Prism/Ag/$PtSe_2$	162	-	14.93	-
[171]	Prism	Prism/Au/$PtSe_2$	165	-	14.12	-
[172]	Prism	Prism/Ag/$PtSe_2$/WS_2	194	34.22	17.64	-
[172]	Prism	Prism/Au/$PtSe_2$/WS_2	187	29.39	15.72	-
Proposed work	Prism	Prism/Ag/AlAs/TIBr/BP	475	80.37	79.72	77.90

For a better understanding of the proposed sensor impact, the performance shows the reflectance intensity with respect to an angle for different wavelength regions at three metal

thicknesses. The RIs for each layer at different wavelengths have been obtained from equations in [138, 176]. Fig. (5.17) depicts reflectance responses for different wavelength regions, such as 630, 650, 670, 690, and 700nm at sensing RI of 1.33, whereas Fig. (5.17a), (5.17b), and (5.17c) represent for Ag thickness of 40, 45 and 50nm, respectively. Fig. (5.18a), (5.18b), and (5.18c) explore similar types of responses at the sensing RI of 1.332.

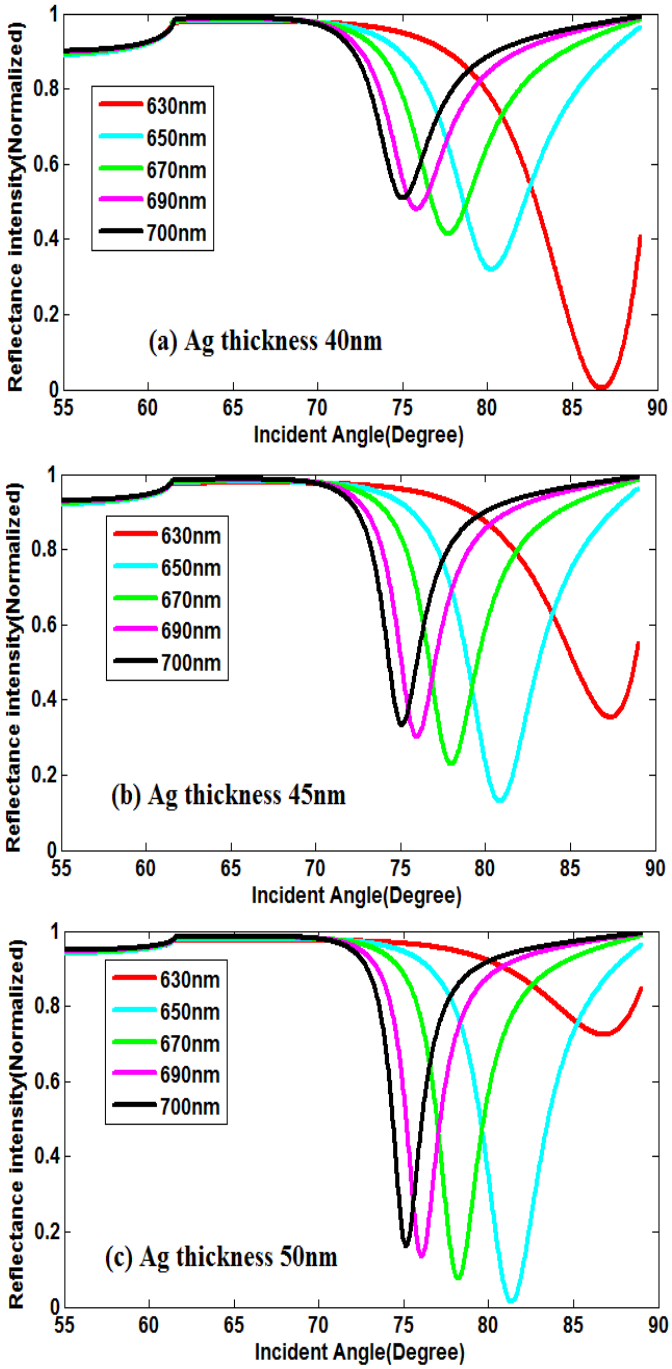

Fig. 5.17 Reflectance intensityat at ns=1.330 and Ag thickness of (a) 40 nm (b) 45 nm (c) 50 nm.

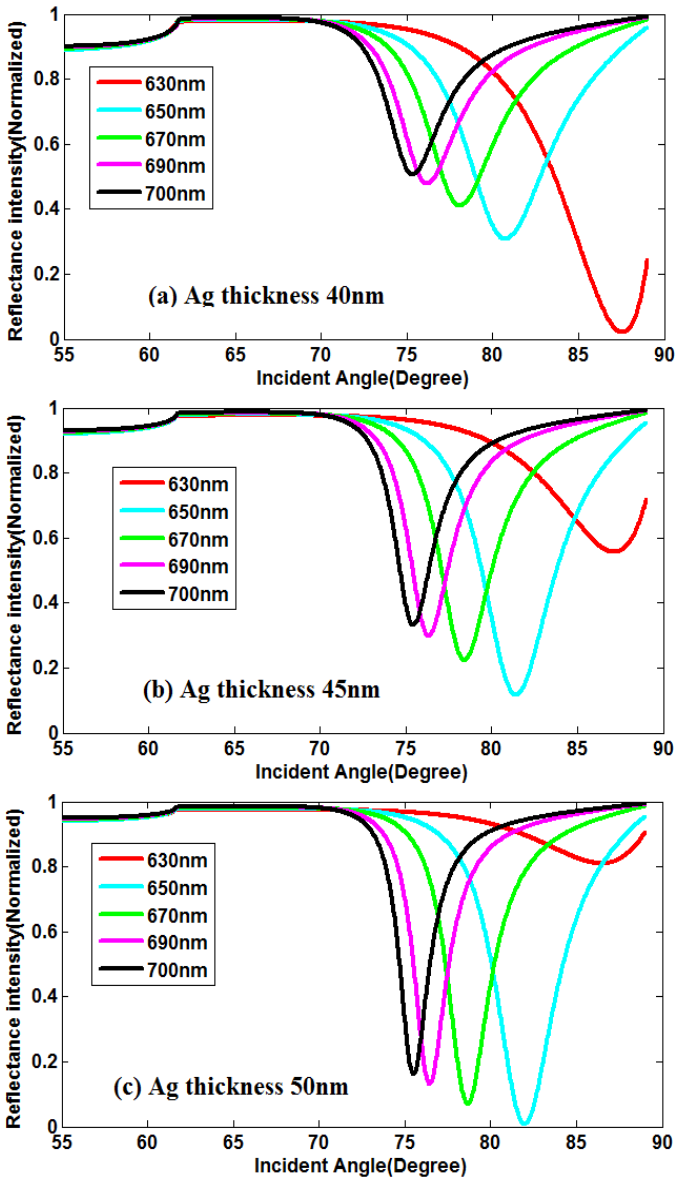

Fig. 5.18 Reflectance intensityat at ns=1.332 and Ag thickness of (a) 40 nm (b) 45 nm (c) 50 nm.

The results obtained in terms of change in resonance angle ($\nabla\theta_{res}$) and sensitivity are exhibited in Fig. 5.19. The results have been demonstrated the highest $\nabla\theta_{res}$ of 0.85 and sensitivity of 425°/RIU are achieved for the wavelength region of 630nm at Ag thickness of 40nm. Therefore, it signifies that the proposed structure furnishes magnified performance at 630nm wavelength region, which is proved using the angular variation method as well as the wavelength variation method. The larger wavelength region is applicable for SPR sensor at the larger metal film thicknesses. However, previous research has shown that lower wavelengths offer low penetration depth with traditional SPR, resulting in lower SPR performance, but this study reveals the opposite with an SPR structure using a novel dielectric material of TIBr. Therefore, an incident optical radiation absorbs into plasmonic modes in the proposed SPR

sensor, resulting in standing waves on the metal film. These waves drive strong EM fields that are existing at the prism and metal interface.

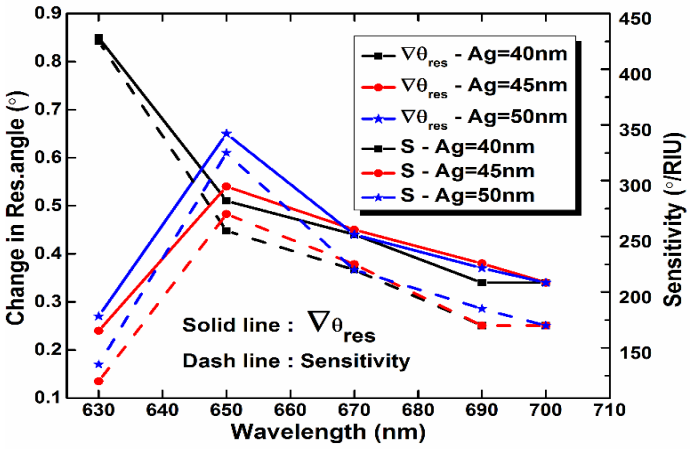

Fig. 5.19 Measured parameters of change in resonance angle and sensitivity.

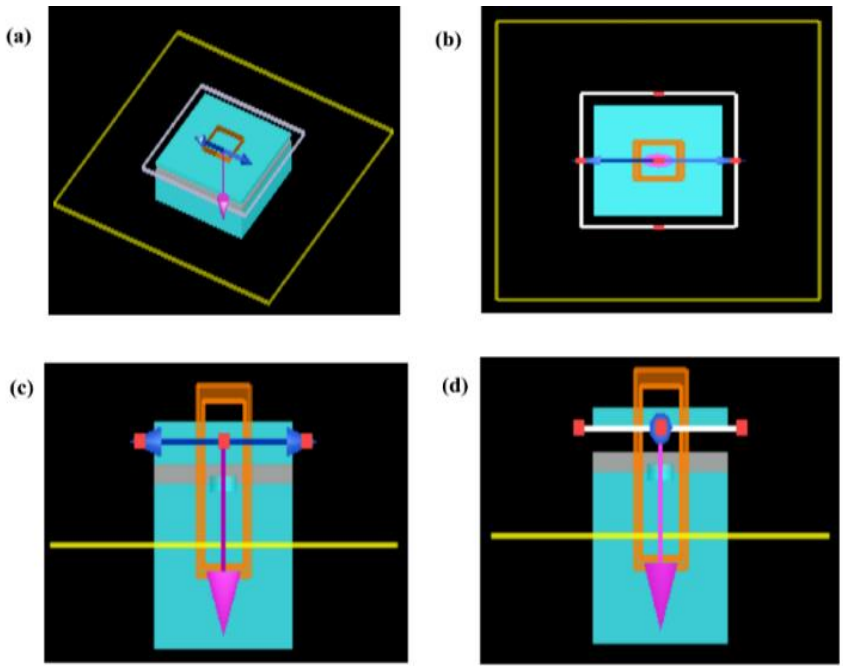

Fig. 5.20 SPR design (a) Perspective view (b) xy view (c) xz view and (d) yz view.

Furthermore, the Finite-difference time-domain (FDTD) is a numerical analysis technique, used for modelling computation electrodynamics. Fig. 5.20 represents the proposed SPR sensor structure design by considering the Lumerical FDTD solution, whereas, Fig. 5.20(a) shows a perspective view, Fig. 5.20(b) xy view, Fig. 5.20(c) xz view, and Fig. 5.20(d) yz view. The fabrication process is used the structural modelling, adding the respective materials to create a complete structure. The objective editor of FDTD technique sets the RIs and all other parameters as default, where all utilized parameters are considered as generalized

measurement parameters, including the substrate width of sensor. The design parameters for the proposed SPR using FDTD are shown in Table 5.11. The design process considered the perfectly matched layer (PML) boundary conditions around the structure, auto non-uniform mesh with an accuracy of 2 for protection from the mechanical and mechanical defects. Furthermore, Fig. 21(a-c) depict the spatial distribution for the fundamental mode of E-field magnitude (|E|), H-field magnitude (|H|) and power amplitude (|P|), respectively in the proposed SPR sensor. Similarly, Fig. 5.22(a-c) show spatial distributions for SPP mode of E-field, H-field and power amplitude, respectively. From the field and power distribution of the proposed SPR sensor, it can be found that at E-field magnitude has better capabilities to strike the metal surface's free electrons in the fundamental mode and the SPP mode. Finally, the analysis has been demonstrated that the incident light is efficiently coupled into plasmonic modes for Ag metal surface, leading to higher SPR performance.

Table 5.11 Design Parameters for Proposed SPR Sensor Using FDTD

	Axes boundary (μm)			Additional Parameters
	X-span	Y-span	Z-span	
BK7	0-20	0-20	-4 – 0	-
Ag	0-20	0-20	0-0.45	-
AlAs	0-20	0-20	0.45-0.95	-
TIBr	0-20	0-20	0.95-1.45	-
BP	0-20	0-20	1.45-1.503	-
Sensing	-	-	1.503-1.523	Radius =2 μm
FDTD	0-6	0-6	0-4	Simulation time= 5000Hz, Stability factor=0.99 and time step=0.0061657.
Source	0-24	0-24	0-1	Z-axis in Backward direction
Transmittance	0-50	0-50	-1.5 - 0	2D Z-normal

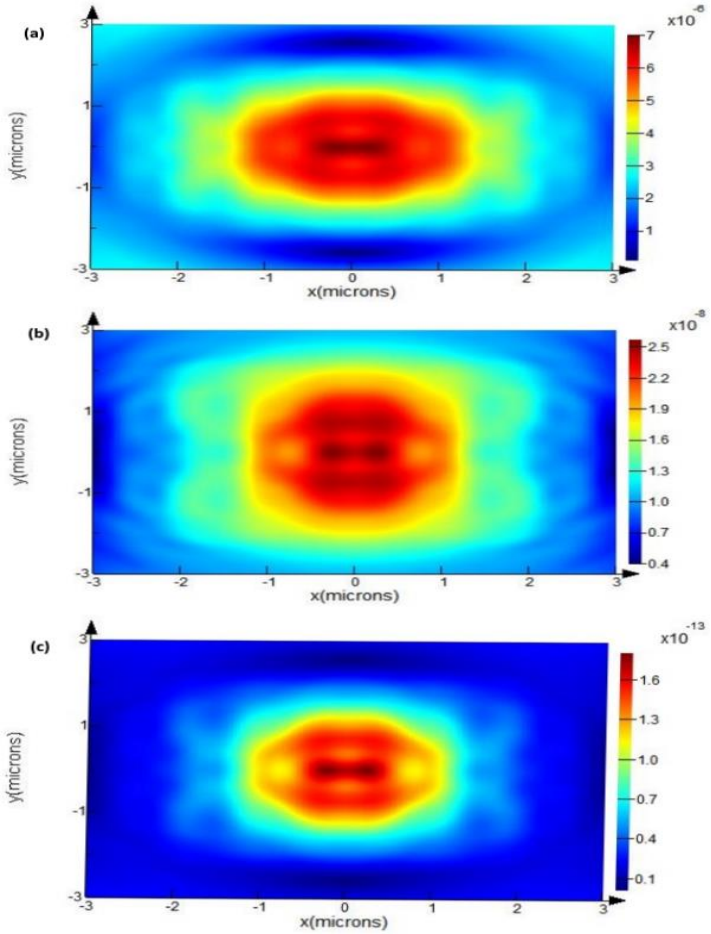

Fig. 5.21 (a) E-field (b) H-field (c) Power distribution field.

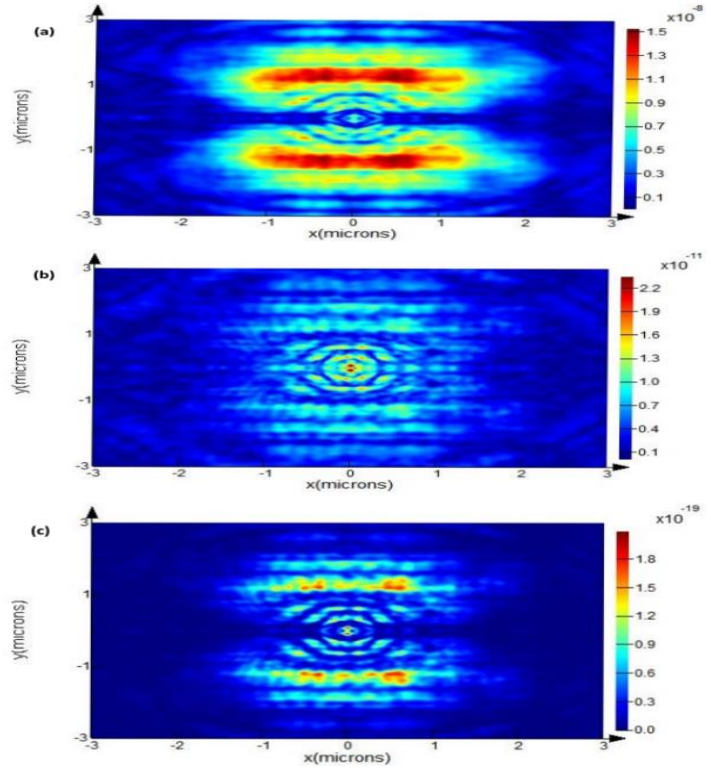

Fig. 5.22 (a) E-field (b) H-field (c) Power distribution field.

5.5 Conclusion

The high-performance SPR sensor is shown in this chapter employing novel hybrid structures. This work has been executed into two significant forms. Firstly, a highly performed SPR biosensor has been proposed by employing the hybrid structure of $BiFeO_3$-bromide material-BP/graphene. The numerical study has been considered to show the impact of different prisms on high performance using the proposed SPR biosensor. The numerical simulation results have been demonstrated that relatively high performance could be achieved when the prism's RI is relatively low. Therefore, to achieve higher SPR performance, the BK7 has been employed as a coupling prism in the proposed structure due to low RI. Furthermore, the dielectric materials, including the $BiFeO_3$, are employed in the proposed structure to improve the SPR performance. Similarly, the BP/graphene layer is used for enhancing absorption capability and applied as the bio-molecular recognition element, which can protect the sensor from being oxidized. Numerical results have been shown that the obtained optimized thickness of $BiFeO_3$ and bromide layer are 5nm and 5nm, respectively. Also, the highest SPR performances, such as a sensitivity of 468 deg/RIU, QF of 87.80RIU^{-1}, FOM of 87.79, DA of 0.44, have been achieved for the BP-based SPR structure ($BiFeO_3$-TIBr-BP), which are 1.32, 1.46, 1.51, 1.47 times higher than the respective performance of the graphene-based structure.

Secondly, being inspired by the impact of TIBr, numerical analysis of another high-performance SPR biosensor has been proposed employing TIBr-based structure. Three other structures have been considered for the performance comparison. For optimizing the Ag thickness of 45nm and TIBr thickness of 5nm by iteration method of Fresnel's R_p mode analysis, the SPR reflectance responses are plotted and accomplished a low R_{min} and high resonance shift. Furthermore, the performance analysis has been done for all structures and found the maximum sensitivity is 475°/RIU for structure-IV, 155°/RIU for structure-III, 120°/RIU for structure-II, and 105°/RIU for structure-I. From the results, it has been clearly observed that the sensitivity of the structure-IV is 4.52, 3.96, 3.06 times higher than that of structure-I, II, III, respectively. Additionally, the structure-IV shows a satisfactory QF of 80.37 RIU^{-1}, FOM of 79.72 compared to the existing sensors. This study has also computed the overall performance parameter and found CSF of 77.9 for the proposed structure. Furthermore, the achieved sensitivity performance of structure-IV is endorsed with the wavelength variation method, and also with the field intensity performance. Results show that it offers a very low value of R_{min} and high field intensity using the transfer matric method. Moreover, the high field intensity performance is endorsed with the FDTD solution tool by plotting EM field

distributions. As the presented SPR sensors have been achieved a magnified value of sensitivity compared to the existing works, therefore, they can be established a remarkable stage in the field of biomedical and biomolecular.

Chapter-6

High-performance SPR sensor for urea detection at different wavelength regions

6.1 Introduction

Different wavelength regions, such as high visible wavelengths and near infrared region, offers numerous advantages over IR in terms of speed (easier handling, no sample preparation required), bulk material information, and adaptability. Moreover, these wavelengths may be used to qualify a variety of chemical and physical properties, and it can also be used in a process environment. On the other hand, the kidneys play a key role in the human body for sustaining human health. The high levels kidneys fail to extract the waste, which can flow out in the form of urine; it can accumulate in the blood and damage the human body. [61]. Therefore, this chapter presents the numerical analysis of high-performance SPR senor employing emerging 2D and dielectric materials based structures at near infrared region wavelength. Because, the surface plasmon resonance (SPR) is a promising optical technique, and is used to monitor the bio-molecular interaction analysis, and detection in liquid samples. It is a non-invasive device for early detection using label-free and real-time methods [62, 177].

Therefore, this chapter presents a high-performance SPR sensor for urea detection employing three different dielectric and 2D materials-based structures at different wavelength regions. Firstly, performance enhancement of SPR sensor is shown employing molybdenum disulfide (MoS_2)-Dielectric materials-MoS_2 structure. Secondly, the SPR sensor based on the gold (Au)-beryllium oxide (BeO)-gallium phosphide (GaP) structure is presented. Thirdly, the SPR sensor employing an Au-dielectric material-based structure is presented. In each event, the metal film thickness is optimized by plotting the reflectance curves. Then, the impact of the proposed structure on the SPR sensor is shown. The performances of the proposed sensors are analyzed in terms of sensitivity and quality factor. Finally, the comparative study is demonstrated that the proposed sensors are accomplished better SPR performance compared to the existing sensors.

6.2 Numerical Expressions

To increase the impulse and wavenumber at an angle, the SPR sensor utilizes the P-polarized light. In SPR geometry, the incident P-polarized light beam should match its impulse factor to that of the plasmon to excite resonance condition of surface plasmons. Therefore, Eq.

(6.1) represents the mathematical expression for resonance condition occurrence of resonance [178].

$$n_p \sin\theta_{res} = \sqrt{\frac{\varepsilon_m \varepsilon_d}{\varepsilon_m + \varepsilon_d}} \quad (6.1)$$

Where, n_p, θ_{res}, ε_m and ε_d denotes the prism's RI, resonance angle (the angle where it shown minimum reflectance response), the dielectric constant of metal and dielectric mediums, respectively. Eq. (6.2) represents the mathematical expression to compute the reflectance of SPR response. This expression can be applied for multi-layered structures as well.

$$R_{pms} = \left|r_{pms}\right|^2 = \left|\frac{r_{pm} + r_{ms}\exp(2ik_m d_m)}{1 + r_{pm} r_{ms}\exp(2ik_m d_m)}\right|^2 \quad (6.2)$$

Furthermore, the analysis determines the SPR performance in terms of sensitivity and quality factor (QF). Sensitivity is defined as the change in resonance angle to change in sensing RI, whereas QF is inversely proportional to FWHM. It is an essential parameter for ensuring a better SPR sensor. The computation of sensitivity and QF is done by applying Eq. (6.3) and (6.4).

$$\text{Sensitivity (S)} = \frac{\text{Change in Res. angle } (\theta_{res})}{\text{Change in RI } (\nabla n)} \quad (6.3)$$

$$\text{Quality Factor (QF)} = \frac{S}{\text{Full width half maximum (FWHM)}} \quad (6.4)$$

6.3 Design and Simulation Results

6.3.1 A Performance Enhancement of SPR sensor for urea detection using MoS_2-Dielectric materials-MoS_2 Based Structure

The schematic structure of the proposed SPR sensor to detect the urea has been depicted in Fig. 6.1. The structure design has been done on the basis of Kretschmann configuration with soda lime glass (SLG), which operates as coupling prism. Numerical analysis of work has been investigated at a wavelength of 750 nm, and RIs of all layers are operated at this wavelength. This structure comprises of seven layers, such as prism, Au, MoS_2, GeO_2, GaP, MoS_2 and sensing medium. SLG prism is considered as first layer of the structure, having the refractive index (RI) of 1.503, which shows better resonance dip change [55, 61]. Moreover, the second layer is comprised of Au, as plasmonic material, having RI of 0.14891+4.7830i [63, 64]. The Au thickness has been optimized by applying the iteration method [55]. The third and sixth layers have been comprised of MoS_2, as coated on both surfaces of dielectric layers. The RI and thickness of MoS_2 are 4.815 and 0.64nm, respectively [64]. The fourth and fifth have been comprised of GeO_2 and GaP, as coated over the Au with the RIs of 1.6034 and 3.2791 [161],

and thicknesses of 5nm and 5nm, respectively. This study is also considered the dielectric materials thicknesses are 5nm and 5nm, where it provides more absorption capacity to achieve higher SPR performance [55]. Finally, the seventh layer is comprised of sensing medium with RIs of 1.339 and 1.342 for 2.5 and 5 gm/dl, respectively, whereas the reference urea RI is considered as 1.335 for calculating SPR parameters [55, 64].

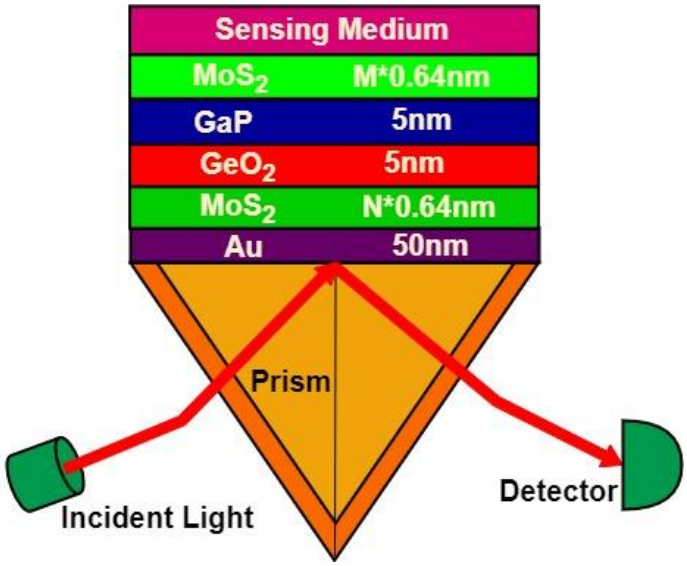

Fig 6.1. Schematic structure of proposed SPR biosensor.

Initially, the performance shows that optimization of the metal film thickness for the proposed SPR structure. Fig. 6.2 exhibits the reflectance intensity performance in terms of an angle for various Au thicknesses (30–60nm with an interval of 5nm), and remaining layers of thicknesses are kept constant, i.e., single MoS_2 of 0.64nm, GeO_2 of 5nm, GaP of 5nm and MoS_2 of 0.64nm. At this movement, the RI of sensing medium is considered as 1.335 [64]. Many other authors have been considered that less R_{min} as a reference for optimizing the layer thickness [128]. With this reason, this study plots reflectance curves for optimizing the Au thickness and observed that less R_{min} of 0.0023 is obtained at the Au thickness of 50nm, and at remaining events, the R_{min} is increasing. The less R_{min} is occurred due to the spatial extension of SPs in a medium that depends on SP's propagation length (PL) in the parallel direction [55]. Therefore, this work has been considered the Au thickness at 50nm in the proposed SPR structure that can be used for further analysis of the proposed structure.

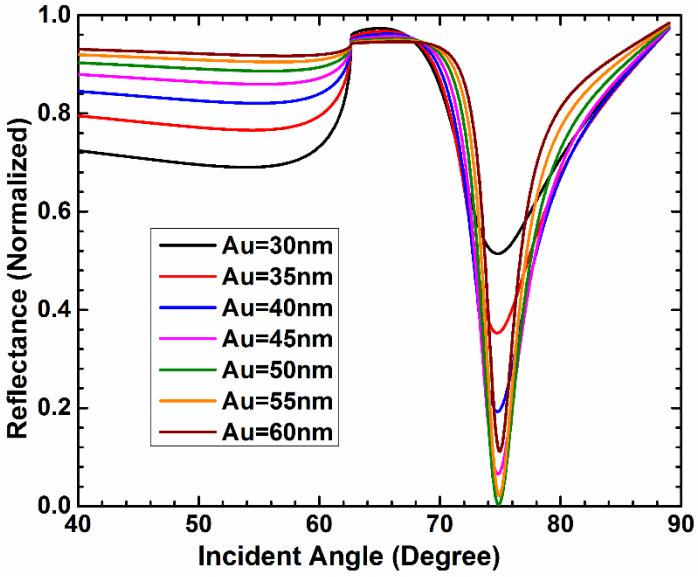

Fig. 6.2 Reflectance response vs an angle for different Au thicknesses.

Furthermore, the study exhibited the performance of the proposed SPR structure in terms of sensitivity. In the literature, it has been discovered that double and multilayers of MoS_2 layers improve the sensitivity performance of an SPR sensor. Therefore, Fig. 6.3 to 6.5 present the reflectance intensity with respect to the angle for number of MoS_2 layers. For plotting these responses, the one of the MoS_2 thickness is confirmed at 0.64nm, whereas another MoS_2 layer varies at different amounts including monolayer, bilayers, 3-layers and 4-layers. Fig. 6.3 depicts the reflectance curves at the sensing RI of 1.335, and the observed resonance angles are 74.87, 76.54, 78.60 and 81.30° for respective MoS_2 layers. Similarly, the resonance angles of 75.51, 77.28, 79.48 and 82.38° are achieved for the reflectance curves of Fig. 6.4; and finally, the resonance angles of 76.05, 77.87, 80.17 and 83.26° are obtained for the reflectance curves of Fig. 6.5. Moreover, the overall performance of R_{min}, resonance angles and FWHM for Fig 6.3 to 6.5 have been mentioned in Table 6.1. The SPR performance of sensitivity and QF are computed by applying Eq. (6.3-6.4), and the computed parameters have been mentioned in Table 6.2. The results reveal that the sensitivity increases with the number MoS_2 layers in the proposed structure. The achieved sensitivities are 160, 185, 220 and 270°/RIU for respective MoS_2 layers at ∇n of 0.004 of the urea sample, whereas 168.57, 190, 224.29 and 280°/RIU for respective MoS_2 layers at ∇n of 0.007 of the urea sample. Moreover, achieved QFs are 37.74, 37.37, 38.33 and 39.88RIU^{-1} for respective MoS_2 layers at ∇n of 0.004 of the urea sample, whereas 39.76, 38.88, 39.08 and 41.36RIU^{-1} for respective MoS_2 layers at ∇n of 0.007 of the urea sample. Enhanced performance of the proposed structure is obtained because of the higher RI, higher penetration depth of SPW and higher molecular

absorption capability of the top layer, i.e., MoS_2. The spectral width of the SPR curve is increased with the number of MoS_2 layers due to the damping effect [32].

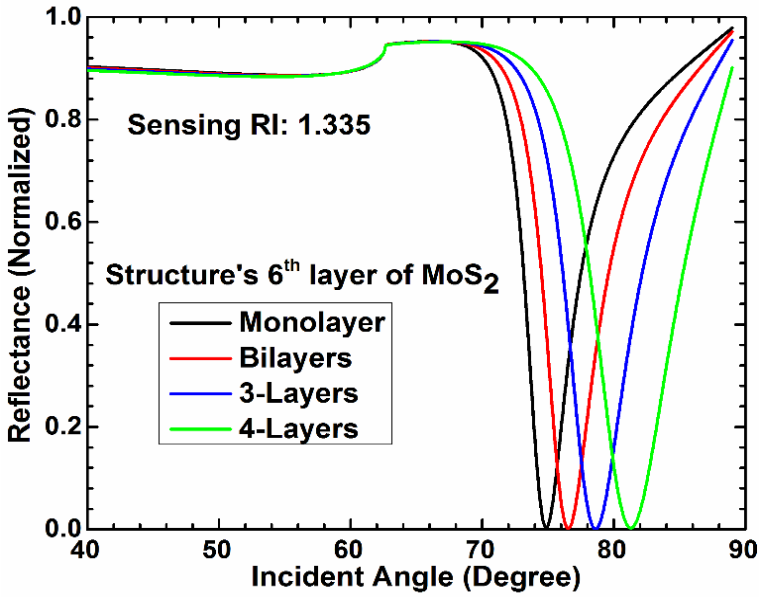

Fig. 6.3 Reflectance response in terms of an angle at sensing RI of 1.335.

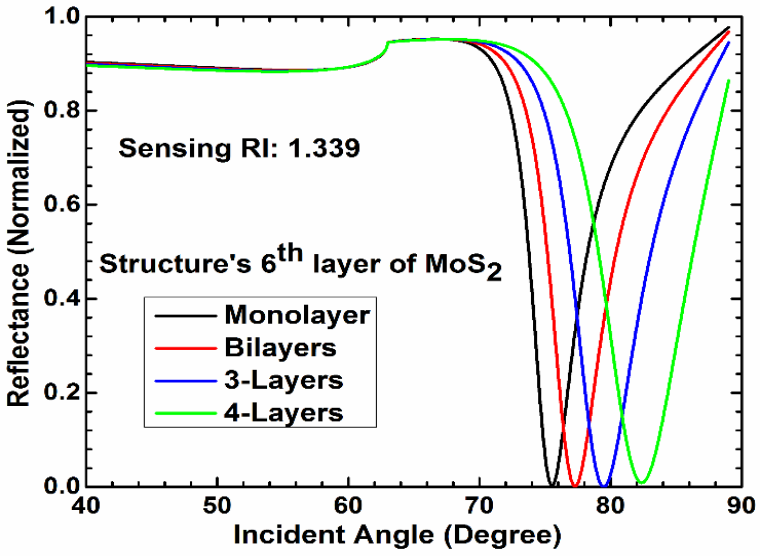

Fig. 6.4 Reflectance response in terms of an angle at sensing RI of 1.339.

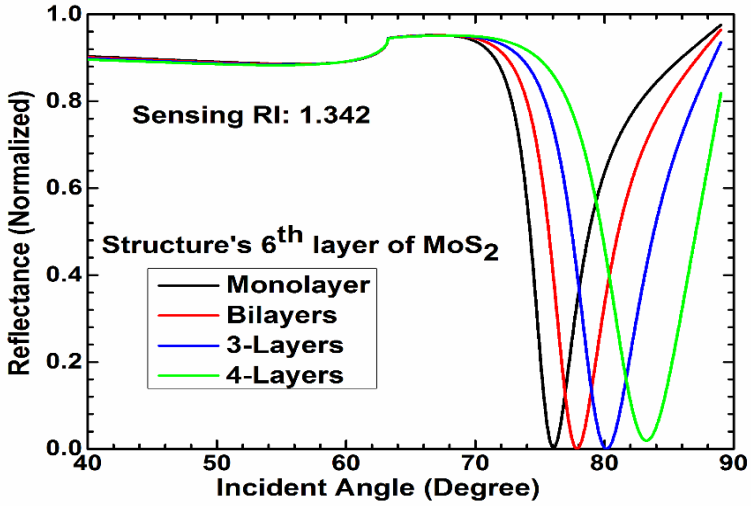

Fig. 6.5 Reflectance response in terms of an angle at sensing RI of 1.342.

Table 6.1. Measured Parameters for Fig. 3 to 5

Number of MoS2 layers (M*0.64)	Minimum Reflectance (R_{min}) for Fig. 3 to 5			Resonance angle (θ_{res}) for Fig. 3 to 5 (°)			FWHM
	1.335	1.339	1.342	1.335	1.339	1.342	
1	0.0031	0.0027	0.023	74.87	75.51	76.05	4.24
2	0.0019	0.0013	0.00082	76.54	77.28	77.87	4.95
3	0.00029	0.00005	0.00028	78.60	79.48	80.17	5.74
4	0.0025	0.0087	0.0190	81.30	82.38	83.26	6.77

Table 6.2. Measured Parameters of sensitivity and quality factor for Fig. 3 to 5

Number of MoS2 layers (M*0.64)	Quality Factor (RIU^{-1})		Sensitivity (°/RIU)	
	At ∇n=0.004	At ∇n=0.007	At ∇n=0.004	At ∇n=0.007
1	37.74	39.76	160	168.57
2	37.37	38.38	185	190
3	38.33	39.08	220	224.29
4	39.88	41.36	270	280

Table 6.3. Performance Comparison of Proposed SPR Sensor with Existed SPR

References	SPR Structure	Sensitivity (°/RIU)	Quality Factor (RIU^{-1})
[61]	Prism-Cu-Graphene-Sensing	32.653	-
[63]	Prism-Chr-Au-Graphene-MoS_2 -Sensing	77.10	-
[64]	Prism-Chr-Al_2O_3-MoS_2-Graphene-Sensing	134.68	-
[62]	Prism-Chr-Au-MoS_2-Graphene-Sensing	172.86	-
Proposed work	Prism-Au-GeO_2-GaP-Sensing	280	41.36

Finally, the proposed structure performance is compared with the existing SPR structures, which are done by other researchers at 785nm wavelength. From Table 3, it can be clearly witnessed that the proposed sensor exhibits the better SPR performance rather than others' structures. The maximum achieved SPR performances are sensitivity of 280°/RIU and QF of 41.36RIU^{-1}, which prove the proposed structure highly exalts the SPR sensor and put it at a remarkable stage in biomedical and bio-molecular fields.

6.3.2 A Highly Performed SPR sensor for Urea Detection Using Au-BeO-GaP Based structure

The schematic structure of a novel SPR sensor is shown in Fig. 6.6 for urea detection. The Kretschmann configuration, which offers efficient light coupling, has been considered for sensor's design. The performance of detection process has been analyzed at a wavelength of 670nm (that can offers minimum Kerr effect) exploiting the angular interrogation technique and transfer matrix method. This structure consists of five layers, such as boron kron-7 (BK7) prism, Au, BeO, GaP and sensing medium. The BK7 prism has been considered as first layer with the refractive index (RI) of 1.5139, which can furnish the higher SPR parameters in terms of sensitivity and QF [155]. Furthermore, the second layer, Au is placed as plasmonic material with RI of 0.13767+3.7917i [179]. The thickness of Au is optimized by applying the iteration process of reflection mode theory. The third layer and fourth of BeO and GaP are deposited over the Au, having the RIs of 1.7158 and 3.2791, and thicknesses of 5nm and 5nm, respectively. Finally, the fifth layer is compound of the sensing medium, which has the presence of urea with refractive indexes of 1.337, 1.339 and 1.342 for 0.625, 2.5 and 5gm/dl,

respectively, whereas the normal urea RI of 1.335 is considered as reference for the SPR measurement [161].

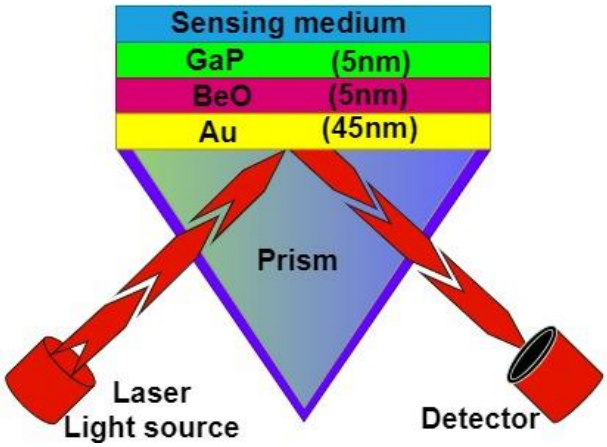

Fig. 6.6 The proposed SPR sensor for urea detection at 670nm wavelength.

In this work, as a first event, the performance of minimum reflectance (R_{min}) is shown the optimization of Au layer thickness that shows more SPs on the prism's surface. In order to shows it, Fig. 6.7 depicts the reflectance curves for different Au thicknesses (30 to 60nm with an interval of 5nm). Results show that less R_{min} of 0.0001 is obtained at the Au thickness of 45nm. The less R_{min} demonstrates the maximum light energy transfers to the SPW that leads to higher performance.

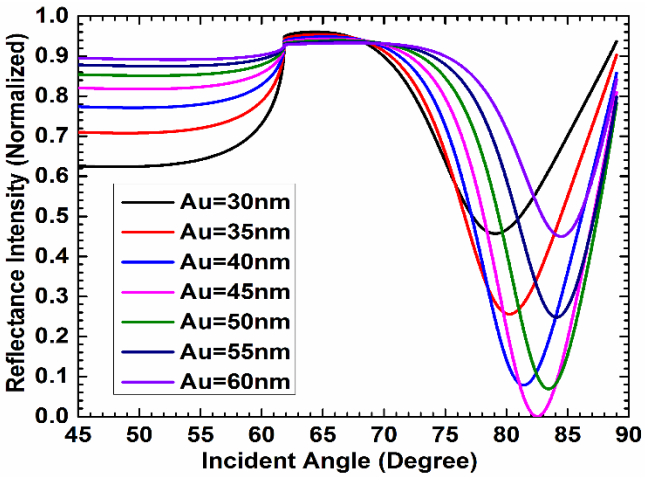

Fig. 6.7 Reflectance response vs angle for different Au thicknesses.

Furthermore, the optimal performance of the proposed structure is shown by comparing with the conventional and BeO-based SPR, as shown in Fig. 6.8. The reflectance curves of Fig. 6.8 are plotted for the sensing RI of 1.335. The black, red and blue colours denote for the conventional, BeO-based and proposed SPR structures, respectively. The computed parameters, such as R_{min}, θ_{res} and FWHM, for Fig. 6.8 have been recorded in Table 6.4. It can be easily noticed that as the number of layers is increasing in the structure, the resonance

angle is moving forward due to changes in the SPR sensor. The R_{min} performance demonstrates the proposed SPR sensor has been achieved less R_{min}, which is 6.47 and 6.06% better than the conventional and BeO-based SPR, respectively, due to low absorption loss. The proposed structure has a high FWHM due to the high damping effect [128] and a rising number of layers, yet it retains a high absorption capability through BeO and GaP.

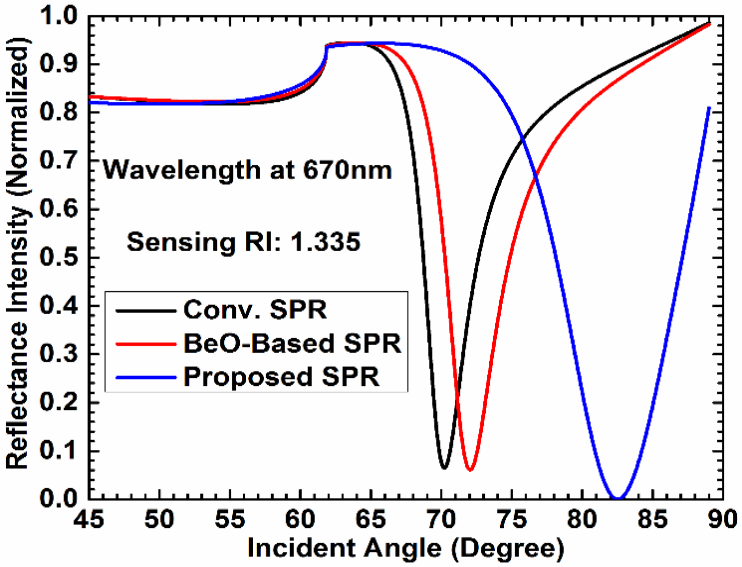

Fig. 6.8 Reflectance intensity vs angle at for sensing RI of 1.335.

Table 6.4 Computed Parameters for Sensing RI of 1.335

Structure Name	R_{min}	θ_{res}	FWHM
Conv. SPR	0.0647	70.24	3.85
BeO-based SPR	0.0606	72.04	4.51
Proposed SPR	0.0001	82.53	8.58

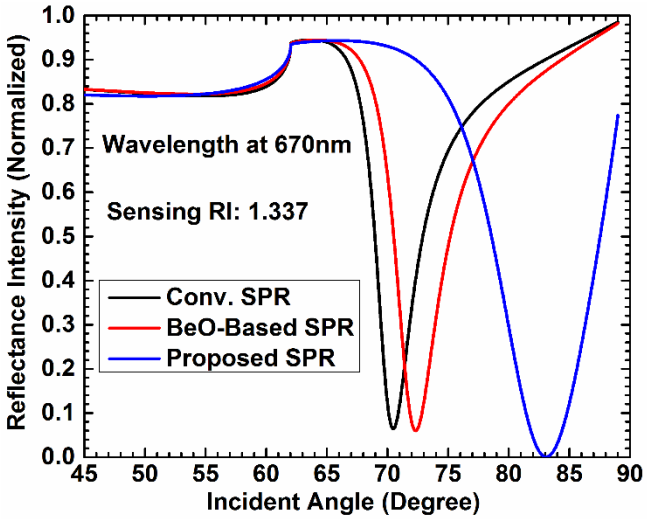

Fig. 6.9 Reflectance intensity vs angle at for sensing RI of 1.337.

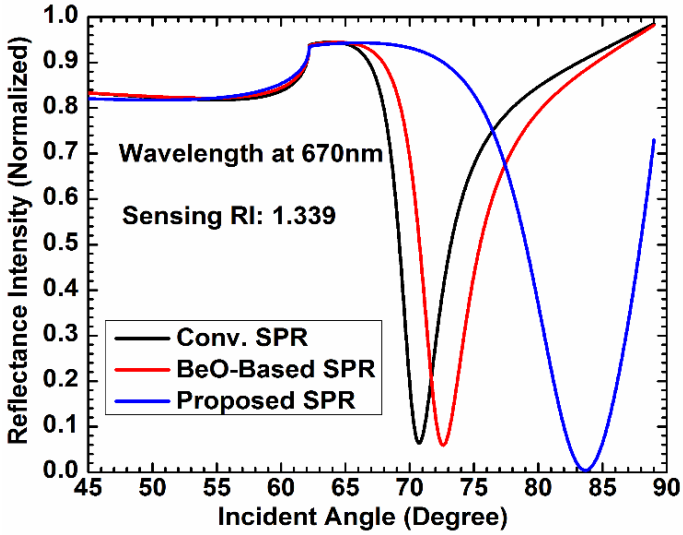

Fig. 6.10 Reflectance intensity vs angle at for sensing RI of 1.339.

Furthermore, Fig. (6.9) to (6.11) depict the reflectance curves for the considered three structures at different sensing RIs, such as 1.337, 1.339 and 1.342, respectively. The sensitivity and QF of the SPR are evaluated, and the computed parameters for Fig. (6.9) to (6.11) have been listed in Table 6.5. The maximum accomplished sensitivities are 125.71, 145.71 and 288.57°/RIU for conventional, BeO-based SPR and proposed SPR sensors, respectively, at ∇n amounts of 0.007 of the urea samples. The results have been demonstrated that the proposed sensor accomplished the maximum sensitivity of 285°/RIU, which is 2.59 and 2.11 times higher compared to the conventional and BeO-based structure, for ∇n amount of 0.002. Similarly, the maximum sensitivity of 285°/RIU, which is 2.37 and 1.96 times higher compared to the conventional and BeO-based structure for ∇n amount of 0.004. The maximum sensitivity of 288.57°/RIU, which is 2.29 and 1.98 times higher compared to the conventional and BeO-based structure for ∇n amount of 0.007. In addition, the maximum achieved QF's are 3.65, 32.31 and 33.63RIU^{-1} for conventional, BeO-based SPR and proposed SPR sensors, respectively, at ∇n amounts of 0.007 of the urea samples. Greater RI, high penetration depth of SPW, and strong molecular absorption capability of upper layers, i.e., BeO and GaP, are the reasons for higher performance via the proposed structure.

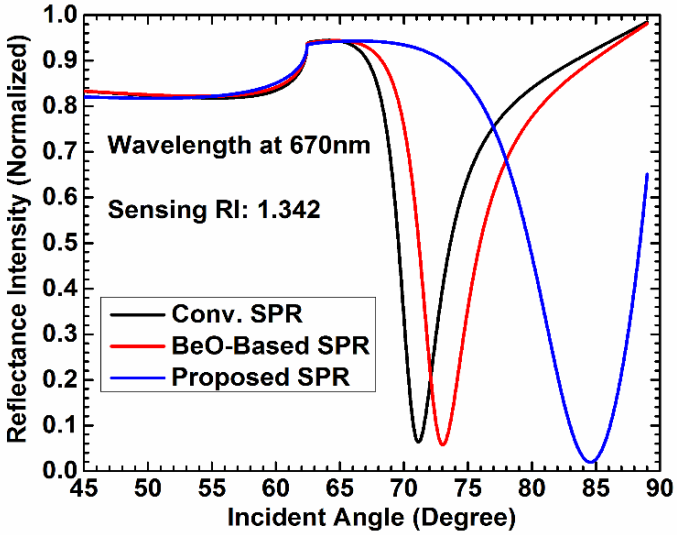

Fig. 6.11 Reflectance intensity vs angle at for sensing RI of 1.342.

Table 6.5 Performance parameters at different RIs of urea samples

SPR Structure Name	θ_{res}(°) for respective sensing RIs				S (°/RIU) for respective ∇n amounts			QF (RIU^{-1}) for respective ∇n amounts		
	1.335	1.337	1.339	1.342	∇n=0.002	∇n=0.004	∇n=0.007	∇n=0.002	∇n=0.004	∇n=0.007
Conv.	70.24	70.46	70.72	71.12	110	123	125.71	28.57	31.17	32.65
BeO-based	72.04	72.31	72.62	73.06	135	145	145.57	29.93	32.15	32.31
Proposed	82.53	83.10	83.67	84.55	285	285	288.57	33.22	33.22	33.63

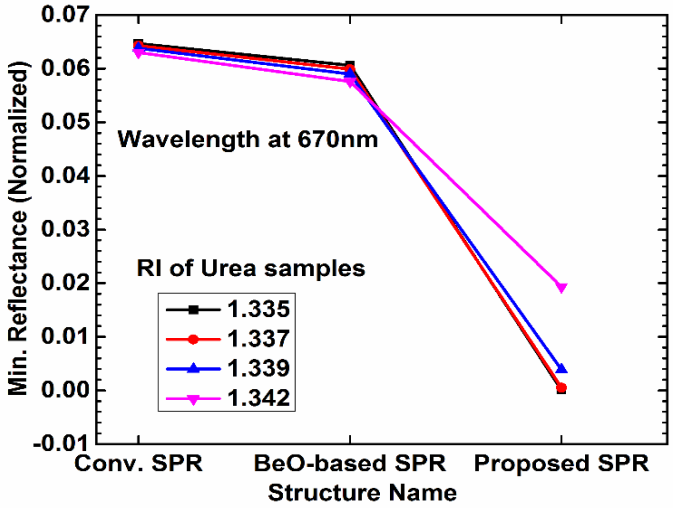

Fig. 6.12 Variations in the R_{min} vs different structures at different RIs of urea samples.

Moreover, Fig. (6.12) shows the R_{min} variations for structure to structure at different sensing RIs of 1.335, 1.337, 1.339 and 1.342. It can be clearly observed that better R_{min} performance is obtained for the proposed SPR structure compared to other structures. The less

R_{min} value signifies the maximum light energy transfer to the SPW, leading to high SPR performance.

Finally, Table 6.6 compares the performances of the proposed SPR structure and existing SPR structures. It demonstrates that the proposed SPR sensor has been achieved higher sensitivity of 288.57°/RIU, which is 1.25, 1.43 and 3.39 times higher that achieved by the existing sensors that are presented by the authors in [62], [64] and [63], respectively. In summary, the suggested SPR sensor provides a greater sensitivity and heightened the QF, making it more suited for SPR sensors to detect urea and therefore usable in the biomedical applications.

Table 6.6 Comparative Study on Proposed SPR with Existed SPR Sensors

References	SPR Structure	Sensitivity (°/RIU)	Quality Factor (RIU^{-1})
[63]	Prism-Chr-Au-Graphene-MoS_2-Sensing	85.05	-
[64]	Prism-Chr-Al_2O_3-MoS_2-Graphene-Sensing	202.02	-
[62]	Prism-Chr-Au-MoS_2-Graphene-Sensing	230	-
Proposed work	Prism-Au-BeO-GaP-Sensing	288.57	33.63

6.3.3 Performance Enhancement of SPR sensor for Urea Detection Using Au-Dielectric Materials Based structure

As shown in 6.13, the Au-dielectric materials structure-based proposed SPR biosensor is presented for this study. The structure has been made up on the basis of Kretschmann configuration, which is more preferable for practical implementation. This structure comprises of five layers, such as soda lime glass (SLG), Au, GeO_2, GaP and sensing medium. As first layer, SLG prism is used with the refractive index (RI) of 1.5031. Then, the second layer is comprised of Au, as plasmonic material, having RI of 0.13767+3.7917i and thickness of 45nm [179]. The third layer and fourth are comprised of GeO_2, GaP, as coated over the Au with the RIs of 1.6034 and 3.2791, and thicknesses of 5nm and 5nm, respectively. Finally, the fifth layer is comprised of sensing medium with RIs of 1.337 and 1.339 for 0.625 and 2.5 gm/dl, respectively, whereas the reference urea RI is 1.335 for analyzing SPR parameters [161].

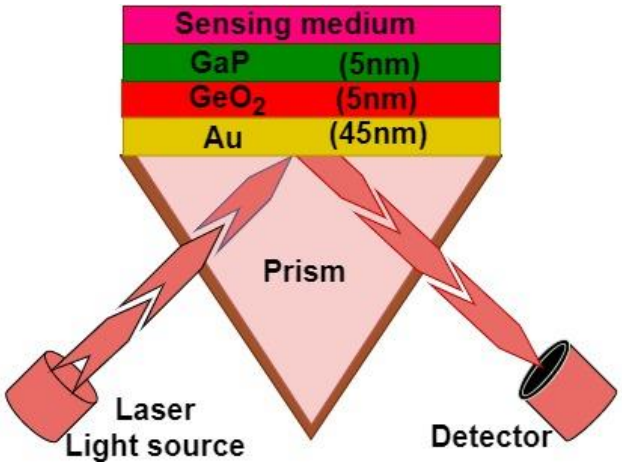

Fig. 6.13 The proposed SPR sensor for urea detection at 670nm wavelength.

The importance of implementing the proposed structure has been shown initially. The minimum reflectance of the sensor shows the maximum energy transfer to the SPW for higher performance. In order to show the optical performance of the proposed sensor, two other structures, such as conventional and GeO_2-based SPR, have been considered with defined layers. Fig. 6.14 shows the reflectance intensity response in terms of incident angle for sensing RI of 1.335, where black, red and blue colours represent the conventional and GeO_2-based and proposed SPR structures, respectively. The measured parameters, such as R_{min}, resonance angle (θ_{res}) and FWHM, for Fig. 6.14 have been mentioned in Table 6.7. It demonstrates that as number of layers are increasing in the structure, the resonance angle is shifted; it occurred because of the SPR phenomenon. The results have demonstrated that low R_{min} is accomplished for the proposed SPR sensor compared to other two structures due to low absorption loss. Because of the high damping effect and increasing number of layers, the proposed structure offers high FWHM [128]; still it has high absorption capability via GeO_2 and GaP.

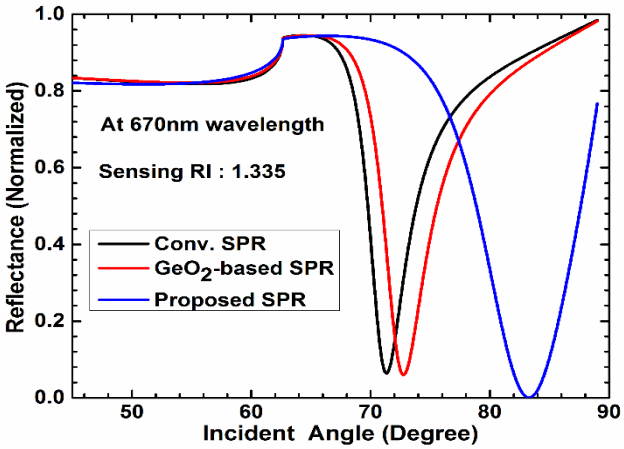

Fig. 6.14 SPR response vs incident angle for sensing RI of 1.335.

Table 6.7 Measured Parameters for Sensing RI of 1.335

Structure Name	R_{min}	θ_{res}	FWHM
Conv. SPR	0.0638	71.34	3.98
GeO_2-based SPR	0.0599	72.75	7.50
Proposed SPR	0.0007	83.27	8.38

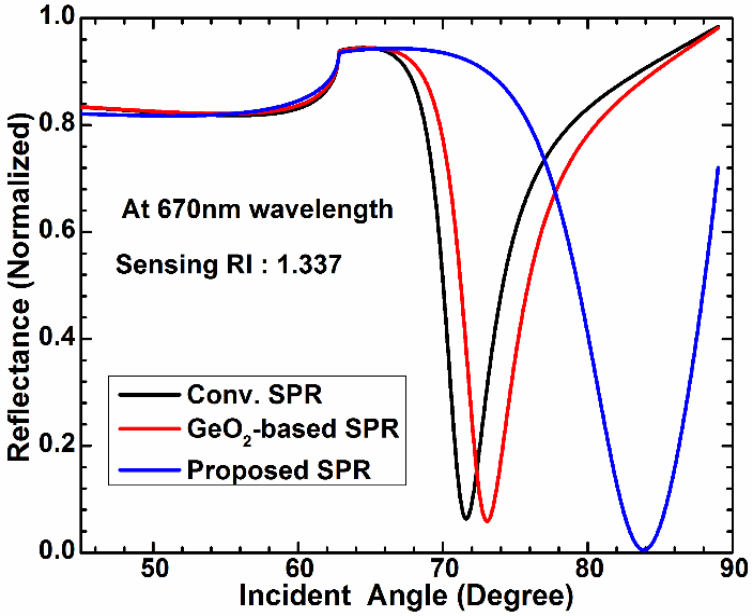

Fig. 6.15 SPR response vs incident angle for sensing RI of 1.337.

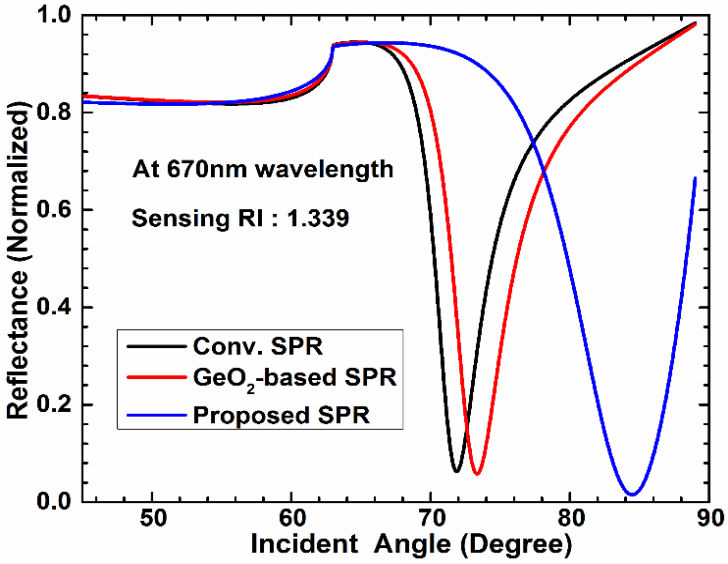

Fig. 6.16 SPR response vs incident angle for sensing RI of 1.339.

Table 6.8 Performance parameters at different RIs of urea samples

Structure Name	θ_{res}(°) for respective sensing RIs			S (°/RIU) for respective ∇n amounts		QF (RIU^{-1}) for respective ∇n amounts	
	1.335	1.337	1.339	∇n=0.002	∇n=0.004	∇n=0.002	∇n=0.004
Conv. SPR	71.34	71.60	71.87	130	132.5	32.66	33.29
GeO_2-based SPR	72.75	73.06	73.32	135	142.5	34.99	31.67
Proposed SPR	83.27	83.89	84.46	310	297.5	36.99	33.35

Furthermore, Fig. (6.15) and (6.16) are shown the reflectance intensity responses with respect to an incident angle for RIs of urea samples, such as 1.337 and 1.339, respectively. The SPR performance is investigated in terms of sensitivity and QF; and computed parameters for Fig. (6.15) and (6.16) have been mentioned in Table 6.8. The maximum achieved sensitivities are 130 and 132.5°/RIU for conventional SPR; 135 and 142.5°/RIU for GeO_2-based SPR; 310 and 297.5°/RIU for proposed SPR at ∇n amounts of 0.002 and 0.004 of urea samples, respectively. The proposed structure is accomplished higher sensitivity, which are 2.39 and 2.30 times higher at ∇n amounts of 0.002; 2.25 and 2.09 times higher at ∇n amounts of 0.004 than the conventional and GeO_2-based structures. Improved performance of proposed structure is obtained because of the higher RI, higher penetration depth of SPW and higher molecular absorption capability of the top layer, i.e., Gap. In addition, the proposed structure is provided QF of 36.99RIU^{-1} , which is better than other defined structures at ∇n amounts of 0.002.

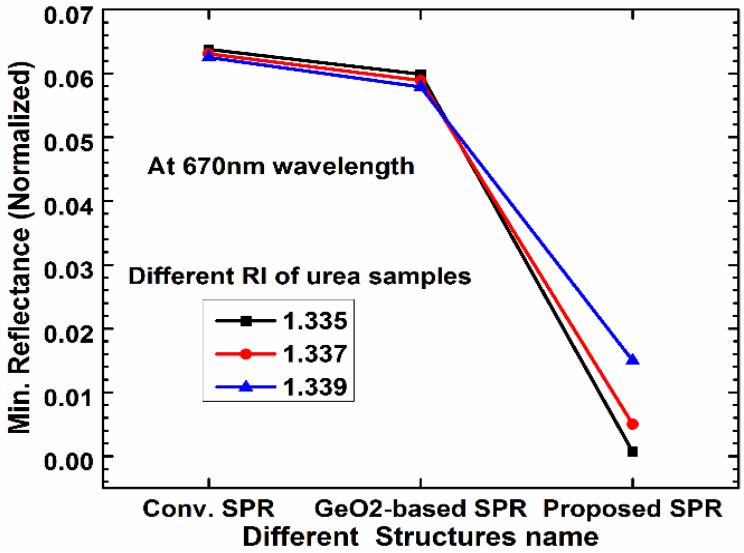

Fig. 6.17 Variations in R_{min} vs different RIs of urea samples for different structures.

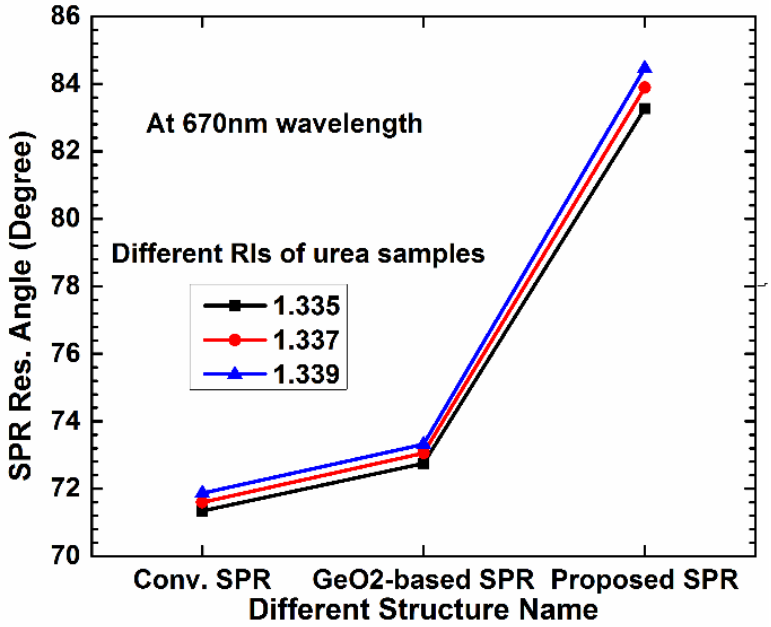

Fig. 6.18 Variations in $\nabla\theta_{ree}$ vs different RIs of urea samples for different structures.

Moreover, from Fig. (6.17) and (6.18), it can be clearly observed that the better performance of R_{min} and resonance angle shift have been exhibited by employing the proposed SPR structure. The resonance angle increases with the number of structure layers and sensing RI. Also, the sensitivity is significantly increased with proposed structure, and it offers more promising structure for urea detection at 670nm wavelength.

Table 6.9 presents the performance comparison of the proposed SPR structure with existing sensors, demonstrating the proposed SPR sensor offers superior performance in terms of sensitivity and QF; it is more suitable to detect the urea as well as applicable in the biomedical field.

Table 6.9 Performance Comparative Table

References	SPR Structure	Sensitivity (°/RIU)	Quality Factor (RIU^{-1})
[63]	Prism-Chr-Au-Graphene-MoS2-Sensing	85.05	-
[64]	Prism-Chr-Al_2O_3-MoS_2-Graphene-Sensing	202.02	-
[62]	Prism-Chr-Au-MoS_2-Graphene-Sensing	230	-
Proposed work	Prism-Au-GeO_2-GaP-Sensing	310	36.99

6.4 Conclusion

Three other SPR structures have been designed and analysed at the visible-infrared-red wavelength regions for urea detection by exploiting the transfer matrix method. Firstly, performance enhancement of SPR sensor has been shown employing MoS_2-Dielectric materials-MoS_2 structure. Secondly, the SPR sensor based on the Au-BeO-GaP structure has been presented. Thirdly, the SPR sensor employing an Au-dielectric material-based structure has been presented. In each event, the metal film thickness is optimized by plotting the reflectance curves with respect to an angle. Then, the impact of the proposed structure on the SPR sensor has been shown by comparing the proposed sensor performance with others. The proposed structures have been investigated in terms of sensitivity and QF. Finally, the comparative study has been demonstrated that the proposed sensors accomplish better SPR performance compared to the existing sensors that are being in available. Therefore, the proposed SPR structures are more suitable to detect the urea and can be gainfully employed in the biomedical field.

Chapter-7

High-performance fiber-optic-based SPR sensor for DNA hybridization using black phosphorus-tungsten disulfide hybrid structure

7.1 Introduction

The earlier works have been designed and analysed high-performance prism-based SPR sensor for different applications. The performances of those works are shown exceptional compared to the existing works. However, the prism-based SPR sensors are not attractive to the remote sensing applications in hazardous areas. On the other hand, the fiber optic based SPR sensors are highly preferred because they are robust, cost-effective, and compact and fast in response. Also, it has several advantages over the prism-based SPR including simple and flexible optical design, in-situ monitoring, and continuous analysis. Moreover, it is useful by the fact that the resonance feature can be easily tuned using a dielectric over-layer in the desired wavelength range.

Therefore, this chapter describes the modeling of high-performance fiber optic-based SPR sensor for DNA hybridization using a hybrid structure of black phosphorus and tungsten disulfide. This work shows the DNA hybridization sensing and the single nucleotide polymorphisms identifying procedure by observing the resonance shift and transmitter power performances for probe DNA, mismatched DNA and complementary DNA stands. Also, the performance parameters, such as sensitivity, depth-of-figure-of-merit (DFOM), quality-factor and detection-accuracy, are observed. Finally, this work shows a better SPR performance compared to the state-of-the-art works currently available.

7.2 Mathematical Equations

This section explains the methodology, mathematical expressions and design considerations for the proposed fiber optic-based SPR structure.

7.2.1 Transmitting power

The schematic diagram of the proposed fiber optic-based SPR sensor has been depicted in Fig. 7.1, which is comprised of Ag-BP-WS_2 structure, to sense the DNA hybridization. The first layer, the core of this optical fiber, has a diameter of D in order to realize this biosensor, and it is wrapped by a cladding with a flexible thickness. To create a sensing region L, the

middle part of the cladding is detached. The fiber's unclad part is coated with a sheet of Ag metal film, monolayer of BP and WS_2, which are regarded as the second, third and fourth layers, having a thickness of d_2, d_3 and d_4, respectively. The TM light mode of laser source, which excites the "surface plasmon poloritons (SPPs)' on the core-metal interface, launches into the one end of the fiber at the axial point with a wavelength of 633nm, and it receives at the other end of the fiber using a spectrometer or a computer. Assume the light source transmits with the power of P at an angle of θ, and dP is the arrived power at angel of dθ. Then, the mathematical expression for dP is shown in Eq. (7.1) [56, 106].

$$dP \propto P(\theta)d\theta \tag{7.1}$$

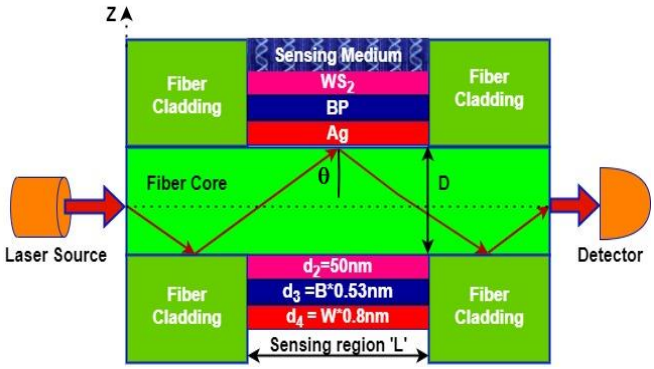

Fig. 7.1 The schematic diagram of the proposed optical fiber SPR biosensor.

Where, "P(θ) is the modal power proportional to the incident angle", and Eq. (7.2) shows its mathematical expression [106, 120].

$$P(\theta) = \frac{n_c^2 \sin\theta \cos\theta}{\left(1-n_c^2\cos^2\theta\right)^2} \tag{7.2}$$

Where, n_c is the RI (1.451) of the fiber core. Furthermore, Eq. (7.3) shows the normalized transmitted power of incident light for single reflection at the core-metal interface [120, 180].

$$P_{trans} = \frac{\int_{\theta_{cr}}^{\pi/2} R_p^{N_{ref}(\theta)} P(\theta) d\theta}{\int_{\theta_{cr}}^{\pi/2} P(\theta)\, d\theta} \tag{7.3}$$

Where, "$N_{ref}(\theta) = L/D\tan\theta$ is the total number of light reflections in the SPR fiber sensor, θ is the incident angle with the normal to the core metal layer interface in the sensing region, L is the length of sensing region, D is the diameter of the fiber core, and $\theta_{cr} = \sin^{-1}(n_{cl}/n_c)$ is the critical angle, whereas n_{cl} and n_c are refractive indexes of the cladding and core, respectively" [180, 181]. In this study, the reflectivity (R_p) of proposed sensor investigates for a five layered structure (fiber core/Ag/BP/WS_2/sensing medium) by considering the "angular interrogation technique". The refractive indexes of Ag, BP and WS_2

are 0.056206+4.2776i [138], 3.5+0.1i [138] and 4.9+0.3122i [145], and their thicknesses are 50nm, B×0.53nm and W×0.8nm [138, 127], respectively, where it can offer low absorption loss [182, 29]. Where, B and W are the number of BP and WS_2 layers, respectively. Finally, the sensing medium is used as fifth layer over WS_2 with an RI of 1.33 [180, 183].

7.2.2 Reflectivity

To compute the proposed sensor's reflectivity (R_p), the transfer matrix method (TMM) has been applied for N-layer modelling due to its efficiency as well as not mandatory any approximations. Here, it assumes the k^{th}-layer's thickness is d_k, which is measured along the $z-$axis, and ε_k denotes the k^{th} layer's dielectric constant. The tangential fields, which can evaluate by applying the boundary conditions, giving a relation between the initial conditions ($Z = Z_1 = 0$) and final conditions ($Z = Z_{N-1}$) as follows in Eq. (7.4) [182, 184]:

$$\begin{bmatrix} P_1 \\ Q_1 \end{bmatrix} = H \begin{bmatrix} P_{N-1} \\ Q_{N-1} \end{bmatrix} \tag{7.4}$$

Where, P_1 and Q_1 represent the tangential components of electrical and magnetic fields, respectively, at the first layer boundary, whereas P_{N-1} and Q_{N-1} are corresponding fields for the N^{th} layer boundary. Eq. (7.5) indicates the properties matrix of combined structure is obtained at resonance condition for SPR sensor (H_{ij}) using TM polarized incident light [180-183]. Moreover, Eq. (7.6) represents a description of the transverse RI (l_k), whereas Eq. (7.7) evaluates the arbitrary stage constant (β_k) for the k^{th} layer. Furthermore, Eq. (7.8) and (7.9) represent the wave impedance (z_k) and input angle (θ_k) for k^{th}layer. Where, λ is the wavelength of an incident light beam, n_c is the fiber core's RI, μ_k is the permeability of the k^{th} layer, k_x is the incident wave vector, and θ is the incident angle [138, 182, 185].

$$H_{ij} = \left[\prod_{K=2}^{N-1} \begin{pmatrix} \cos\beta_k & -i\sin\beta_k / \varepsilon_k \\ -i\varepsilon_k \sin\beta_k & \cos\beta_k \end{pmatrix} \right]_{if} = \begin{bmatrix} H_{11} & H_{12} \\ H_{21} & H_{22} \end{bmatrix} \tag{7.5}$$

Where,

$$l_k = \left[\frac{\mu_k}{\varepsilon_k} \right]^{1/2} \qquad \cos\theta_k = \sqrt{\frac{\varepsilon_k - (n_c \sin\theta)^2}{\varepsilon_k^2}} \tag{7.6}$$

And,

$$\beta_k = \frac{2\pi}{\lambda} l_k \cos\theta_k (z_k - z_{k-1}) = \frac{2\pi}{\lambda} d_k \sqrt{\varepsilon_k - (n_c \sin\theta)^2} \tag{7.7}$$

$$z_k = \frac{k_x l_k \cos\theta_k}{(2\pi c/\lambda_{633})\varepsilon_k^2} \tag{7.8}$$

$$\theta_k = \left(\cos\sqrt{1 - (l_{k-1}/l_k)(\sin\theta)^2} \right)^{-1} \tag{7.9}$$

Finally, the numerical expressions for Fresnel's R_p mode analysis to compute the reflection coefficient (r_p) as well as R_p of an incident light in the SPR response have been represented in Eq. (7.10) and (7.11), respectively [138, 182, 185].

$$r_p = \frac{(H_{11} + H_{12} l_N) - (H_{21} + H_{22} l_N)}{(H_{11} + H_{12} l_N) + (H_{21} + H_{22} l_N)} \tag{7.10}$$

$$R_P = \left| r_p \right|^2 \tag{7.11}$$

7.2.3 For computing performance parameter

The performance of SPR-based sensor is primarily measured in three parameters, such as sensitivity, quality factor (QF) and detection accuracy (DA). Sensitivity is defined as the ratio of change in SPR resonance angle ($\nabla\theta_{res}$) and change in the RI (∇n), and it is manifested as the sensor's sensing capabilities. QF is defined as the ratio of sensitivity and full-width-half-maxima (FWHM), where FWHM signifies the SPR curve's spectral width corresponds to 50% of maximum reflectivity. DA is defined as the ratio of $\nabla\theta_{res}$ to FWHM. In addition to the above mentioned parameters, this study analyzes the performance of dip of figure of merit (DFOM) in the fiber optic based SPR sensor for the first time, and this is defined as the ratio of sensitivity to minimum transmittance (T_{min}). The performances of QF, DA and DFOM demonstrate the quality, accuracy of the product and noise impact in a sensor, respectively. All the parameters should be as high as possible for a better optical fiber-based SPR sensor. The mathematical modelling for computing the performance sensitivity, QF, DA and DFOM have been represented in Eq. (7.12-7.15) [55, 57, 138, and 186].

$$S = \frac{\nabla \theta_{res}}{\nabla n} \qquad (^\circ / RIU) \tag{7.12}$$

$$QF = \frac{S}{FWHM} \qquad (RIU^{-1}) \tag{7.13}$$

$$DA = \frac{\nabla \theta_{res}}{FWHM} \tag{7.14}$$

$$DFOM = \frac{S}{T_{\min}} \tag{7.15}$$

7.2.4 Sensing RI

Due to the submersing of the probe DNA (P-DNA), the RI of the sensing medium changes in the sensor [10]. Eq. (7.16) shows the numerical modelling to measure the changed amount in the sensing medium's RI (n_s^a) after adsorption of the DNA molecule [12, 33].

$$\mathbf{n_s^a = n_s + c_a \frac{dn}{dc}} \tag{7.16}$$

Where, n_s is the sensing RI before the DNA adsorption, c_a is the concentration of adsorbed molecules, dn/dc is the RI increment after DNA molecule adsorption, and the increment value is $0.182 cm^3/gm$ for standard buffer solution [10-12]. Due to the inclusion of the probe DNA in the sensing medium, which affects the sensing RI, DNA molecules move the SPR resonance angle towards right. The number of carriers in the concentration of BP-WS_2 layer should be changed because the DNA is composed of electron-rich molecules that show a deviation in the propagation constant. Therefore, a high performing SPR sensor has been proposed for DNA hybridization detection based on changes in SP angle.

7.3 Simulation Results

7.3.1 DNA hybridization sensing

Initially, the performance shows the probe DNA hybridization sensing employing the proposed sensor, which is composed of a five layered schematic structure, fiber core-Ag-BP-WS_2-sensing region, that compound of probe DNA as well as Phosphate Buffered Saline (PBS) solution. Fig. 7.2 depicts the corresponding SPR curves for without (blue line) and with (red line) adding probe DNA. The results have shown the ambipolar behavior because of the changes in sensing RI that effects the resonance angle (θ_{res}) in the SPR curve. The obtained resonance angles are 77.17° and 79.39° for without (bare sensor) and with probe DNA, demonstrating the SPPs has a large resonance angle shift ($\nabla\theta_{res}$) of 2.22° towards right, which is desirable as well as easily detectable, due to the immobilization of the probe DNA on the BP-WS_2 monolayer surface.

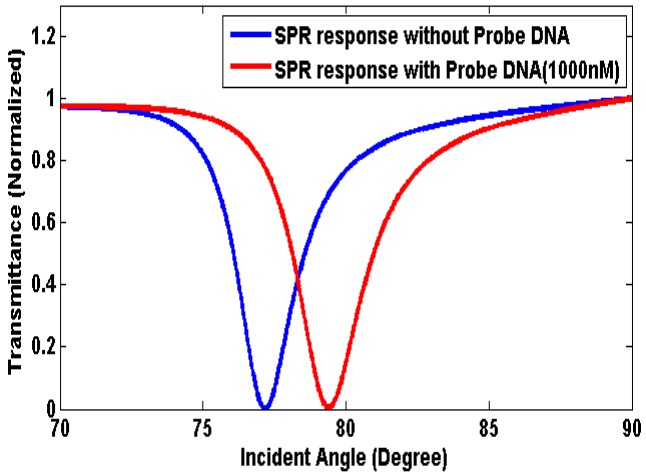

Fig. 7.2 SPR responses for with and without probe DNA comparison.

Furthermore, the performance shows the detection of mismatched DNA hybridization with probe DNA employing the proposed SPR sensor, which is a combination of PBS solution, probe DNA and mismatched DNA. Fig. 7.3 explores the corresponding SPR responses,

whereas blue, red and black lines are showing the responses for before composing probe DNA, after composing probe DNA and after composing mismatched DNA, respectively. The results reveal that the achieved resonance angles are 77.17, 79.39 and 79.65° for before composing probe DNA, after composing probe DNA and after composing mismatched DNA, respectively. The $\nabla\theta_{res}$ of 0.26◦ has been observed in the event of single mismatched DNA using the "non-complementary DNA target", showing no significant change in the resonance angle because of the immobilized probe and mismatched DNA pair. This can signify that no hydrogen bonding occurs between the probe and target DNA strands when the probe molecules are transported to the mismatched target [138, 180, 183]. Therefore, the target molecules' charges do not alter significantly.

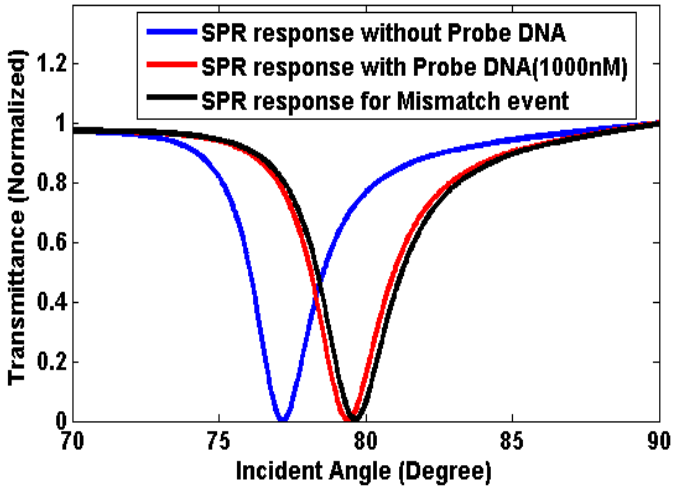

Fig. 7.3 Hybridization of probe DNA and mismatched DNA using proposed sensor.

Furthermore, the performance shows the complementary DNA hybridization sensing employing the proposed sensor. The attachment of two single-stranded complementary (ssDNA) forms the helix structure of double stranded DNA (dsDNA). In this event, one is probe and the other is target; this process is called the complementary DNA hybridization. The performance shows the sensor's analytical behavior in the process of target DNA and probe DNA, which are composed on the hybrid surface of BP-WS_2. This investigation also shows the distinctive characterization between the "single-based mismatched" and "complementary DNA" as well as SNP. The analytical data is demonstrated that θ_{res} plays a crucial role in the DNA hybridization sensing. Therefore, Fig. 7.4 depicts the transmittance power (T.P) in terms an angle for the proposed sensor at the different concentrations of complementary DNA, whereas each curve shows the specific DNA molecule. The obtained parameters of T.P and θ_{res} have been mentioned in Table 7.1 for various concentration of "complementary DNA" molecules. In order to achieve the typical value of DNA concentration where the resonance

angle is strongly influenced, the different DNA concentrations, such as 1001, 1010, 1100nM, are compared as a group in this study.

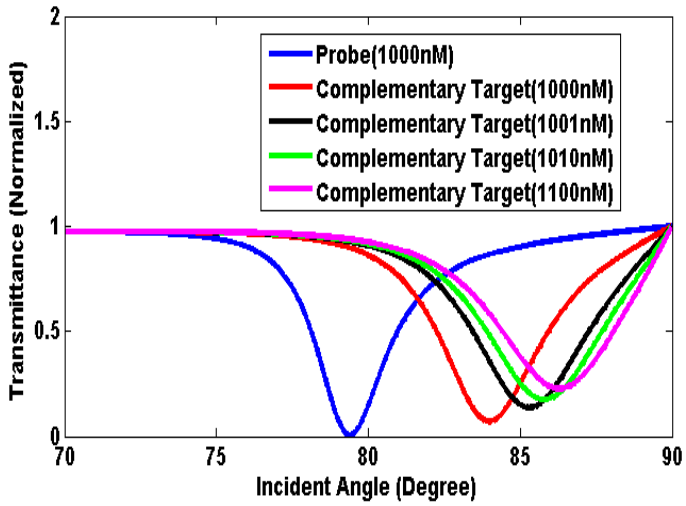

Fig. 7.4 Transmittance curves for probe DNA and complementary DNA target.

A considerable improvement of θ_{res} shows a sign for DNA hybridization with the matching combination of probe and complementary target (C.T.). Table 7.1 has been witnessed the SPR angle is strongly influenced by the concentration increment, having a predictable impact on the T.P-incidence angle features of the SPR device, which manifests the higher sensitivity and resonance shift towards the target DNA hybridization. Moreover, the variations in $\nabla T.P_{min}^{probe}$ and $\nabla\theta_{res}^{probe}$, which are measured by Eq. (7.17) and (7.18), have been reported in Table 7.1 and found the minimum values of $\nabla T.P_{min}^{probe}$ (i.e., $\left(\nabla \mathrm{T.P_{min}^{probe}}\right)_{\mathrm{min}}$), and $\nabla\theta_{res}^{probe}$ (i.e., $\left(\nabla\theta_{\mathrm{res}}^{\mathrm{probe}}\right)_{\mathrm{min}}$) have been achieved at the C.T concentration of 1000nM, but they are different in the remaining events. Finally, Table 7.2 displays the various conditions and their obtained results or decision on the DNA hybridization. Therefore, from Table 7.2, it can be noticed that the proposed sensor has been successfully detected the DNA hybridization at different concentrations of DNA target molecules, and it has also been also mentioned when the SNP is occurred.

$$\nabla T.P_{min}^{probe} = \left|T.P_{min}^{probe} - T.P_{min}^{Target-nM}\right| \quad (7.17)$$

$$\nabla\theta_{res}^{probe} = \left|\theta_{res}^{probe} - \theta_{res}^{Target-nM}\right| \quad (7.18)$$

$\left(\nabla T.P_{min}^{probe}\right)_{min} = \left|T.P_{min}^{probe} - T.P_{min}^{Target-1000nM}\right|$ = |0.004722-0.07117|= 0.066418

$\left(\nabla\theta_{res}^{probe}\right)_{min} = \left|\theta_{res}^{probe} - \theta_{res}^{Target-1000nM}\right|$ = |79.39-83.97|= 4.58deg

Table 7.1. Measured Parameters of (T.P) and θ_{res} for Fig. 4

Concentration (c_a) [nM]	T.P	θ_{res} (°)	$\nabla T.P_{min}^{probe}$	$\nabla\theta_{res}^{probe}$ (°)
1000 (Probe)	0.004722	79.39	-	-
1000 (C.T.)	0.07117	83.97	0.066418	4.58
1001 (C.T.)	0.1364	85.30	0.131678	5.91
1010 (C.T.)	0.1742	85.80	0.169478	6.41
1100 (C.T.)	0.2264	86.28	0.221678	6.89

Table 7.2. Different Conditions for Decision Making for hybridization

Condition	Obtain Result/Decision
$\nabla T.P_{min}^{probe} \geq \left(\nabla T.P_{min}^{probe}\right)_{min}$ && $\nabla\theta_{res}^{probe} \geq \left(\nabla\theta_{res}^{probe}\right)_{min}$	Hybridization is happened
$\nabla T.P_{min}^{probe} \leq \left(\nabla T.P_{min}^{probe}\right)_{min}$ && $\nabla\theta_{res}^{probe} \geq \left(\nabla\theta_{res}^{probe}\right)_{min}$	Try again
$\nabla T.P_{min}^{probe} \geq \left(\nabla T.P_{min}^{probe}\right)_{min}$ && $\nabla\theta_{res}^{probe} \leq \left(\nabla\theta_{res}^{probe}\right)_{min}$	Try again
$\nabla T.P_{min}^{probe} \leq \left(\nabla T.P_{min}^{probe}\right)_{min}$ && $\nabla\theta_{res}^{probe} \leq \left(\nabla\theta_{res}^{probe}\right)_{min}$	SNP is happened

7.3.2 Performance analysis of the proposed sensor

Since the angular interrogation method is easy to implement in real time applications, the proposed fiber optic based SPR sensor has been considered this method in order to analyze the performance. In this event, the proposed sensor considered the fiber core diameter (D), sensing region (L), Ag, BP and WS_2 thicknesses (d_2, d_3 and d_4) as 50µm 5mm, 50nm, 0.53nm and 0.8nm, respectively, because they offer low absorption loss. Beyond those thicknesses, the sensor makes it absorbent that leads to high damping or attenuation in the SPR response [138, 180-184]. It signifies a low SPR performance that symbolizes the reduced transmitted energy and higher reflected energy to the surface plasmon wave (SPW), which is produced by the oscillations of SPPs at the fiber core-metal interface [138, 145]. Fig. 7.5 shows the transmittance responses in terms of an angle for different sensing refractive indexes (1.33 to 1.36 with an interval of 0.01). Where, blue, red, black and magenta lines are represented for the sensing RI of 1.33, 134, 1.35 and 1.36, respectively. The obtained resonance angles (θ_{res})

are 77.17, 79.39, 82.17 and 86.30° and found that the θ_{res} increases as the sensing RI increases, indicating that the SPR detection property is fulfilled, as stated in the literature. In Fig. 7.5, the relationship between θ_{res} and RI is non-linear due to high changes in the sensing RI that make changes in the SPW. Therefore, from Fig. 7.5, this study has considered the ∇n of 0.03 refractive index units (RIU) where the maximum resonance shift is achieved compared to ∇n of 0.01 and 0.002RIU. In optical biosensing, the RIU is utilised for evanescent wave sensors (optical waveguides, ring resonators, interferometers and SPR). It can also be used to indicate amounts that change as the RI changes. It's the smallest detectable change in the RI of the surface where the evanescent wave is travelling. The abbreviation RIU is sometimes used to indicate that a number refers to a RI. Therefore, ∇n of 0.03RIU is used for further analysis of the proposed fiber optic-based SPR sensor.

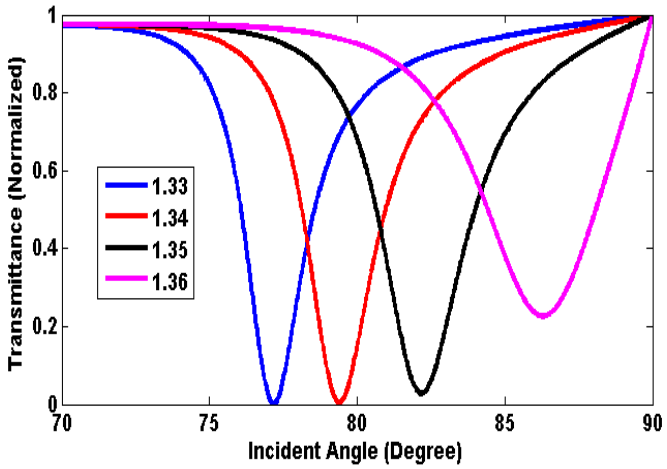

Fig. 7.5 Transmittance vs angle for proposed sensor at different sensing RI.

Furthermore, the study shows performance analysis of the proposed sensor in terms of sensitivity, DA, QF and DFOM for different layer combinations of BP-WS_2 hybrid surface. In this event, the proposed sensor is considered the D of 50µm, L of 5mm, d_2 of 50nm, d_3 of B×0.53nm and d_4 of W×0.8nm, whereas B and W are signifying the number of BP and WS_2 layers, respectively. Fig. 7.6 depicts the transmitted responses for five distinct combinations of BP and WS_2 layer numbers, such as (0 and 0), (1 and 0), (2 and 0), (3 and 0), and (4 and 0). (1 and 1), in order to observe the influence of monolayer BP-WS_2 structure in the proposed sensor. The blue color line signifies the B=0 and W=0, red color line signifies the B=1 and W=0, black color line signifies the B=2 and W=0, magenta color line signifies the B=3 and W=0, and green color line signifies the B=1 and W=1.

The obtained results of FWHM, T.P, and the corresponding θ_{res} and $\nabla\theta_{res}$ have been mentioned in Table 7.3, whereas the sensing RI of 1.33 and ∇n of 0.03RIU. From Table 7.3, it

can be observed that θ_{res} increases after adding hybrid structure of BP-WS_2 and offers a better T.P performance rather than conventional structure and only BP-based structure (fiber core-Ag-BP-sensing). The achieved minimum T.P's are 0.0514 at θ_{res} of 74.56° for conventional sensor, 0.0340 at θ_{res} of 75.25° for monolayer BP, 0.0197 at θ_{res} of 76.03° for only bilayer BP, 0.0089 at θ_{res} of 76.89 for only three-layer BP, and 0.0004 at θ_{res} of 77.17° for monolayer of BP and WS_2 hybrid structure.

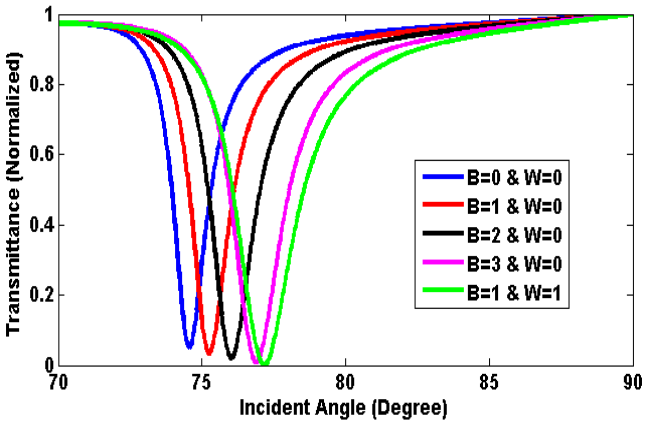

Fig. 7.6 Transmittance vs angle for proposed sensor at different BP-WS_2 layers.

The corresponding resonance angle shifts have been also mentioned in Table 7.3, showing the significant improvement in the hybrid structure of BP and WS_2. Therefore, the sensor performance parameters of sensitivity, DA, QF and DFOM have been computed by applying Eq. (7.12-7.15), and obtained parameters have been reported in Table 7.4. The achieved sensitivities are 208.33, 226.67, 252.00, 293.00 and 304.33°/RIU for the conventional, monolayer BP, bilayer BP, three-layer BP and hybrid structure of BP-WS_2-based (proposed structure) sensors, respectively. Similarly, the accomplished DFOM are 4053.11, 6666.76, 12791.88, 32921.35, and 760825.00 for conventional, monolayer BP, bilayer BP, three-layer BP and hybrid structure of BP-WS_2-based sensors, respectively. The graphical representation of sensitivity and DFOM have been shown in Fig. 7.7; The proposed structure has been accomplished the significant performance of sensitivity and DFOM compared to other sensors because of the exceptional properties of BRE materials, such as the absorption ability of biomolecules of BP and high fluorescence quenching ability of WS_2. Because of the expanded layer of biosensors, DA and QF are reduced slightly in the proposed structure due to high damping effect that leads to high FWHM. Although the DA and QF are reduced slightly, they are still suitable for the detection of DNA hybridization, whereas sensitivity and DFOM are the most important requirements.

Table 7.3 Measured Parameters for Fig. 6

BP (B) & WS_2 (W) layers	T. P_{min}	θ_{res} (°)	FWHM	$\nabla\theta_{res}$ for ∇n of 0.03
B=0 & W=0	0.0514	74.56	1.37	6.25
B=1 & W=0	0.0340	75.25	1.58	6.80
B=2 & W=0	0.0197	76.03	1.82	7.56
B=3 & W=0	0.0089	76.89	2.10	8.79
B=1 & W=1	0.0004	77.17	2.50	9.13

Table 7.4 Measured Parameters of S, DFOM, QF and DA for Fig. 6

BP (B) & WS_2 (W) layers	S (°/RIU)	DFOM	QF (RIU^{-1})	DA
B=0 & W=0	208.33	4053.11	152.07	4.56
B=1 & W=0	226.67	6666.76	143.46	4.30
B=2 & W=0	252.00	12791.88	138.46	4.15
B=3 & W=0	293.00	32921.35	139.52	4.19
B=1 & W=1	304.33	760825.00	121.73	3.65

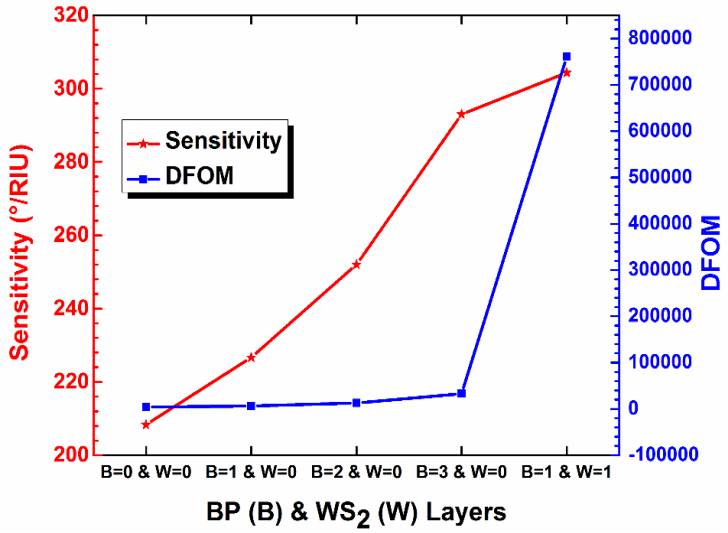

Fig. 7.7 Variations in the performances of S and DFOM vs the BP and WS_2 layers.

7.3.3 Comparative study of performance analysis

Finally, the performance of the proposed work has been compared with the existing works, as shown in Table 7.5; it can be observed that the proposed sensor is shown a significant sensitivity of 303.43°/RIU, QF of 121.73RIU^{-1} and DA of 3.65, which are manifested as the better performances compared to others. In addition, this study has analyzed the accuracy parameter of DFOM of 760825, which is existed in the DNA sensing for the first time. In

summary, the proposed fiber optic-based SPR sensor heightens the performance in terms of sensitivity, QF and DA, compared to the existing works, and presents the DFOM performance that shows the resonance depth effect for the first time in DNA hybridization sensing.

Table 7.5. Performance Comparison of Proposed Work with Existed Work

References	Coupling	Structure	S (°/RIU)	QF (RIU^{-1})	DA	DFOM
[186]	Prism	Ag-MoS_2-graphene	130	17.02	1.30	-
[55]	Prism	Au-BP-graphene	125	1.62	0.95	-
[187]	Prism	Au-WS_2-graphene	95.71	25.19	1.76	-
[57]	Prism	Cr-Au-BP-WSe_2	186.11	18.61	0.10	-
[180]	Fiber optic	Ag-MoS_2-graphene	105.71	23.23	1.63	-
[188]	Prism	Au-MoS_2-graphene	130	17.02	1.37	
[189]	Prism	Al-Si-BP-graphene	202.37	-	-	-
[190]	Prism	Ag-Ti-$MoSe_2$-graphene	215.50	-	-	-
Proposed work	Fiber optic	Ag-BP-WS_2	304.33	121.73	3.65	7,60,825

7.4 Conclusion

A highly performed fiber optic-based SPR sensor using a hybrid structure of BP-WS_2 to detect the DNA hybridization has been presented. The proposed structure has been comprised of five layers, such as fiber core, Ag, BP, WS_2 and sensing medium. For the hybridization of probe DNA, mismatched DNA and complementary DNA stands, the resonance shift and transmitter power performances have been shown by considering the angular interrogation technique. The proposed sensor successfully detected the DNA hybridization and shown the SNP procedure, according to the findings. Moreover, the influence of hybrid structure of BP-WS_2 in the proposed SPR sensor has been observed. For the proposed sensor, the maximum accomplished sensitivity and DFOM performances are 304.33°/RIU and 760825, respectively, which are 1.46 and 187.71 times higher than the conventional sensor (without hybrid structure). The highly improved performance of the proposed sensor has been attributed to the exceptional properties of 2D materials, such as the absorption ability of biomolecules of BP and high fluorescence quenching ability of WS_2. In addition, the acceptable performances of QF of 121.73RIU^{-1} and DA of 3.65 have been also observed for the proposed

sensor. A comparative study has been carried out at the end. It has been witnessed that the proposed structure has improved the sensitivity, QF and DA performances compared to the existing works, and presented DFOM performance for the first time. Therefore, the proposed fiber optic-based SPR sensor can be used as a high-performance carrier for DNA hybridization sensing and establishes a new platform in the biomedical and biological fields.

Chapter-8

Conclusions and Future Scope

8.1 Conclusions

The thesis presents numerical analysis of high-performance SPR based optical sensor for biomedical applications, such as urea detection, bacteria detection and DNA hybridization. The high-performance SPR sensors are analysed employing several novel SPR structures employing different combinations of metal films, dielectric materials and promising 2D materials. Numerical modeling of the presented SPR sensors is investigated by exploiting the angular interrogation method, wavelength region method and FDTD solution tool. The SPR sensor performances are considered in terms of sensitivity, quality factor, detection accuracy, figure of merit, dip-figure-of-merit and combined sensitivity factor. The details of the major achievements of the thesis works are summarized as follows.

- The performance enhancement of the SPR sensor has been presented for deoxyribonucleic acid hybridization employing black phosphorus, silver and silicon configurations. Thicknesses of structure layers are obtained by plotting reflectance curve using the transfer matrix method. The SPR performances are analyzed in terms of sensitivity, detection accuracy, quality factor and figure of merit. Results show that the combination of silver and black phosphorus provides better sensitivity as 91.54°/RIU, which is 1.26 times greater than conventional and graphene-based SPR sensors. However, the performance of detection accuracy and quality factor are degraded for the combination of silver and black phosphorus structure. The degraded parameters are improved of 8.53 and 11.04 times higher compared to conventional and graphene-based SPR sensor, respectively, with the inclusion of a silicon layer between the silver and black phosphorus. Moreover, it introduces the performance of figure of merit for the first time. Finally, the comparative study is carried out and observed that the proposed sensor provides better performance compared to existing sensors.
- Numerical analysis of a novel SPR sensor has been presented for Pseudomonas bacterial detection employing a silicon-barium titanate structure. In this work, three bacterial attachments of Pseudomonas over the affinity layer have been constituted, such as toluene, nicotine, and trifluoroethyl methacrylate. Initially, thicknesses of structure layers are obtained by plotting reflectance curves with respect to an angle. To show the impact of silicon in the proposed structure, three different structures are considered with comprised layers. The SPR performances are analyzed in terms of sensitivity, quality factor and figure of merit.

Results demonstrate that the proposed SPR sensor structure has been achieved the maximum performance parameters, such as sensitivity of 370°/RIU, quality factor of 86.65RIU^{-1} and figure of merit of 86.43 for Pseudomonas of trifluoroethyl methacrylate. It shows the improved the sensitivity performance after adding silicon to the structure. In addition, the proposed sensor is accomplished a magnified quality factor and figure of merit performances. Finally, the comparative study is carried out and demonstrated that the proposed sensor heightens performances in terms of sensitivity and FOM.

- A better performance of SPR biosensor has been presented by employing novel hybrid structures in this work. The work is categorized into two parts. In the first part, the numerical analysis of SPR biosensor based on Bismuth Ferrite-Bromide materials-BP/Graphene hybrid structure is presented using the transfer matrix method. This study initially observes the impact of 2D and bromide materials in the proposed structure. Results show that the BP-based structure provides better SPR performance than the graphene-based structure. The performance parameters, such as sensitivity of 468deg/RIU, QF of 87.80RIU^{-1}, FOM of 87.79 and DA of 0.44, have been achieved for the thallium bromide-black phosphorus-based SPR structure, which are 1.32, 1.46, 1.51, 1.47 times higher than the respective performances of the thallium bromide-graphene-based structure. Being inspired by the properties of thallium bromide and black phosphorus, another SPR biosensor is designed employing aluminum arsenide, thallium bromide and black phosphorus in the second part. Three other structures have been considered for the performance comparison. Results show that the sensitivity of the proposed structure is 4.52, 3.96, 3.06 times higher than that of structure-I, II, III, respectively. Moreover, the proposed sensor provides acceptable quality factor and figure of merit performances. In addition, this study introduces the performance parameter as the combined sensitivity factor for the first time. Finally, the high-performance of the proposed sensor is validated with the wavelength variation method by plotting reflectance curves at different wavelengths as well as by electric field intensity curves using the FDTD solution tool.
- A high performed SPR sensor has been presented for urea detection employing three different dielectric and 2D materials-based structures at different wavelength regions in this work. Firstly, performance enhancement of SPR sensor has been shown employing MoS_2-Dielectric materials-MoS_2 structure. The maximum achieved SPR performances are sensitivity of 280°/RIU and QF of 41.36RIU^{-1}. Secondly, the SPR sensor based on the Au-BeO-GaP structure has been presented. The maximum sensitivity of 288.57°/RIU, which is

2.29 and 1.98 times higher compared to the conventional and BeO-based structure. Thirdly, the SPR sensor employing an Au-dielectric material-based structure is presented. The proposed structure is accomplished higher sensitivity of 297.5°/RIU, which is 2.25 and 2.09 times higher than the conventional and GeO_2-based structures. In each work, the metal film thickness is optimized by plotting the reflectance curves. Finally, the comparative study is carried out and demonstrated that the proposed sensors are accomplished better SPR performance compared to the existing sensors.

- A high-performance fiber optic-based SPR sensor has been presented using a hybrid structure of black phosphorus and tungsten disulfide. This study shows the DNA hybridization sensing and the single nucleotide polymorphisms identifying procedure by observing the resonance shift and transmitter power performances for probe DNA, mismatched DNA and complementary DNA stands. Moreover, the performance parameters are investigated in terms of sensitivity, depth-of-figure-of-merit, quality factor and detection accuracy. Results show a significant sensitivity of 303.43°/RIU, quality factor of 121.73RIU^{-1} and detection accuracy of 3.65 for the proposed sensor, and these are manifested as the better performances compared to the existing sensors. In addition, this study has been analyzed the accuracy parameter as DFOM of 760825 for the first time with respect to DNA sensing.

8.2 Future Scope

Although the thesis presents enhanced performance in terms of sensitivity, quality factor, detection accuracy, figure of merit, dip of figure of merit and combined sensitivity factor, of the prism-based and fiber optic-based SPR sensors, some of the suggestions for the future works are as follows:

- In chapter-3, a combination of Ag, Si and BP provides better performance compared to the existing works for DNA hybridization. However, the sensor performance can be improved further by exploiting the wavelength interrogation method with the transfer matrix method as well as finite element method.
- In chapter-4, the Si-$BaTiO_3$ based structure overcomes the problem of Si that reduces the sensitivity of the sensor. It also gives better performance over all other existing sensors for bacterial detection. However, simultaneous improvement of sensitivity, detection accuracy and quality factor with single SPR structure could be a great challenge for the future work. These developments might include image processing technology, which will have an

influence on future SPR imaging trends, whether in real time (video) or non-real time (image).

- In chapter-5, a novel SPR sensor is designed with high performance employing novel hybrid structures. However, the sensor performance still be improved employing emerging can dielectric and TDMC materials, which provide high absorption capability. Moreover, wide-area, robust and dependable light source technology are required to allow high-quality sensing in the hardware implementation. As an alternative to this feature need, it needs the development of organic light sources in the future.
- In chapter-6, high-performance prism-based SPR sensor is proposed for urea detection at different wavelength regions. However, the high-performance proposed sensors can be developed at infrared wavelengths in future, where the sensor offers high light-transmission.
- In chapter-7, the numerical modelling of high-performance fiber optic based SPR sensor has been proposed with BP and WS_2based structure for DNA hybridization. However, the high-cost platforms and components are the key difficulties of SPR sensor research and development. Typically, commercial platforms do not match the financial needs of small research groups or points of care to invest and maintain. As a result, it might serve as a future blueprint for academic and industrial scientists and engineers to design a low-cost, high-performance SPR sensor platform.

Bibliography

1. B. Liedberg, C. Nylander, I. Lunstrom, Surface plasmon resonance for gas detection and biosensing, Sens. Actuators. B 4 (1983) 299–304.
2. R. W. Wood, On a remarkable case of uneven distribution of light in a diffraction grating spectrum, Phys. Soc. 18(1) (1902) 269.
3. J. Zenneck, Uber die FortpflanzungebenerelektromagnetischerWellenlangseinerebenenLeiterflache und ihreBeziehungzurdrahtlosenTelegraphie,Annalen der Physik, 328(10) (1907) 846-866.
4. A. Sommerfeld, Propagation of Waves in Wireless Telegraphy, Annals der Physik, 28 (1909) 665-736.
5. R. H. Ritchie, Plasma losses by fast electrons in thin films, Phys. Rev. 106 (1957) 874-881.
6. C. J. Powell, J. B. Swan, Effect of oxidation on the characteristic loss spectra of aluminum and magnesium, Phys. Rev. 118 (1960) 640-643.
7. E. A. Stern, R. A. Ferrell, Surface plasma oscillations of a degenerate electron gas, Phys. Rev. 120 (1960) 130-136.
8. A. Otto, Excitation of nonradiative surface plasma waves in silver by the method of frustrated total reflection, Zeit. Phys., 216(4) (1968) 398-410.
9. E. Kretschmann, H. Reather, Radiative decay of non-radiative surface plasmons excited by light, Zeit.Natur. 23(12) (1968) 2135-2136.
10. X.D. Hoa, A. G. Kirk, M. Tabrizian, Towards integrated and sensitive surface plasmon resonance biosensors: a review of recent progress, Biosensors and bioelectronics, 23(2) (2007) 151-60.
11. J. Homola, S. S. Yee, G. Gauglitz, Surface plasmon resonance sensors: Review, Sens. Actuators B, 54(1-2)(1999) 3-15.
12. R. Ince, R. Narayanaswamy, Analysis of the performance of interferometry, surface plasmon resonance, and luminescence as biosensors and chemosensors, Analy.Chim. Acta 569(1-2) (2006) 1-20.
13. O. S. Wolfbeis, Fiber-optic chemical sensors and biosensors, Analy. Chem. 78(12) (2006) 3859-3873.
14. V. Yesudasu, H.S. Pradhan, and R.J. Pandya, "Recent progress in surface plasmon resonance based sensors: A comprehensive review," Heliyon **7**(2), 06321 (2021).

15. R. H. Ritchie, Plasma losses by fast electrons in thin films, Phys. Rev. 106(5) (1957) 874-881.
16. C. J. Powell, J. B. Swan, Effect of oxidation on the characteristic loss spectra of aluminum and magnesium, Phys. Rev. 118(3) (1960) 640-643.
17. A. Otto, Excitation of nonradiative surface plasma waves in silver by the method of frustrated total refection, Zeit. Phys. 216(4) (1968) 398-410.
18. A. K. Sharma, R. Jha, B. D. Gupta, Fiber-optic sensors based on surface plasmon resonance: a comprehensive review, J. IEEE Sens. 7(8) (2007) 1118-1129.
19. Rademann, Jörg, and Günther Jung. "Integrating combinatorial synthesis and bioassays." *Science* 287.5460 (2000): 1947-1948.
20. Steinhauer, Cornelia, et al. "Biocompatibility of surfaces for antibody microarrays: design of macroporous silicon substrates." *Analytical biochemistry* 341.2 (2005): 204-213..
21. Albers, Willem M., and Inger Vikholm-Lundin. "Surface plasmon resonance on nanoscale organic films." Nano-Bio-Sensing. Springer, New York, NY, 2011. 83-125.
22. Kurihara, Kazuyoshi, and Koji Suzuki. "Theoretical understanding of an absorption-based surface plasmon resonance sensor based on Kretchmann's theory." Analytical Chemistry 74.3 (2002): 696-70.
23. David, Catalina, et al. "SERS detection of biomolecules using lithographed nanoparticles towards a reproducible SERS biosensor." Nanotechnology 21.47 (2010): 475501.
24. Roos, Håkan, et al. "Thermodynamic analysis of protein interactions with biosensor technology." Journal of Molecular Recognition: An Interdisciplinary Journal 11.1-6 (1998): 204-210.
25. Çavdar, Seda. Mycobacterium tuberculosis bakterisinin rifampine karşı geliştirdiği direnç mutasyonlarının elektrokimyasal DNA biyosensörü ile saptanması. Diss. Ege Üniversitesi, 2008.
26. Çavdar, Seda. "Mycobacterium tuberculosis bakterisinin rifampine karşı geliştirdiği direnç mutasyonlarının elektrokimyasal DNA biyosensörü ile saptanması." PhD diss., Ege Üniversitesi, 2008.
27. McLaughlin, J. A. D. "Point of Care Biomedical Sensors." Studies in health technology and informatics 117 (2005): 25.
28. Wassaf, Dina, et al. "High-throughput affinity ranking of antibodies using surface plasmon resonance microarrays." Analytical biochemistry 351.2 (2006): 241-253.
29. Abe, Masato, Jandro Abot, Günther Achs, Jason Agius, A. Emin Aktan, John C. Aldrin, Bashir Ali et al. "Encyclopedia of structural health monitoring." (2009).

30. Y. K. Prajapati, A. Yadav, A. Verma,V.Singh, Effect of metamaterial layer on optical surface plasmon resonance sensor, J. Light Elec. Opt. 124(18) (2013) 3607-3610.
31. S. Pal, Y. K. Prajapati, J. P. Saini, V. Singh, Resolution enhancement of optical surface plasmon resonance sensor using metamaterial, Photonic Sens. 5(4) (2015) 330-338.
32. J. B. Maurya, Y. K. Prajapati, A comparative study of different metal and prism in the surface plasmon resonance biosensor having MoS_2-graphene, Opt. Quant. Elec. 48(5) (2016) 280.
33. S. Pal, A. Varma, Y. K. Prajapati, J. P. Saini, Influence of black phosphorous on performance of surface plasmon resonance biosensor, Opt. Quant. Elec. 49(12) (2017) 403.
34. M. S. Rahman, M. S. Anower, M. R. Hasan, M. B. Hossain, M. I. Haque, Design and numerical analysis of highly sensitive Au-MoS_2-graphene based hybrid surface plasmon resonance biosensor, Opt. Commun. 396, (2017) 36-43.
35. J. B. Maurya, Y. K. Prajapati, V. Singh, J. P. Saini, R. Tripathi, Improved performance of the surface plasmon resonance biosensor based on graphene or MoS_2 using silicon, Opt. Commun. 359 (2016), 426-434.
36. J. B. Maurya, Y. K. Prajapati, V. Singh, J. P. Saini, R. Tripathi, Performance of graphene–MoS 2 based surface plasmon resonance sensor using silicon layer, Opt. Quant. Elec. 47(11) (2015) 3599-3611.
37. J. B. Maurya, Y. K. Prajapati. Influence of dielectric coating on performance of surface plasmon resonance sensor, Plasmonics 12(4) (2017) 1121-1130.
38. S. Pal, Y. K. Prajapati, J. P. Saini, V. Singh, Sensitivity enhancement of metamaterial-based surface plasmon resonance biosensor for near infrared, Opt. Appl. 46(1)2016.
39. M. B. Hossain, M. Hassan, L. F. Abdulrazak, M. M. Rana, M. M. Islam, M. S. Rahman, Graphene-MoS_2-Au-TiO_2-SiO_2 hybrid SPR biosensor for formalin detection: numerical analysis and development, Adv. Mater. Lett. 10(9) (2019) 656-662.
40. Y. Xiang, J. Zhu, L. Wu, Q. You, B. Ruan, and X. Dai, Highly sensitive terahertz gas sensor based on surface plasmon resonance with graphene, J. IEEE Photonics 10(1) (2017) 1-7.
41. L. Oliveira, A. Herbster, C. da Silva Moreira, F. H. Neff, A. M. N. Lima, Surface plasmon resonance sensing characteristics of thin aluminum films in aqueous solution, J. IEEE Sensors 17(19) (2017) 6258-6267.
42. Aksimsek, Sinan, Zhipei Sun, Graphene-MoS_2heterostructure based surface plasmon resonance biosensor, EMTS IEEE, (2016).
43. J. N. Nur, F. Asrafy, K. N. Shushama. Highly Sensitive Surface Plasmon Resonance Biosensor Using WSe_2 and Silicon, iCEEiCT IEEE, (2018).

44. M. M. Bari, A. K. Sarkar, S. Hossain, Sensitivity analysis of a graphene based surface plasmon resonance biosensor in terms of number of graphene layers, ICECTE IEEE, (2016).
45. H. Vahed, C. Nadri, Sensitivity enhancement of SPR optical biosensor based on Graphene-MoS_2 structure with nanocomposite layer, Opt. Mater. 88, (2019) 161-166.
46. M. S. Islam, A. Z. Kouzani, E. D. Coyle, Theoretical analysis of the propagation of surface plasmon waves in multilayer surface plasmon resonance biosensor, PIERS IEEE (2017).
47. S. Pal, A. Verma, J. P. Saini, Y. K. Prajapati, Sensitivity enhancement using silicon-black phosphorus-TDMC coated surface plasmon resonance biosensor, IET Optoelectronics 13(4) (2019) 196-201.
48. R. Boruah, D. Mohanta, A. Choudhury, P. Nath, G. A. Ahmed, Surface plasmon resonance-based protein bio-sensing using a Kretschmann configured double prism arrangement, J. IEEE Sensors 15(12) (2015) 6791-6796.
49. G. Lan, Y. Gao, Surface plasmon resonance sensor with high sensitivity and wide dynamic range, IEEE Sens. 18(13) (2018) 5329-5333.
50. A. A. Michelson, F. G. Pease, F. Pearson, Repetition of the Michelson-Morley experiment, JOSA, 18(3) (1929) 181-182.
51. S. K. Raghuwanshi, M. Kumar, Highly dispersion tailored property of novel class of multimode surface plasmon resonance biosensor assisted by teflon and metamaterial layers, IEEE Trans. Instr. Meas. (2018).
52. C. A. De Souza Filho, A. M. Lima, F. H. Neff, Modeling and Temperature Drift Compensation Method for Surface Plasmon Resonance-Based Sensors, IEEE Sens. 17(19) (2017) 6246-6257 (2017).
53. S. Scarano, S. Mariani, and M. Minunni, SPR-based affinity biosensors as innovative analytical devices, J. LightwaveTechn. 33(16) (2015) 3374-3384.
54. V. M. Faca, K. S. Song, H. Wang, Q. Zhang, A. L. Krasnoselsky, L. F. Newcomb, R. R. Plentz, S. Gurumurthy, M. S. Redston, S. J. Pitteri, S. R. Pereira-Faca, A mouse to human search for plasma proteome changes associated with pancreatic tumor development, *PLoS medicine* 5(6) (2008).
55. S. Pal, A. Verma, S. Raikwar, Y. K. Prajapati, J. P. Saini, Detection of DNA hybridization using graphene-coated black phosphorus surface plasmon resonance sensor, Appl. Phys. A 124(5) (2018) 394.

56. M. S. Rahman, M. R. Hasan, K. A. Rikta, M. S. Anower, A novel graphene coated surface plasmon resonance biosensor with tungsten disulfide (WS_2) for sensing DNA hybridization, Opt. Mater. 75, (2018) 567-573.
57. B. Meshginqalam, J. Barvestani, Performance enhancement of SPR biosensor based on phosphorene and transition metal dichalcogenides for sensing DNA hybridization, IEEE Sens. 18(18) (2018) 7537-7543.
58. Y. Vasimalla, H. Pradhan, R. Pandya, "SPR performance enhancement for DNA hybridization employing Black Phosporous, Silver and Silicon," Appl. Opt. 59(24) (2020) 7299-7307.
59. S. Ahmed, S. Kabir, Copper-Germanium-Graphene Based Highly Sensitive Plasmonic Biosensor For Protein Detection, IC4ME2 IEEE, (2018).
60. W. Wu, A. Katsnelson, O. G. Memis, H. Mohseni, A deep sub-wavelength process for the formation of highly uniform arrays of nanoholes and nanopillars, Nanotechn.18(48) (2007) 485302.
61. F. Said, P. S. Menon, M. N. Nawi, A. R. Zain, A. Jalar, B. Y. Majlis, Copper-graphene SPR-based biosensor for urea detection, ICSE IEEE (2016).
62. N. A. Jamil, P.S. Menon, F. A. Said, K. A. Tarumaraja, G. S. Mei, B.Y. Majlis, Graphene-based surface plasmon resonance urea biosensor using Kretschmann configuration, RSM IEEE (2017).
63. N. A. Jamil,N. B. Khairulazdan, P. S. Menon, A. R. Zain, A. A. Hamzah, B. Y. Majlis, Graphene-MoS_2 SPR-based biosensor for urea detection, ISESD IEEE (2018).
64. N. A. Jamil, P. S. Menon, G. S. Mei, S. Shaari, B. Y. Majlis, Urea biosensor utilizing graphene-MoS_2 and Kretschmann-based SPR, IEEE (2017).
65. P. S. Mead, L. Slutsker, V. Dietz, L. F. McCaig, J. S. Bresee, C. Shapiro, P. M. Griffin, R. V. Tauxe, Food-related illness and death in the United States, Emerging infectious diseases 5(5) (1999) 607.
66. J. B. Maurya, Y. K. Prajapati, R. Tripathi, Effect of molybdenum disulfide layer on surface plasmon resonance biosensor for the detection of bacteria, Silicon 10(2)(2018) 245-256.
67. J. P. Nataro, and J. B. Kaper, "Diarrheageniceschericia coli. Clinical microbiology reviews," 11(1), 142-201 (1998).
68. S. Kumbhat, R. Gehlot, K. Sharma, U. Singh, V. Joshi, Surface plasmon resonance based indirect immunoassay for detection of 17β-estradiol, J. Phar. Biom. Anal. 163 (2019) 211-216.

69. J. K. Seifert, D. L. Morris, World survey on the complications of hepatic and prostate cryotherapy, J. Surgery, 23(2) (1999) 109-114.
70. H. D. Butala, A. Ramakrishnan, A. Sadana, A mathematical analysis using fractals for binding interactions of estrogen receptors to different ligands on biosensor surfaces, Sens. Act. B Chem. 88(3) (2003) 266-280.
71. E. Wozei, S. W. Hermanowicz, H. N. Holman, Developing a biosensor for estrogens in water samples: Study of the real-time response of live cells of the estrogen-sensitive yeast strain RMY/ER-ERE using fluorescence microscopy,Biosens. Bioelect. 21(8) (2006) 1654-1658.
72. M. Mahmoudpour, J. E. Dolatabadi, M. Torbati, A. Homayouni-Rad, Nanomaterials based surface plasmon resonance signal enhancement for detection of environmental pollutions,Biosens. Bioelect. 127 (2019) 72-84.
73. D. Michel, F. Xiao, L. Skillman, K. Alameh, Surface plasmon resonance sensor for in situ detection of xanthan gum, J. IEEE Quant. Elect. 22(3) (2015) 379-382.
74. J. Homola, R. Slavik, Fibre-optic sensor based on surface plasmon resonance, Elect. Lett. 32(5) (1996) 480.
75. M. S. Islam, C. M. Cordeiro, J. Sultana, R. A. Aoni, S. Feng, R. Ahmed, M. Dorraki, A. Dinovitser, B. W. Ng, D. Abbott, A Hi-Bi Ultra-Sensitive Surface Plasmon Resonance Fiber Sensor, IEEE Access 7 (2019) 79085-79094.
76. F. Wang, C. Liu, Z. Sun, T. Sun, B. Liu, P. K. Chu, A highly sensitive SPR sensors based on two parallel PCFs for low refractive index detection, IEEE Photonics 10(4) (2018) 1-10.
77. Z. Zhang, F. Chu, Z. Guo, J. Fan, G. Li, W. Cheng, Design and Optimization of Surface Plasmon Resonance Sensor Based on Polymer-Tipped Optical Fiber, J. LightwaveTechn. 37(11) (2019) 2820-2827.
78. N. Polley, S. Basak, R. Hass,C. Pacholski, Fiber optic plasmonic sensors: Providing sensitive biosensor platforms with minimal lab equipment,Biosens. Bioelect. 132 (2019) 368-374.
79. H. Qian, Y. Huang, X. Duan, X. Wei, Y. Fan, D. Gan, S. Yue, W. Cheng, T. Chen, Fiber optic surface plasmon resonance biosensor for detection of PDGF-BB in serum based on self-assembled aptamer and antifouling peptide monolayer, Biosens. Bioelect. 140 (2019) 111350.

80. K. Ravi, B. D. Gupta, Fiber-Optic SPR Based Acetylcholine Biosensor Using Enzyme Functionalized Ta_2O_5Nanoflakes for Alzheimer's Disease Diagnosis, J. LightwaveTechn. 36(18) (2018) 4018-4024.
81. V. Semwal, B. D. Gupta, Highly sensitive surface plasmon resonance based fiber optic pH sensor utilizing rGO-Pani nanocomposite prepared by in situ method, Sens. Actuators B Chem. 283 (2019) 632-642.
82. W. Qi, J. Y. Jing, B. T. Wang, Highly Sensitive SPR Biosensor Based on Graphene Oxide and Staphylococcal Protein A Co-Modified TFBG for Human IgG Detection, IEEE Transactions Inst. Meas. (2018).
83. F. Zha, J. Li, P. Sun, H. Ma, Highly sensitive selectively coated D-shape photonic crystal fibers for surface plasmon resonance sensing, Phys. Lett. A 383(15) (2019) 1825-1830.
84. Q. Liu, Y. Liu, H. Yuan, F. Wang, W. Peng, A smartphone-based red-green dual color fiber optic surface plasmon resonance sensor, IEEE Photonics Techn. Lett. 30(10) (2018) 927-930.
85. H. Fu, S. Zhang, H. Chen, J. Weng, Graphene enhances the sensitivity of fiber-optic surface plasmon resonance biosensor, J. IEEE Sens. 15(10) (2015) 5478-5482.
86. Z. Fan, Surface plasmon resonance refractive index sensor based on photonic crystal fiber covering nano-ring gold film, Opt. Fiber Techn. 50, (2019) 194-199.
87. A. Aray, H. SaghafifarM. Soltanolkotabi, Calculation of Dispersion Relation and Single Mode Operation in Surface Plasmon Resonance Based Fiber Optic Refractive Index Sensors, J. LightwaveTechn. 34(11) (2016) 2782-2788.
88. N. Cennamo, L. Coelho, D. F. Santos, J. M. Baptista, A. Guerreiro, P. A. Jorge, Modal Filtering for Optimized Surface Plasmon Resonance Sensing in Multimode Plastic Optical Fibers, IEEE Sens. 15(11) (2015) 6306-6312.
89. N. Luan, J. Yao, Refractive Index and Temperature Sensing Based on Surface Plasmon Resonance and Directional Resonance Coupling in a PCF, IEEE Photonics 9(2) (2017) 1-7.
90. L. Peng, G. Zhou, M. Li, Z. Hou, C. Xia, S. Ge, Surface Plasmon Resonance Sensor Based onMicrostructured Optical Fiber with Ring-Core Configuration, IEEE Photonics 8(5) (2016) 1-11.
91. M. Li, L. Peng, G. Zhou, B. Li, Z. Hou, C. Xia, Design of Photonic Crystal Fiber Filter With Narrow Width and Single-Polarization Based on Surface Plasmon Resonance, IEEE Photonics 9(3) (2017) 1-8.

92. L. C. C. Coelho, J. M. M. M. de Almeida, H. Moayyed, J. L. Santos,D. Viegas, Multiplexing of Surface Plasmon Resonance Sensing Devices on Etched Single-Mode Fiber, J. LightwaveTechn. 3(2) (2015)432-438.
93. N. Luan, J. Yao, Surface Plasmon Resonance Sensor Based On Exposed-Core Microstructured Optical Fiber Placed With A Silver Wire, IEEE Photonics 8(1), (2016) 1-8.
94. N. Luan, J. Yao, High Refractive Index Surface Plasmon Resonance Sensor Based on a Silver Wire Filled Hollow Fiber, IEEE Photonics 8(1) (2016) 1-9.
95. N. Jing, J. Zhou, K. Li, Z. Wang, J. Zheng, P. Xue, Refractive Index Sensing Based on a Side-Polished Macrobend Plastic Optical Fiber Combining Surface Plasmon Resonance and Macrobending Loss, IEEE Sens. 19(14) (2019) 5665-5669.
96. S. K. Mishra, S. Bhardwaj and B. D. Gupta, Surface Plasmon Resonance-Based Fiber Optic Sensor for the Detection of Low Concentrations of Ammonia Gas, IEEE Sens. 15(2) (2015) 1235-1239.
97. J. Homola, "Present and future of surface plasmon resonance biosensors," Anal Bioa. Chem. 377(3), 528-539 (2003).
98. W. M. Mukhtar, S. Shaari, A. A. Ehsan, and P. S. Menon, "Electro-optics interaction imaging in active plasmonic devices," Opt. Mater. Express **4**(3), 424-433 (2014).
99. F. A. Said, P. S. Menon, T. Kalaivani, M. A. Mohamed, A. Abedini, S. Shaari, B. Y. Majlis, and V. Retnasamy, "FDTD analysis of structured metallic nanohole films for LSPR-based biosensor," IEEE RSM 1-4 (2015).
100. H. Fu, S. Zhang, H. Chen, and J. Weng, "Graphene enhances the sensitivity of fiber optic surface plasmon resonance biosensor," IEEE Sens. **15**(10), 5478-5482 (2015).
101. J. Zhu, B. Ruan, Q. You, J. Guo, X. Dai, and Y. Xiang, "Terahertz imaging sensor based on the strong coupling of surface plasmon polaritons between PVDF and graphene," Sens. Actuators B Chem. **264**, 398-403 (2018).
102. L. Wu, J. Guo, H. Xu, X. Dai, and Y. Xiang, "Ultrasensitive biosensors based on long-range surface plasmon polariton and dielectric waveguide modes," Photonics Research **4**(6), 262-266 (2016).
103. A.Sinibaldi, N. Danz, E. Descrovi, P. Munzert, U. Schulz, F. Sonntag, L. Dominici, and F. Michelotti, "Direct comparison of the performance of Bloch surface wave and surface plasmon polariton sensors," Sens. Actuator B Chem. **174**, 292-298 (2012).

104. B. Ruan, Q. You, J. Zhu, L. Wu, J. Guo, X. Dai, and Y. Xiang, "Improving the performance of an SPR biosensor using long-range surface plasmon of Ga-doped zinc oxide," Sensors **18**(7), 2098 (2018).

105. A. K. Mishra, S. K. Mishra, and R. K. Verma, "Graphene and beyond graphene MoS_2: a new window in surface-plasmon-resonance-based fiber optic sensing," J. Phys. Chem. C **120**(5), 2893-2900 (2016).

106. L. E. Ronald, "Multiwavelength Surface Plasmon Resonance Sensor Designs for Chemical and Biochemical Detection," P.H.D. thesis, Dept. of Chemistry, Virginia Polytechnic Institute and State University, Ontario, Canada, 2013.

107. E. Klantsataya, A. François, H. Ebendorff-Heidepriem, P. Hoffmann, andT. M. Monro, "Surface plasmon scattering in exposed core optical fiber for enhanced resolution refractive index sensing," Sensors **15**(10), 25090-25102 (2015).

108. A. Verma, A. Prakash, and R. Tripathi, "Sensitivity enhancement of surface plasmon resonance biosensor using graphene and air gap," Opt. Commun. **357**, 106-112 (2015).

109. M. Biednov, T. Lebedeva, and P. Shpilovuy, "Gold and Aluminum based surface Plasmon resonance biosensors: sensitivity enhancement," Opt. Sens. 9506, 95061P, (2015).

110. A. K. Mishra, S. K. Mishra, and R. K. Verma, "Graphene and beyond graphene MoS_2: a new window in surface-plasmon-resonance-based fiber optic sensing," J. Phys. Chem. C **120**(5), 2893-2900 (2016).

111. M. Pumera, "Graphene in biosensing," Mater. Today **14**(7-8), 308-315, (2011).

112. L. Wu, H. S. Chu, W. S. Koh, and E. P. Li, "Highly sensitive graphene biosensors based on surface plasmon resonance," Opt. Express **18**(14), 14395-14400 (2010).

113. X. SX, X. Zhai, Y. Huang, J. Q. Liu, L. L. Wang, andS. C. Wen, "Graphene surface plasmons with dielectric metasurfaces," J. Lightwave Technol. **35**(20), 4553-4558 (2017).

114. S. Y. Cho, Y. Lee, H. J. Koh, H. Jung, J. S. Kim, H. W. Yoo, J. Kim, and H. T. Jung, "Superior chemical sensing performance of black phosphorus: comparison with MoS_2 and graphene," Adv. Mater. **28(**32), 7020-7028 (2016).

115. N. Mao, J. Tang, L. Xie, J. Wu, B. Han, J. Lin, S. Deng, W. Ji, H. Xu, K. Liu, and L. Tong, "Optical anisotropy of black phosphorus in the visible regime," J. Am. Chem. Soc. **138** (1), 300-305 (2016).

116. L. Wu, J. Guo, Q. Wang, S. Lu, X. Dai, Y. Xiang, and D. Fan, "Sensitivity enhancement by using few-layer black phosphorus-graphene/ TMDCs heterostructure in surface plasmon resonance biochemical sensor," Sens. Actuators B Chem. **249**, 542-548 (2017).

117. A. Verma, A. Prakash, and R. Tripathi, “Performance analysis of graphene-based surface plasmon resonance biosensors for detection of Pseudomonas-like bacteria,” Opt. Quant. Elect. **47**(5), 1197-1205 (2015).

118. K. M. McPeak, S. V. Jayanti, S. J. Kress, S. Meyer, S. Iotti, A. Rossinelli, and D. J. Norris, “Plasmonic films can easily be better: rules and recipes," ACS photonics **2**(3), 326-333 (2015).

119. H. Karimi, R. Yusof, R. Rahmani, H. Hosseinpour, and M. T. Ahmadi, “Development of solution-gated graphene transistor model for biosensors,” Nano Lett. **9**(1), 1-11 (2014).

120. L. Diéguez, N. Darwish, M. Mir, E. Martínez, M. Moreno, and J. Samitier, “Effect of the refractive index of buffer solutions in evanescent optical biosensors,” Sens. Lett. **7**(5), 851-855 (2009).

121. L. J. Wang, G. Cao, T. Tu, H. O. Li, C. Zhou, X. J. Hao, Z. Su, G. C. Guo, H. W. Jiang, and G. P. Guo, “A graphene quantum dot with a single electron transistor as an integrated charge sensor,” Appl. Phys. **97**(26), 262113 (2010).

122. V. Ball, and J. J. Ramsden, “Buffer dependence of refractive index increments of protein solutions,” Inc. Biopoly. **46**(7), 489-492 (1998).

123. C. Fang, Y. Liu, G. Han, Y. Shao, Y. Huang, J. Zhang, and Y. Hao, “Absorption Enhancement for Black Phosphorus Active Layer Based on Plasmonic Nanocavity,” IEEE Photonics **10**(1), 1-10 (2018).

124. Q. Ouyang, S. Zeng, L. Jiang, L. Hong, G. Xu, X. Q. Dinh, J. Qian, S. He, J. Qu, P. Coquet, and K. T. Yong, “Sensitivity enhancement of transition metal dichalcogenides/silicon nanostructure-based surface plasmon resonance biosensor,” Scientific reports. 6, 28190 (2016).

125. H. Riveros-Rosas, A. Julián-Sánchez, G. Moreno-Hagelsieb, and R. A. Muñoz-Clares, “Aldehyde dehydrogenase diversity in bacteria of the Pseudomonas genus,” Chem. Bio. Interactions **304**, 83-87 (2019).

126. Z. Hossain, “Bacteria:Pseudomonas,” Enc. Food Safe. **1**, 490– 500 (2014).

127. T. Liu, J. Hou, and Y. Peng, “Effect of a newly isolated native bacteria, Pseudomonas sp. NP22 on desulfurization of the lowrank lignite,” J. Mineral Proc. **162**, 6–11 (2017).

128. N. Mudgal, P. Yupapin, J. Ali, and G. Singh, “$BaTiO_3$-Graphene-Affinity Layer–Based Surface Plasmon Resonance (SPR) Biosensor for Pseudomonas Bacterial Detection,” Plasmonics **15**(5), 1-9 (2020).

129. J.B. Maurya, Y.K. Prajapati, S. Raikwar, and J.P. Saini, “A silicon-black phosphorous based surface plasmon resonance sensor for the detection of NO2 gas,” Optik **160**, 428–33 (2018).

130. J. Hamola, “Surface plasmon resonance sensors for detection of chemical and biological species,” Chem. Rev. **108**(2), 462–93 (2008).

131. A.S. Kushwaha, A. Kumar, R. Kumar, M. Srivastava, and S.K. Srivastava, "Zinc oxide, gold and graphene-based surface plasmon resonance (SPR) biosensor for detection of Pseudomonas like bacteria: a comparative study," Optik **172**, 697–707 (2018).

132. A. Verma, A. Prakash, and R. Tripathi, "Sensitivity improvement of graphene based surface plasmon resonance biosensors with chaclogenide prism," Optik **127**(4), 1787–1791 (2016).

133. A. Verma, A. Prakash, and R. Tripathi, "Performance analysis of graphene based surface plasmon resonance biosensors for detection of Pseudomonas-like bacteria," Opt. Quant. Elect. **47**(5), 1197–1205 (2015).

134. J. Homola, "Surface plasmon resonance based sensors," Chem. Sen. Biosen. **4,** 45–67 (2006).

135. S. Saini, I. S. Ahuja, V. S. Sharma, "Residual stresses, surface roughness, and tool wear in hard turning: a comprehensive review," Materials and Manufacturing Processes. 27(6), 583-598 (2012).

136. A.K. Sharma, and A.K. Pandey, "Blue phosphorene/MoS_2 heterostructure based SPR sensor with enhanced sensitivity," IEEE Phot. Techn. Lett. **30(**7), 595–598 (2018).

137. A. Lahav, M. Auslender, I. Abdulhalim, "Sensitivity enhancement of the guided wave surface-plasmon resonance sensors," Opt. Lett. **33**(21), 2539–2541 (2008).

138. V. Yesudasu, H.S. Pradhan, and R.J. Pandya, "SPR performance enhancement for DNA hybridization employing black phosphorus, silver, and silicon," Appl. Opt. **59**(24), 7299-7307 (2020).

139. Kumar, A.S. Kushwaha, M. Srivastava, H. Mishra, and S.K. Srivastava, "Enhancement in sensitivity of graphene-based zinc oxide assisted bimetallic surface plasmon resonance (SPR) biosensor," Appl. Phys. A Mater. Sci. Proc. **124**(3), 235 (2018).

140. L. Liu, M. Wang, L. Jiao, T. Wu, F. Xia, M. Liu, W. Kong, L. Dong, and M. Yun, "Sensitivity enhancement of a graphene– barium titanate based surface plasmon resonance biosensor with an Ag– au bimetallic structure in the visible region," Opt. Soc. Ame. B **36**, 1108–1116 (2019).

141. P. Sun,M. Wang, L. Liu, L. Jiao, W. Du, F. Xia, M. Liu, W. Kong, L. Dong, and M. Yun, "Sensitivity enhancement of surface plasmon resonance biosensor based on graphene and barium titanate layers," Appl. Surf. Sci. **475**, 342–347 (2019).

142. Z. Lin, L. Jiang, L. Wu, J. Guo, X. Dai, Y. Xiang, and D. Fan, "Tuning and sensitivity enhancement of surface plasmon resonance biosensor with graphene covered Au-MoS_2-Au films, " IEEE Phot. Jour. **8**(6), 1–8 (2016).

143. P.B. Johnson, and R.W. Christy, "Optical constants of the noble metals," Phys. Rev. B **6**(12), 4370–4379 (1972).

144. P.K. Maharana, T. Srivastava, R. Jha, "On the performance of highly sensitive and accurate graphene-on-aluminum and silicon-based SPR biosensor for visible and near infrared," Plasm. **9**(5), 1113–1120 (2014).

145. B. D. Gupta, and A. K. Sharma, "Sensitivity evaluation of a multi-layered surface plasmon resonance-based fiber optic sensor: a theoretical study," Sens. Actuators B **107**, 40–46 (2005).

146. S.H. Wemple, J.M. Didomenico, and I. Camlibel, "Dielectric and optical properties of melt-grown $BaTiO_3$," Phys. Chem. Sol. Jour. **29**(10), 1797–1803 (1968).

147. K.N. Shushama, M.M. Rana, R. Inum, and M.B. Hossain, "Sensitivity enhancement of graphene coated surface plasmon resonance biosensor," Opt. Quant. Ele. **49**(11), 381 (2017).

148. M.S. Rahman, M.S. Anower, M.K. Rahman, M.R. Hasan, M.B. Hossain, and M.I. Haque, "Modeling of highly sensitive MoS_2-graphene hybrid based fiber optic SPR biosensor for sensing DNA hybridization," Opt. **140**, 989–997 (2017).

149. M.B. Hossain, M.M. Islam, L.F. Abdulrazak, M.M. Rana, T.B.A. Akib, and M Hassan, "Graphene coated optical fiber SPR biosensor for BRCA1 and BRCA2 breast cancer biomarker detection: a numerical design-based analysis," Phot. Sens. **10**(2), 1–13 (2019).

150. M.S. Rahman, M.S. Anower, M.R. Hasan, M.B. Hossain, and M.I. Haque, "Design and numerical analysis of highly sensitive Au-MoS_2 graphene based hybrid surface plasmon resonance biosensor," Opt. Comm. **396**, 36–43 (2017).

151. T.M. Davis, and W.D. Wilson, "Determination of the refractive index increments of small molecules for correction of surface plasmon resonance," Data. Ana. Biochem. **284**(2), 348-353 (2000).

152. M.B. Hossain, and M.M. Rana, "DNA hybridization detection based on resonance frequency readout in graphene on Au SPR biosensor," J. Sens. (2016).

153. S. Pal, A. Verma, Y.K. Prajapati, and J.P. Saini, "Figure of Merit Enhancement of Surface Plasmon Resonance Biosensor Using Ga-Doped Zinc Oxide in Near Infrared Range," Phot. Sens. **10**(4), 340-352 (2020).

154. Kumar, R., Pal, S., Pal, N., Mishra, V., and Prajapati, Y. K., High-performance bimetallic surface plasmon resonance biochemical sensor using a black phosphorus-MXene hybrid structure, Appl. Phys. A 127, 259 (2021).

155. Wu, L., Jia, Y., Jiang, L., Guo, J., Dai, X., Xiang, Y., and Fan, D., Sensitivity improved SPR biosensor based on the MoS2/graphene–aluminum hybrid structure. J. Lightw. Techno. 35(1), 82-87 (2016).

156. Dhibi, A., Hakami, J., and Abassi, A., Performance analysis of surface plasmon resonance sensors using bimetallic alloy--bimetallic alloy and perovskite-bimetallic alloy-perovskite nanostructures, Phys. Scr. 96, 065505 (2021).

157. Jha, R., and Sharma, A. K., Chalcogenide glass prism based SPR sensor with Ag-Au bimetallic nanoparticle alloy in infrared wavelength region. J. Opt. A-Pure Appl. Op., 11(11), 45502-45508 (2009).

158. S. H. Choi, Y. L. Kim, and K. M. Byun, Graphene-on-silver substrates for sensitive surface plasmon resonance imaging biosensors, Opt. Exp., 19(2) (2011) 458-66.

159. Wu, L., Guo, J., Wang, Q., Lu, S., Dai, X., Xiang, Y., and Fan, D., Sensitivity enhancement by using few-layer black phosphorus-graphene/TMDCs heterostructure in surface plasmon resonance biochemical sensor. Sens. Actuators B Chem. 249, 542-548 (2017).

160. Mukhtar, W. M., Halim, R. M., Dasuki, K. A., Rashid, A. R., and Taib, N. A., Silver-Graphene Oxide Nanocomposite Film-based SPR Sensor for Detection of Pb 2+ Ions. IEEE (ICSE), 152-155 (2018).

161. Polyanskiy, M., RefractiveIndex. INFO-Refractive index database, Ref. Ind. INFO. (2018).

162. Maharana, P. K., Jha, R., and Palei, S., Sensitivity enhancement by air mediated graphene multilayer based surface plasmon resonance biosensor for near infrared. Sens. Actuators B, Chem., 190(1), 494-501 (2014).

163. Pozo, A. M., Pérez-Ocón, F., and Rabaza, O., A continuous liquid level sensor for fuel tanks based on surface plasmon resonance. Sensors 16(5), 724 (2016).

164. Vibisha, G. A., Jeeban K. N., Maheswari, P., Priyadharsini, N., Nisha, A., Jaroszewicz, Z., Rajesh, K. B., and Jha, R., Sensitivity enhancement of surface plasmon resonance sensor using hybrid configuration of 2D materials over bimetallic layer of Cu-Ni, Opt. Commun. 463, 125337 (2020).

165. Mohamed, A., Bedir, Y., Nehal, F. A., and Mahmoud E., Improved the quality factor and sensitivity of a surface plasmon resonance sensor with transition metal dichalcogenide 2D nanomaterials, J. Nanopart. Res. 22, 189 (2020).

166. Liu, N., Shutao, W., Qi, Ch., Bo, P., and Jiangtao Lv., High Sensitivity in Ni-Based SPR Sensor of Blue Phosphorene/Transition Metal Dichalcogenides Hybrid Nanostructure, Plasm.16 (2021).

167. Pal, A., and Jha, A., A Theoretical Analysis on Sensitivity Improvement of an SPR Refractive Index Sensor with Graphene and Barium Titanate Nanosheets, Optik 231, 166378 (2021).

168. Kumar, R., Pal, S., Pal, N., Mishra, V., and Prajapati, Y. K., High-performance bimetallic surface plasmon resonance biochemical sensor using a black phosphorus-MXene hybrid structure, Appl. Phys. A 127, 259 (2021).

169. Dhibi, A., Hakami, J., and Abassi, A., Performance analysis of surface plasmon resonance sensors using bimetallic alloy--bimetallic alloy and perovskite-bimetallic alloy-perovskite nanostructures, Phys. Scr. 96, 065505 (2021).

170. Lin, Z., Jiang, L., Wu, L., Guo, J., Dai, X., Xiang, Y., Fan, D., Tuning and sensitivity enhancement of surface plasmon resonance biosensor with graphene covered Au-MoS2-Au films. IEEE Phot. Jour. 8(6), 1-8 (2016).

171. Jia, Y., Li, Z., Wang, H., Saeed, M., and Cai, H., Sensitivity enhancement of a surface plasmon resonance sensor with platinum diselenide. Sensors 20(1), 131 (2020).

172. Rahman, M. M., Rana, M. M., Rahman, M. S., Anower, M. S., Mollah, M. A., and Paul, A. K., Sensitivity enhancement of SPR biosensors employing heterostructure of PtSe2 and 2D materials. Opt. Mater. 107, 110123 (2020).

173. S. Pal et al., "Sensitivity enhancement of metamaterial based surface plasmon resonance biosensor for near infrared," Int. J. Opt. Appl. vol. 46, no. 1, pp. 131–143, 2016.

174. K. Hitomi et al., "Characterization of thallium bromide crystals for radiation detector applications," J. Cry. Grow. vol. 225, no.2-4, pp-129-133, May 2001.

175. Z. Lin, S. Chen, and C. Lin, "Sensitivity improvement of a surface plasmon resonance sensor based on two-dimensional materials hybrid structure in visible region: a theoretical study," Sensors, vol. 20, no. 9, pp-2445, Jan 2020.

176. I. Pockrand, "Surface plasma oscillations at silver surfaces with thin transparent and absorbing coatings," Surf. Sci. vol. 72, no. 3, pp-577–588, 1978.

177. J. F. Masson, "Surface plasmon resonance clinical biosensors for medical diagnostics, ACS sensors, vol. 2, pp.16-30, Jan 2017.

178. H. Jussila, H. Yang, N. Granqvist, and Z. Sun, "Surface plasmon resonance for characterization of large-area atomic-layer graphene film," Optica, vol. 3, no. 2, pp. 151–158, Feb 2016.

179. C. Sindal, Y. Vasimalla and P. N. Patel, "Performance Analysis of Surface Plasmon Resonance Sensor Having Multi-layer Structures of MoS_2 and Graphene in NIR-region," 2019 3rd International Conference on Electronics, Materials Engineering & Nano-Technology (IEMENTech), 2019, pp. 1-5.

180. M. S. Rahman, M. S. Anower, M. K. Rahman, M. R. Hasan, M. B. Hossain, and M. L. Haque, "Modeling of a highly sensitive MoS2-Graphene hybrid based fiber optic SPR biosensor for sensing DNA hybridization," Optik. 140, 989-97 (2017).

181. B. H. Ong, X. Yuan, S. C. Tjin, J. Zhang, and H. M. Ng, "Optimised film thickness for maximum evanescent field enhancement of a bimetallic film surface plasmon resonance biosensor," Sens. Actuators B Chem., 114, 1028-1034 (2006.)

182. Y. Vasimalla, H. S. Pradhan, and R. J. Pandya, "Sensitivity enhancement of the SPR biosensor for Pseudomonas bacterial detection employing a silicon-barium titanate structure," Appl. Opt. 60(19):5588-5598 (2021).

183. M. S. Rahman, S. S. Noor, M. S. Anower, L. F. Abdulrazak, M. M. Rahman, K. A. Rikta, "Design and numerical analysis of a graphene-coated fiber-optic SPR biosensor using tungsten disulfide," Phot. Nanostruct. Fund. Appl. 33, 29-35 (2019).

184. A. Kumar, A. K. Yadav, A. S. Kushwaha, and S. K. Srivastava, "A comparative study among WS2, MoS2 and graphene based surface plasmon resonance (SPR) sensor," Sens. Actuators Rep. 2(1), 100015 (2020).

185. Y. Xu, L. Wu, and L. K. Ang, "Surface exciton polaritons: A promising mechanism for refractive-index sensing," Phys. Rev. Appl. 12(2), 024029 (2019).

186. B. Hossain, A. Kabir, M. Rahman, S. Roy, L. F. Abdulrazak, S. Hossain, N. Mondol, M. H. Rahman, K. Z. Islam, and M. I. Pathan, "Hybrid structure based high performance SPR sensor: a numerical approach of structure optimization for DNA hybridization," Opt. Quant. Elect. 53(1), 1-9 (2021).

187. P. T. K. Loan, W. Zhang, C. T. Lin, K. H. Wei, L. J. Li, and C. H. Chen, "Graphene/MoS2 heterostructures for ultrasensitive detection of DNA hybridization," Adv. Mater. 26, 4838–4844 (2014).

188. M. B. Hossain, M. A. Kabir, M. S. Hossain, K. Z. Islam, M. S. Hossain, M. I. Pathan, N. Mondol, L. F. Abdulrazak, M. A. Hossain, and M. M. Rana, "Numerical modeling of MoS2–graphene bilayer-based high-performance surface plasmon resonance sensor: structure optimization for DNA hybridization," Opt. Eng. 59(10), 105105 (2020).

189. M. K. Singh, S. Pal, A. Verma, Y. K. Prajapati, and J. P. Saini, "Highly sensitive antimonene-coated black phosphorous-based surface plasmon-resonance biosensor for DNA hybridization: design and numerical analysis," J. Nanophot. 14(4), 046015 (2020).

190. T. Haque, and H. K. Rouf, "DNA hybridization detection using graphene-MoSe2–Ag heterostructure-based surface plasmon resonance biosensor," Appl. Phys. A 127(10), 1-3 (2021).

List of Publications

International Journals

1. Yesudasu V, Himansu Shekhar Pradhan, Pandya RJ., "SPR performance enhancement for DNA hybridization employing black phosphorus, silver, and silicon," Applied Optics, 59(24), 7299-7307 (2020).
2. Yesudasu V, Himansu Shekhar Pradhan, Pandya RJ., "Recent progress in surface plasmon resonance based sensors: A comprehensive review", Heliyon. 7(3), e06321 (2021).
3. Yesudasu V, Himansu Shekhar Pradhan, Pandya RJ., "Sensitivity enhancement of the SPR biosensor for Pseudomonas bacterial detection employing a silicon-barium titanate structure," Applied Optics, 60(19), 5588-5598 (2021).
4. Yesudasu V, Himansu Shekhar Pradhan, "Performance Enhancement of a Novel Surface Plasmon Resonance Biosensor using Thallium Bromide", IEEE Transactions on NanoBioscience, 21(2), 206-215 (2022).
5. Yesudasu V, Himansu Shekhar Pradhan "A highly performed SPR biosensor based on bismuth ferrite-bromide materials-BP/graphene hybrid structure", Optical and Quantum Electronics, 53(12), 1-8 (2021).
6. Yesudasu V, Himansu Shekhar Pradhan, "High Performance Fiber-Optic Based SPR Sensor for DNA Hybridization using Black Phosphorus-Tungsten Disulfide Hybrid Structure," Journal of the Optical Society of America B (JOSA B)", 9, 20-32 (2021).

International Conferences

1. Yesudasu V, Himansu Shekhar Pradhan, "Performance Enhancement of SPR sensor in NIR-Region for urea detection using MoS_2-Dielectric materials-MoS_2 Based Structure", (ASIANCON) IEEE, 1-4 (2021).
2. Yesudasu V, Himansu Shekhar Pradhan, "A Highly Performed SPR sensor for Urea Detection Using Au-BeO-GaP Based structure", In2021 5th Conference on Information and Communication Technology (CICT) IEEE, 1-4 (2021).
3. Yesudasu V, Himansu Shekhar Pradhan, "Performance Enhancement of SPR sensor for Urea Detection Using Au-Dielectric Materials Based structure",- Accepted – IEEE ICAECC- (2022).